Faculdade de Engenharia da Universidade do Porto

Computational Left-Ventricle Reconstruction from MRI Data for Patient-specific Cardiac Simulations

Maria Isabel von Hafe Pérez Ferreira da Silva

Dissertation conducted under the
Integrated Master in Bioengineering - Branch of Biomedical Engineering

Supervisors:

Hans Christian Hege, Director of Research Department "Visualization and Data Analysis" at Zuse Institute Berlin (ZIB)

Aurélio Campilho, Full Professor in the Department of Electrical and Computer Engineering at the Faculty of Engineering of the University of Porto

Hans Lamecker, Senior Researcher at Zuse Institute Berlin (ZIB)

Jorge Novo Buján, Post-doctoral Investigator at the INESC Technology and Science (INESC TEC) in Porto

September, 2014

Abstract

Recent developments and sophistication of medical imaging technologies, such as Magnetic Resonance (MR), Computed Tomography and Ultrasonography, resulted in more accurate and detailed images of the human body, from which a wide range of valuable anatomical and physiological information can be extracted. Cardiac research has increasingly recognized that heart modeling can help interpret and analyze the provided information from imaging technologies. By combining it with prior biophysical information and other clinical data it is possible to obtain a more realistic model, which can be used for medical diagnosis, to predict surgical outcomes and finally to support treatment decisions. The heart is an organ with a complex structure and function, presenting involuntary cyclical movements, which together with the respiratory motion complicates image acquisition and cardiac modeling. Nevertheless, considering the extreme negative impact that cardiovascular diseases have in the society, the interest in cardiac modeling has received increasing attention, especially in the context of patient-specific medical simulations.

The present dissertation establishes a simple methodology to reconstruct the spatio-temporal left ventricle (LV) anatomy from MRI data for personalized cardiac simulations. Considering the main role that the LV plays in the cardiovascular system, the characterization of its anatomy and function is essential in the clinical practice for the diagnosis of pathological situations, such as the aortic valve diseases. Therefore, the development of personalized in-silico models that allow not only the observation of this heart chamber in 3D and its deformation along the cardiac cycle, but also enables the conduction of patient-specific cardiac simulations, can have an enormous impact on the diagnosis and treatment of cardiovascular diseases. The methodology here proposed extracts personalized geometric surfaces that represent accurately the anatomy of the inner LV surface in different phases of the cardiac cycle from MR images. In order to overcome the main challenges inherent to left ventricle modelling, such as the reconstruction of the apical and basal regions and the correction of motion-related artifacts, interactive techniques that combine different types of MR images used in clinical practice were developed. As final result, a set of smooth surfaces with high quality finite element meshes that represent accurately the geometric shape of the LV cavity in different phases of the cardiac cycle were obtained. This set of patient-specific LV surfaces describe the natural motion of a beating heart and encode information about the regions of the surface that deform at most between two instants of the cardiac cycle. The reconstructed shape of the LV with a smooth geometry and isotropic triangular mesh can be combined with other cardiac models to conduct patient-specific cardiac simulations, such as blood-flow simulations in patients with an aortic valve disease.

Concepts regarding the cardiac anatomy, function and modeling that were crucial for the understanding and development of this project will be addressed. This dissertation also presents the state-of-the-art in the field of LV reconstruction for simulations purposes, by introducing and discussing the most important works on this subject, giving special attention to recent projects based on MRI.

Resumo

Actualmente, os níveis de desenvolvimento e sofisticação das tecnologias para imagiologia médica, tais como Ressonância Magnética (RM), Tomografia Computorizada e Ultra-sonografia, permitem a aquisição de imagens do corpo humano com bastante detalhe, a partir das quais é possível extrair uma vasta gama de informação anatómica e fisiológica. No campo da investigação cardiovascular, a importância de modelos cardíacos para apoiar a interpretação e análise da informação proveniente das tecnologias de imagiologia tem sido altamente reconhecida. A combinação deste tipo de modelos com informação biofísica e com outros tipos de dados clínicos permite a construção de um modelo computacional mais próximo da realidade, que pode ser utilizado para diagnóstico médico, previsão de procedimentos cirúrgicos e por último apoiar decisões relativas ao tipo de tratamento a adoptar.

O coração é um órgão com uma estrutura e função complexas, apresentando movimentos cíclicos e involuntários que, em conjunto com os movimentos respiratórios, complicam a aquisição de imagens cardíacas e também o processo de modelação cardíaca. No entanto, devido ao impacto extremamente negativo que as doenças cardiovasculares têm na sociedade moderna, o interesse no desenvolvimento de modelos cardíacos tem vindo a aumentar de forma significativa, particularmente em modelos apropriados para a realização de simulações cardíacas personalizadas.

Esta dissertação estabelece uma metodologia simples para a reconstrução espacial e temporal da anatomia do ventrículo esquerdo a partir de imagens de RM para posteriores simulações cardíacas personalizadas. Tendo em consideração a função fulcral do ventrículo esquerdo no sistema cardiovascular a caracterização da sua anatomia e da sua função é essencial para a detecção e diagnóstico de certas situações patológicas, tais como doenças da válvula aórtica. Neste contexto, a construção de um modelo *in silico* personalizado que permita a observação em 3D da anatomia e da deformação do ventrículo esquerdo ao longo do ciclo cardíaco terá um impacto significativo no diagnóstico e tratamento de doenças cardiovasculares. Na metodologia desenvolvida nesta dissertação, os diferentes tipos de imagens de RM foram combinados através de métodos interactivos de forma a ultrapassar as dificuldades inerentes ao desenvolvimento de modelos cardíacos, tais como a reconstrução das regiões apical e basal e a correcção de artefactos consequentes dos movimentos cardíacos e respiratórios. O resultado final consiste em superfícies geométricas suaves que representam de forma detalhada a anatomia do ventrículo esquerdo ao longo do ciclo cardíaco. Esta sequência de superfícies ventriculares possibilita não só a observação *in silico* do movimento natural do coração durante um batimento cardíaco de um determinado paciente, mas também a identificação das regiões ventriculares que sofrem uma deformação mais intensa entre duas fases do ciclo cardíaco. O resultado da reconstrução espacial e temporal do interior do ventrículo esquerdo na forma de superfícies com uma malha de elementos finitos isotrópica e homogénea pode ser combinado com outro tipo de modelos cardíacos para a realização de simulações cardíacas personalizadas, como por exemplo a simulação do fluxo do sanguíneo em pacientes com uma doença valvular.

Esta dissertação introduz os conceitos relativos à anatomia, função e imagiologia cardíacas que foram e são relevantes para a compreensão do problema em causa e também para o desenvolvimento do projecto. O estado-da-arte relativo à reconstrução do ventrículo esquerdo para a realização de simulações cardíacas também será discutido, dando especial atenção aos trabalhos publicados recentemente e baseados em imagens de RM.

Acknowledgements

First of all, I wish to thank Hans-Christian Hege, head of the Department of Visualization and Data Analysis at the Zuse Institute Berlin (ZIB), for giving me the opportunity to develop this interesting and challenging project at ZIB and for providing me the first contact with the field of Data Visualization and with a work environment outside the university context. Without his constant support this work would not have been possible.

I am sincerely grateful to Prof. Aurélio Campilho, who awakened my great interest in the field of biomedical imaging analysis and processing and who guided me with his knowledge and constructive critics in the development of this dissertation.

I also want to thank Dr. Hans Lamecker and Dr. Jorge Novo Buján for sharing with me their knowledge and experience in this field. Their vision, extensive support and constant availability contributed to very important improvements of this work.

It was a pleasure to work with all the collaborators of the Department of Visualization and Data Analysis at ZIB, who contributed to a friendly and motivating work atmosphere. In this context, I give a special thanks to Olaf Paetsch, Alexander Kuhn, Vincent Dercksen, Ulrike Homberg and Dr. Daniel Baum, who contributed to my quick integration in the institute and were always available to help me overcome technical difficulties and to support me in the use of the software Amira and also in the German language.

I wish to thank the partners from the DHZB for their medical contribution, but especially Dr. Eng Leonid Goubergrits who introduced me to the research field of cardiac biomechanics and contributed to the developed methodology to achieve the aims of this project. I am truly grateful to João Filipe Fernandes, for his patience and constant availability to guide me in the field of cardiovascular image analysis and processing.

To Prof. Artur Cardoso and Prof. Diamantino Freitas, I want to thank their support in my application for an internship at ZIB, which allowed the realization of this project.

I also thank the European ERASMUS Placements Program for the financial support to fulfill an internship abroad.

At last, but not least, I would like to express my deep gratitude to my parents and my brothers and also to my colleagues and friends Maria Eira and Miguel Duarte, for their constant and indispensable support throughout the course of this Integrated Master in Bioengineering.

Contents

List of Acronyms

2CH - 2 Chambers

3CH - 3 Chambers

4CH – 4 Chambers

3D-WH – 3D Whole Heart

AHA - American Heart Association

ASNC - American Society of Nuclear Cardiology

CoA - Aortic Coarctation

AR - Aortic Regurgitation

AS - Aortic Stenosis

AVD - Aortic Valve Diseases

AV - Atrio-Ventricular

bFFE - balanced Fast Field Echo

CRT - Cardiac Resynchronization Therapy

CVD - Cardiovascular Diseases

CMRI - Cardiovascular MRI

CFD - Computational Fluid Dynamics

CT - Computed Tomography

CARDIOPROOF - Proof of Concept of Model-based Cardiovascular Prediction

DHZB – *Deutsches Herzzentrum Berlin*

DICOM -Digital Image and Communication in Medicine

DT - MRI Diffusion Tensor MRI

ECG - Electrocardiograms

EDV - End Diastolic Volume

ED - End of Diastole

ESV - End Systolic Volume

ES - End of Systole

EU - European Union

FE - Finite Elements

GL - Gray Level

IP – Intersection Point

LAX – Horizontal Long Axis

LGE - Late-Gadolinium-Enhancement

LV - Left Ventricle

LVEF - Left Ventricular Ejection Fraction

MRI - Magnetic Resonance Imaging

MDCT - Multi-Detector Computed Tomography,

PC - Phase Contrast

PET - Positron Emission Tomography

RF - Radiofrequency

SAX - Short Axis

SPECT - Single Photon Emission Computed Tomography

SA - Sino-Atrial

SVR - Surgical Ventricular Restoration

VHD - Valvular Heart Disease

TP - Time Point

TRA - Transversal

US - Ultrasonography

USA - United States of America

RVEF – Right Ventricular Ejection Fraction

VS - Voxel Size

WHO - World Health Organization

Chapter 1 - Introduction

1.1 – Problem and Motivation

According to the World Health Organization (WHO) cardiovascular diseases (CVD) are the number one cause of death and there are projections indicating that the situation will remain (World Health Organization, 2014). An estimated 17.3 million people died from CVD in 2008, representing 30% of all global deaths. Of these deaths, 7.2 million were due to heart attacks and 5.7 million were due to stroke. If the current trends continue, by 2030 an estimated 23.6 million people will die from cardiovascular diseases in the world. In Unites States of America (USA), an estimated 80 million adults (more than one in three) have one or more types of cardiovascular diseases, causing an American fatality every 40 seconds (Wang & Amini 2012). Furthermore, the American Heart Association (AHA) foresees that 40.5% of Americans, or roughly 116 million people, will have some form of cardiovascular disease by the year 2030. The annually economic implications associated with cardiovascular diseases exceed 503 billion $ in the USA (Ringenberg et al. 2013) and 169 billion € in the European Union (EU) (Leal et al. 2006).

Due to the social and economic impacts of cardiovascular diseases, their prevention, detection and identification (diagnosis), prediction of evolution, and therapy are important issues for improving treatments and reducing mortality and morbidity. From this context arises a demand for preferably non-invasive, accurate diagnosis procedures. Analysis of the cardiac function using imaging instruments has shown to be effective in diagnosing, reducing the mortality and morbidity of CVD.

Magnetic Resonance Imaging (MRI) is a noninvasive imaging technique with the capability to monitor and assess the progression of CVD so that effective procedures for the care and treatment of patients can be developed by physicians and researchers. However, myocardial images analysis is time consuming and suffers from inter and intra-observer variability. Computerized processing and analysis can help clinicians to visualize and interpret the medical conditions objectively (Tavakoli & Amini 2013). Cardiovascular MRI (CMRI), by acquiring data from contiguous, serial electrocardiogram (ECG) gated images of the thorax (including the cardiac apex to the aortic arch) contains sufficient information to allow computer-aided reconstruction of the heart and great vessels in three or four (including time) dimensions (Laschinger et al. 1988). This spatiotemporal (4D) cardiac imaging and reconstruction provides qualitative and quantitative information about the morphology, kinematic and electric function and tissue properties of the heart and larger vessels, enabling the creation of an anatomically realistic model of the heart with detailed heart structure information. This model is of great value in electromechanical simulation, by simulating in different conditions the main cardiac features, including cardiac rhythms, mechanics, hemodynamics, fluid-structure interaction, energy

metabolism, and neural control (Deng et al. 2012). The developed models can be used for medical teaching, surgery planning and to support the study of the physiological and pathological mechanism of the heart diseases, such as heart failure, valvular pathologies, arrhythmias or ventricular fibrillation, and hence, to help improve their diagnosis and treatment (Deng et al. 2012). Besides, the computational reconstructed heart can be used as a basis to optimize the design of implantable devices, such as artificial cardiac valves, for improved therapy (Sermesant et al. 2008). The integration of clinical data into computational models of the heart, allows the projection of 3D numerical models with patient-specific parameters, which introduces enormous potential for improving personalized diagnosis, treatment planning, and interventions for cardiovascular diseases. Furthermore, these models have the potential for predictive use and may aid in guiding patient management and therapy planning in the future, both clinically and surgically (Ringenberg et al. 2013).

A particular case of cardiac pathologies that would benefit from a patient-specific model for simulation purposes is the valvular heart disease (VHD). Although less common in industrialized countries than coronary artery disease, heart failure, or hypertension, VHD is associated to a dramatic socio-economic impact due to the need for surgical treatment and hospitalization, as well as to possible peri- and post-operative complications (Vahanian et al. 2012). According to the AHA, the prevalence of any type of VHD in the USA population is 2.5%, from which almost 40% are related to aortic valve diseases (AVD), namely aortic stenosis or aortic regurgitation. Currently, only in the EU, more than 50 000 aortic valve replacements are reported per year, each with an associated cost between 10 000 € and 20 000 € (CARDIOPPROOF, 2014). Therefore, modeling methods that improve the understanding of AVD mechanism and allow predicting the evolution of disease or treatment outcomes are highly recommended.

Patient-specific Modeling for CVD

The detailed anatomical reconstruction from a patient's heart using its clinical data from various sources, such as electrocardiograms (ECGs), CT (Computed Tomography) and MRI scans, measurements of blood flow and blood pressure, is essential for patient-specific simulations of cardiac electrophysiology, mechanics and hemodynamics. In other words, using the patient's own medical data, 4D working personalized representation of the heart, in its current state could be created. This could be used to simulate a number of pathologies or the effect of therapeutic actions and to analyze the cardiac function of the considered patient, giving valuable details without the need of invasive procedures (Billet et al. 2004). For instance, observing how a problem such as a hole in the heart deforms with each beat, could help in the identification of the critical junctions to make tightest suture during a surgical intervention. Depending on the desired simulation, these models must represent a variety of anatomical structures and functional information. For example, when simulating the electrophysiology in cardiac

resynchronization therapy (CRT) it is desirable to have a model comprising the anatomy including part of the coronary veins, tissue motion and scar tissue distribution in the left ventricle. Finally, the model should also incorporate clinical knowledge about how cardiovascular disease disturbs the correct functioning of the heart (Weese et al. 2013).

At the level of aortic valve diseases, the increasing sophistication of surgical solutions and the broad range of available heart valve prostheses require the development of quantitative patient-specific computer simulation tools to aid surgical planning through the assessment of pre-operative scenarios and prediction of post-operative and/or post-implantation outcomes (Vota et al. 2014). Such models would contribute to the analysis of the patient's heart reaction in terms of blood-flow and mechanics to the implantation of an artificial cardiac valve.

In this context arises a critical need of integration of state-of-the-art clinical imaging with biomechanical computational approaches and with personalized clinical information, not only to enable a reconstruction and visualization of patient-specific 4D heart models, but also to support simulation-based therapy decisions.

1.2 – Overview

This dissertation was prepared at the Visualization and Data Analysis Department from *Konrad-Zuse-Zentrum für Informationstechnik Berlin*[1] (ZIB), a research institute for applied mathematics and computer science. The project integrates a main European project, led by the *Deutsches Herzzentrum Berlin* (DHZB, German Heart Institute Berlin), that aims to determine the applicability and effectiveness of predictive modeling and simulation tools for cardiology, known as CARDIOPROOF[2] (Proof of Concept of Model-based Cardiovascular Prediction). It focuses on pathologies related to the aorta, namely the AVD and aortic coarctation (CoA), characterized by left ventricle (LV) pressure and/or volume overload and impaired pump function, which if left untreated can lead to irreversible heart failure.

In both AVD and CoA, the timing and type of treatment (surgery, catheter based intervention or medication/follow-up) are crucial to prevent potentially life threatening sequelae (e.g. heart failure) and, on the other hand, to avoid too early procedures, which might in turn increase the risk for re-operation during the life time of a given patient. Tools that can help improve such decision-making would, therefore, have a significant impact on patient management guidelines, as well as on outcomes and on socio-economic costs. CARDIOPROOF will thus try to apply predictive methods concerning the immediate treatment outcome of intervention on cardiac pump and intrinsic myocardial function, enabling physicians to choose best timing and treatment options. Furthermore, by using virtual models of different valve prostheses, CARDIOPROOF will guide decision-making related to different types of valve surgery (aortoplasty,

[1] ZIB, http://www.zib.de/en/home.html

[2] CARDIOPROOF, http://www.cardioproof.eu/

biological/mechanical valve). These problems will be addressed by modelling the response to aortic valve repair both in terms of local haemodynamics and LV load. The response will be modeled for virtual implantation of different mechanical and biological valve substitutes and for virtual valve reconstruction. Among others, it will be important to develop computational fluid dynamics (CFD) models of the aortic valve and the aorta including fluid-structure interaction and a biomechanical-electrophysiological model of the LV.

The scope is to develop, apply and validate modeling methodologies for performing patient-specific in-silico simulations of ventricular electro-mechanics and to provide deformation data which can be used as a boundary condition for fluid flow simulations. The patient-specific mechanical deformation model shall consist of four main components, an anatomical finite element (FE) model, a constitutive model of passive mechanical properties, an active contraction model which drives contraction and relaxation and a haemodynamical model to serve as a pressure-volume boundary condition, which requires patient-specific parameterization. These models should be physiologically sufficiently detailed to facilitate a direct clinical interpretation of results and should also ensure that simulations can be executed with inexpensive hardware within time frames which are compatible with a clinical framework.

In order to develop the anatomical FE model, a processing pipeline for translating clinical image data on 4D cardiac anatomy into finite element meshes of the ventricles and the attached vessel must be set up. Taking into account that the LV plays the major role in the cardiac pump function (particularly in the AVD cases), the goal of the sub-project presented in this document was to establish a framework to extract a geometric and anatomically accurate surface of the LV cavity, in the different phases of the cardiac cycle. In order to represent the cardiac anatomy in a diastolic configuration, different types of 2D and 3D ECG-gated cardiovascular MR image stacks corresponding to the instant of end diastole were processed, merged and tessellated into a static triangular finite element mesh. The reconstruction strategy was then propagated to the remaining phases of the cardiac cycle. For this end, the biomedical data were processed with Amira®, a software for 3D data visualization, analysis, modeling and visualization. The final results consist on eleven personalized, geometric and smooth surfaces with high quality meshes, representing the LV cavity in different states of the cardiac cycle. Those will serve as one of the input parameters for the biomechanical model, designed to obtain the strain and stress distribution throughout the ventricles, ventricular displacement fields (in particular, the displacement of endocardial surfaces), and pressure-volume loops, i.e cavitary volume and pressure changes over a heart cycle.

Figure 1.1 depicts a flowchart that summarizes the concept of the developed project and its integration in the CARDIOPROOF project.

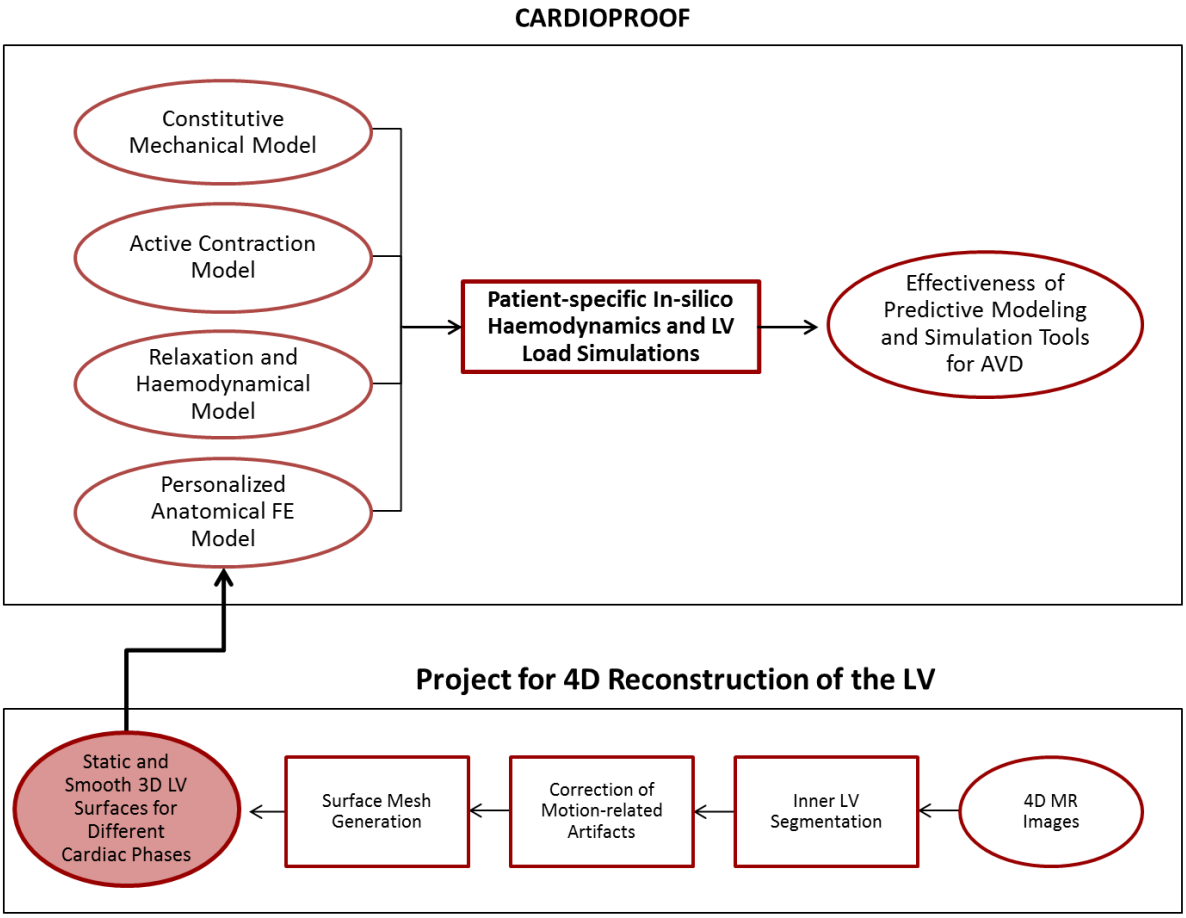

Figure 1.1 - Flowchart resuming the developed work in this project for the 4D reconstruction of the LV cavity and its integration in the European project CARDIOPROOF.

The developed framework consists on the following main phases:

1. Identification of the physiological state that best represents the anatomical structure of the heart in the images, which usually is the end-diastolic phase of the cardiac cycle.
2. Registration from MR images with different orientation
3. Extraction of the global structure of inner LV (endocardium) for the selected functional stage by image segmentation of the MRI data.
4. Slices' alignment to correct motion-related artifacts during image acquisition.
5. Extraction of a smooth and accurate surface mesh from the labeled fields, suitable for finite element analysis.
6. Creation of further static models within the cardiac cycle, by adaption of the aforementioned methods to the MR images of the remaining cardiac phases.

The main contribution of this work is the establishment of a simple and interactive method to solve the complex problem of personalized spatio-temporal LV surface reconstruction, which was

performed under the supervision of experts in the cardiology area. This 4D reconstruction of the LV allows a primary evaluation of a patient's cardiac anatomy and function. Besides it will serve as one of the inputs to construct the patient-specific mechanical deformation model that will be used for in-silico simulations regarding the aortic valve disease.

The remainder of this document is organized as follows: Chapter 2 describes the relevant anatomical and physiological aspects of the heart for this project and also the main cardiac image acquisition modalities namely, Ultrasonography (US), Nuclear Imaging (PET and SPECT), Computed Tomography (CT) and, with more detail, Magnetic Resonance Imaging (MRI). Chapter 3 introduces the concept of heart modeling, its applications and respective challenges and limitations. Chapter 4 reviews recent activities on the reconstruction of the LV surface, taking into account simulation purposes. Subsequently, Chapter 5 presents the developed framework and respective methods and materials that were used to create the inner LV model in eleven phases of the cardiac cycle, whereas the results are presented in Chapter 6, followed by a discussion and evaluation in Chapter 7. At last, the main conclusions that can be deduced from the developed work are exposed in Chapter 8.

Chapter 2 - Cardiac Anatomy, Physiology and Imaging

The cardiovascular system is composed of the heart, blood and the blood vessels (divided into veins that carry blood to the heart at low pressure and arteries that carry away blood from the heart at high pressure). This system ensures the circulation of blood throughout the body to maintain homeostasis delivering oxygen and nutrients to the cells and removing wastes. The heart is a contractile muscular organ (myocardium) acting as a mechanical blood pump. Cardiac mechanics is achieved by the contraction of cardiac muscle fibers and is maintained by a circulatory system of coronary arteries that supplies the muscle with oxygenized hemoglobin and nutrients. Coronary arteries (right and left) are two branches of the aorta and supply the myocardium through smaller branches such as left anterior descending and left circumflex diagonal arteries. This contraction is involuntary activated by an electrical impulse triggered by cells of the cardiac conduction system. The rate of triggering is regulated by the autonomous nervous system. This electrical impulse propagates in the heart through the conduction system and then through the rest of the cardiac muscles. The electrical impulse and the mechanical contraction are mainly propagated along the cardiac muscle fibers. Consequently their spatial organization and orientation have an impact on the cardiac function (Peyrat 2009).

This chapter first gives a brief overlook of the cardiac anatomy and physiology, taking into account the main aspects for cardiac modeling. Afterwards, the most common imaging techniques that allow observing the cardiac structure, anatomy, and function based on different physical principles are presented.

2.1 – Cardiac Anatomy

The heart is a muscular cone-shaped organ about the size of a clenched fist of the same person, surrounded by two layers of connective tissue inside and outside, called endocardium and epicardium, respectively, and located in the upper body (chest area) between the lungs. The heart anatomy is illustrated in Figure 2.1. This organ is divided into right and left sections separated by the interventricular septum. Each of these right and left sections is divided into upper and lower chambers known as atria (one is called an atrium) and ventricles, respectively.

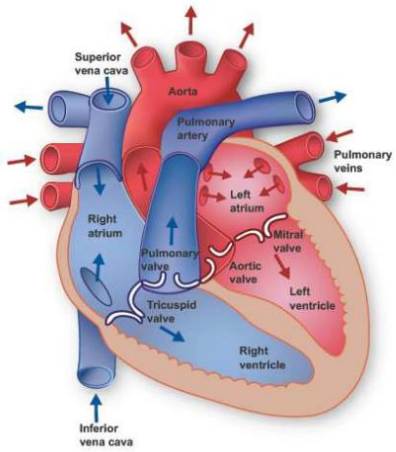

Figure 2.1 - Anatomy of the heart and blood flow that can be followed by the arrows on the diagram, oxygenated blood in red and deoxygenated in blue (from http://www.texasheart.org).

The four main chambers of the heart are therefore:

- the right atrium (RA), pumps blood into the right ventricle;
- the right ventricle (RV), pumps blood into the pulmonary artery;
- the left atrium (LA), pumps blood into the left ventricle;
- the left ventricle (LV), pumps blood into the aorta and is the major contractile chamber maintaining the systemic circulation and having a thicker wall than the RV.

To ensure the blood circulation always in the same direction, the heart includes a series of valves:

- the tricuspid valve, separates the right atrium from the right ventricle;
- the pulmonary valve separates the right ventricle from the pulmonary artery;
- the mitral valve (or bicuspid valve), separates the left atrium from the left ventricle;
- the aortic valve separates the right ventricle from the aorta.

The pulmonary and aortic valves passively open and close with pressure difference between the ventricles and the arteries. The tricuspid and mitral valves are actively controlled by papillary muscles to avoid backflow of blood in atria when blood pressure increases in the contracting ventricles.

Electrical impulses in the heart are originated in specialized cardiac muscle cells, known as self-excitable cells. This type of cells are able to generate an action potential without external stimulation by nerve cells. Only the rate of self-excitability is regulated by the autonomous nervous system depending on needs of the body. The self-excitable cells induce an electrical

stimulus to initiate the cardiac cycle and provide a conduction system to coordinate the contraction of muscle cells throughout the heart. The cardiac conduction system can be divided into five parts enumerated in the direction of propagation of the electrical impulse (Figure 2.2):

1. the sino-atrial (SA) node, located in the upper wall of the right atrium, initiates the cardiac cycle by generating an electrical impulse that spreads through both atria;
2. the atrio-ventricular (AV) node, located near the lower region of the interatrial septum, receives the electrical impulse generated by the SA node. A slight delay of the electrical transmission occurs here, allowing the atria to fully contract before the electrical impulse propagates into the ventricles;
3. the bundle of His (or atrioventricular bundle), a collection of heart muscle cells specialized for electrical conduction, receives the action potential from the AV node and transmits the electrical impulse to the ventricles through the right and left bundle branches;
4. the left and right bundle branches, propagates the electrical impulse in two different parts of the heart, the left and right ventricles;
5. the Purkinje fibers, conduct the action potential from the interventricular septum, down to the apex, and then upward through the ventricles.

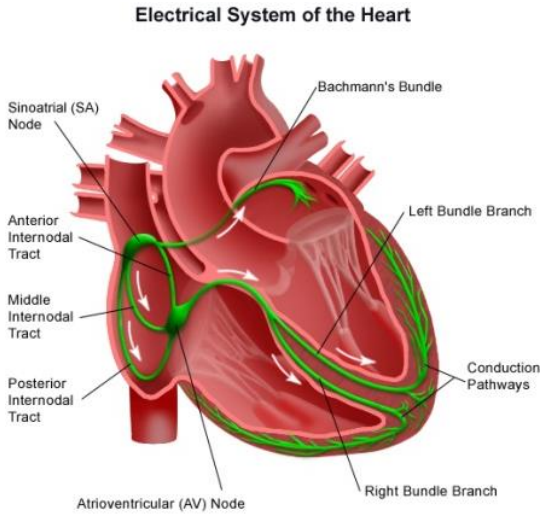

Figure 2.2 – Electrical system of the heart (from http://www.hopkinsmedicine.org/healthlibrary).

2.2 - Cardiac Function

Since the heart has a periodic motion, the description of the cardiac function can be limited to one cardiac cycle. The cardiac cycle is divided into two general phases: systole and diastole. The systole includes events associated with ventricular contraction and ejection, and the diastole includes the ventricular relaxation and filling.

The electrical function of the heart can be observed with the ECG, which gives a global electrical state of the heart (Figure 2.3). The three main features of the ECG are the following:

1. P wave, indicating that the atria are electrically stimulated to pump blood into the ventricles.
2. QRS complex, indicating that the ventricles are electrically stimulated to pump blood.
3. T wave, indicating the recovery period of the ventricles (Peyrat 2009).

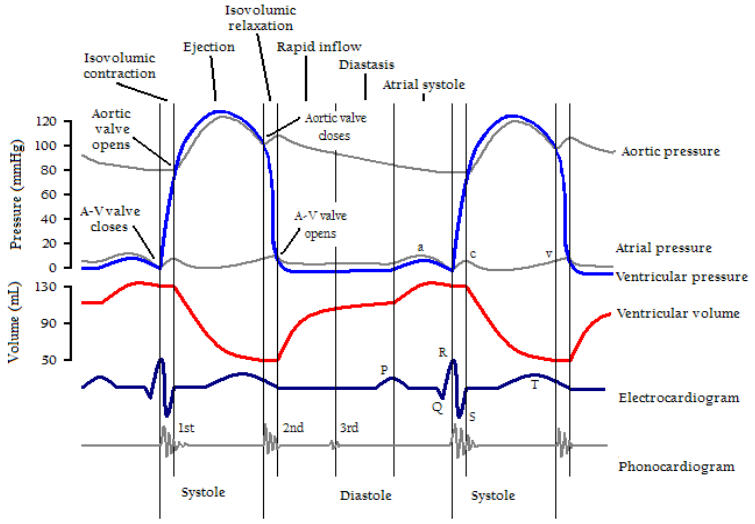

Figure 2.3 - Wiggers Diagram [Richardson 1998] : It shows different parameters of the cardiac function during a cardiac cycle (from http://en.wikipedia.org/wiki/Cardiac_cycle).

Usually, the cardiac cycle is described between the end of diastole (ED) of two consecutives cardiac cycles. The cardiac cycle is further divided into seven phases:

1. The atrial systole: it refers to the contraction of the atrial muscle and it starts when the P wave occurs on the ECG.
2. The isovolumetric contraction: this phase includes the contraction of the ventricle with all valves closed, starting when the R wave occurs in the ECG.
3. The rapid ejection: when the intraventricular pressures exceed the pressures within the aorta and pulmonary artery, the aortic and pulmonary valves open and blood is ejected out of the ventricles.

4. The reduced ejection: during this phase ventricular pressure falls slightly below outflow tract pressure. Atrial pressures gradually rise during this phase owing to continued venous return into the atrial chamber. This phase is characterized by the end of the T wave on the ECG.
5. The isovolumetric relaxation: in this phase the ventricles relax and the intraventricular pressure decreases. When this occurs, a pressure gradient reversal causes the aortic and pulmonary valves to abruptly close.
6. The rapid inflow: when the ventricular pressures fall below atrial pressures, the atrio-ventricular valves open and ventricular filling begins.
7. The diastole: in this period the ventricles are passively filling with blood.

Figure 2.3 summarizes the evolution of some parameters over a cardiac cycle, such as the ECG, sound of the heartbeat, volume curves, and pressure curves. The most common and simple parameters used to assess the cardiac function are the left ventricular (LVEF) and right ventricular (RVEF) ejection fractions. They represent the fraction of blood pumped out of a ventricle with each heart beat (Peyrat 2009). Normally, 70% of the whole LV blood in end diastole is ejected out during systole. The ejection fraction (EF) ratio is an index of global LV function, which is calculated as (EDV–ESV)/EDV, where EDV is the volume of the LV at end-diastole and ESV is the volume of the LV during end-systole. Ventricular walls thicken during systole – this is typically referred as wall thickening and has been proven to be a very reliable index of regional myocardial function. Heart failure is characterized by a significant decrease in the EF. An additional index of cardiac performance is myocardial mass, which can be determined from myocardial volume, assuming the myocardium to have uniform density (Tavakoli & Amini 2013).

Due to atherosclerosis, the coronary arteries may gradually become occluded and end in coronary artery disease. Coronary occlusion leads to disturbance in the cardiac contractility and causes global or regional dysfunction in the heart which may be diagnosed using state-of-the-art medical imaging techniques such as US, MRI, CT, and nuclear medicine.

Aortic valve disease can be caused by aortic stenosis (AS), leading to an obstruction to flow, or by aortic regurgitation (AR), resulting in a leakage backward, or by a combination of both. AS refers to a narrowing of the aortic valve opening during systole and consequently the LV muscles thicken (LV hypertrophy) in order to try to overcome the stress of obstruction. The pressure in the LV when it fills with blood increases and is transmitted to the lungs. AR occurs when the aortic valve does not close properly due to a leakage of the valve backward into the LV after systole. In order to compensate for the large volume of blood that flows backward, the LV cavity enlarges and the wall muscle thickens. Thus, the heart is capable of pumping out both the amount of blood required by the body and the blood that has gone backward into the LV. Long-

standing aortic regurgitation may result in irreversible damage to the muscle of the left ventricle, even in the absence of symptoms. Consequently, appropriate, timely treatment with open-heart surgery may be lifesaving in the case of AVD (Nishimura 2002).

When studying ventricular motion, physicians typically assign a subjective segmental function score to different segments of the ventricles:

- Normokinesia: The myocardial motion and thickening is normal.
- Hypokinesia: The affected segment moves slower and thickens less than normal.
- Akinesia: The infarcted region has totally lost its ability to contract in the systolic phase and moves passively along with its surrounding myocardial tissue.
- Dyskinesisa: The infarcted region moves paradoxically and bulges out during systole due to the ventricular blood pressure.
- Aneurysm: The infarcted region undergoes remodeling, becomes thin, bulging outwards during the systolic phase like a balloon, leading to rupture and death (Tavakoli & Amini 2013).

2.3 - Cardiac Imaging

Cardiac imaging is an integral part of the evaluation of patients with all forms of heart disease. Imaging techniques make it possible to visualize anatomical structures and morphological or functional anomalies of the heart. Due to the inherent nature of cardiac function, the temporal visualization of cardiac anatomy allows a better assessment of cardiac motion and mechanical function. Beyond cardiac anatomy and motion, metabolic function of the heart can also be observed with molecular imaging techniques. There are several cardiac imaging modalities that are in widespread use. These include nuclear imaging (PET and SPECT), US (or echocardiography), cardiac CT, cardiovascular MRI and coronary angiography, which can be used to measure myocardial perfusion, left ventricular function, and coronary anatomy for clinical management and research. The orientation of the heart, angle selection for cardiac planes, number of segments, slice display and thickness, nomenclature for segments, and assignment of segments to coronary arterial territories are important parameters for imaging myocardial perfusion and wall motion that vary between each modality. The definition of these parameters in image acquisition should be based on the following criteria (Cerqueira 2002):

1. Maintain consistency with accepted anatomic and autopsy data.
2. Utilize as much as possible existing and accepted approaches to myocardial segmentation and nomenclature.
3. Allow precise localization by using anatomic landmarks whenever possible.
4. Provide adequate sampling of the left ventricle and coronary distribution without exceeding the resolution limits of the imaging modalities or relevance for clinical and research applications.
5. Allow linkage of the segments to known coronary arterial topography as defined by coronary angiography.

A standardization of these parameters for all modalities would enable accurate intra- and cross-modality comparisons for clinical patient management and research.

The American Society of Nuclear Cardiology (ASNC) has proposed three main cardiac view planes and a myocardial segmentation and nomenclature to be used for all cardiac imaging modalities, which can be observed in Figure 2.4. A view plane through:

- the short axis (SAX), shows both ventricles (Figure 2.4 a)),
- the horizontal long axis (LAX) or the 4-chambers view (4CH) shows the two ventricles and both atria (Figure 2.4 b)),
- the vertical long axis, or the 3-chambers view (3CH) shows the left ventricle, the two atria and the LV outflow tract (LVOT), through the aorta (Figure 2.4 c)).

In the context of LV reconstruction, the 2-chambers (2CH) view plane, where it is possible to observe the left atrium and ventricle and the mitral valve, is also important.

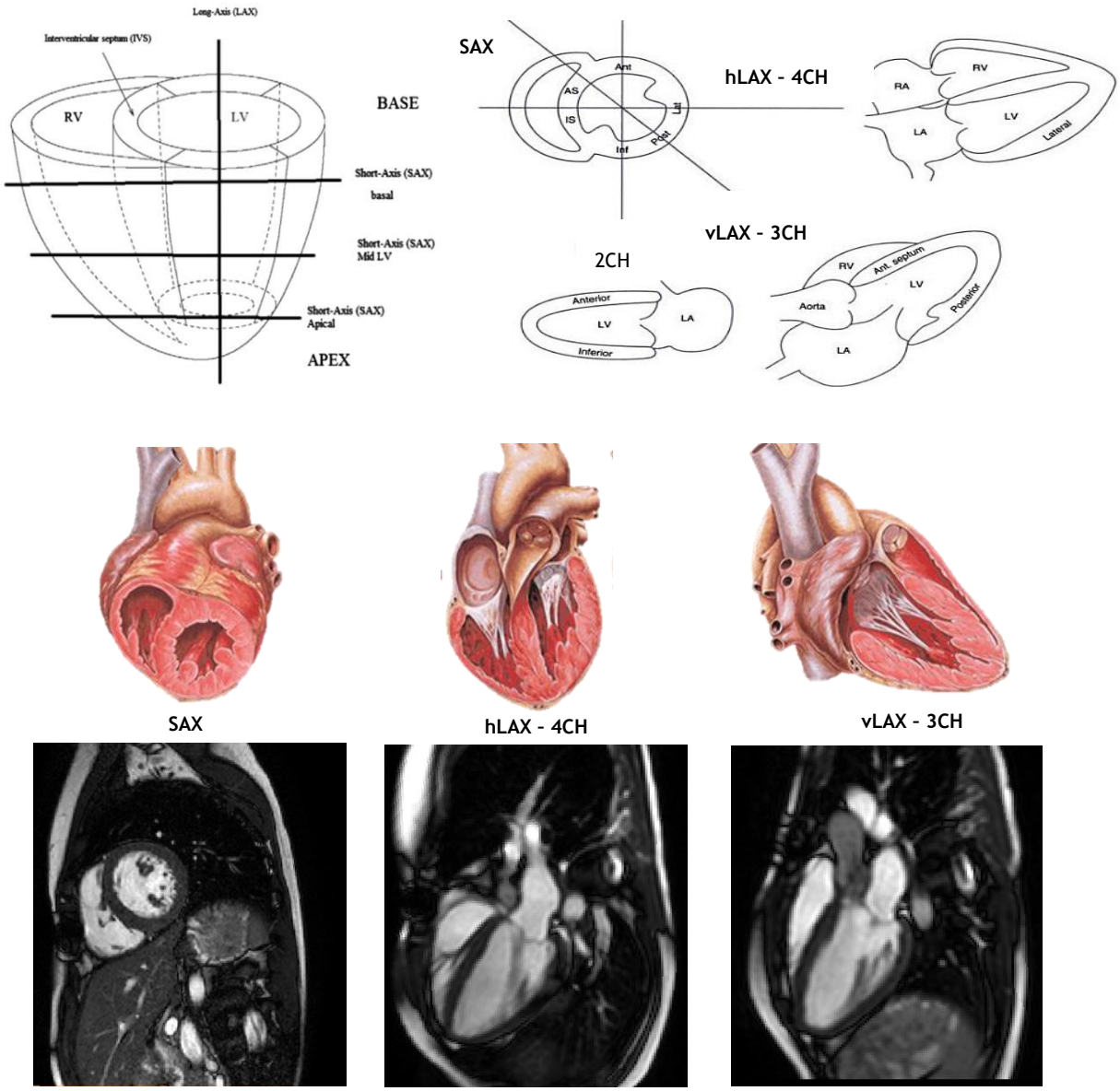

Figure 2.4 – Standard Cardiac Imaging View Planes. On the top-left, an illustration of short axis (SAX) and Long-Axis (LAX) cardiac sections in a normal subject (Tavakoli & Amini 2013). On the top right, simplified representation of the cardiac anatomy represented in the different standard views (from (Lee 2006)). In the middle row representation of the standard cardiac planes as proposed by the ASNC (adapted from yale.edu), short axis, horizontal long axis and vertical long axis, and respective examples of MR images on the bottom (short-axis (SAX), long-axis (LAX), 2 chambers (2CH), 3 chambers (3CH), 4 chambers (4CH)).

The division of the heart in three annular regions along its long axis, results in a basal, mid-cavity and apical regions, that are divided in six, six and four angular segments, respectively. Another segment is included for the apical cap. The attachment of the right ventricular wall to the left ventricle is used to identify and separate the septum from the left ventricular anterior

and inferior free walls. Figure 2.5 shows the location and the recommended names for the 17 myocardial segments prescribed by the American Heart Association (AHA).

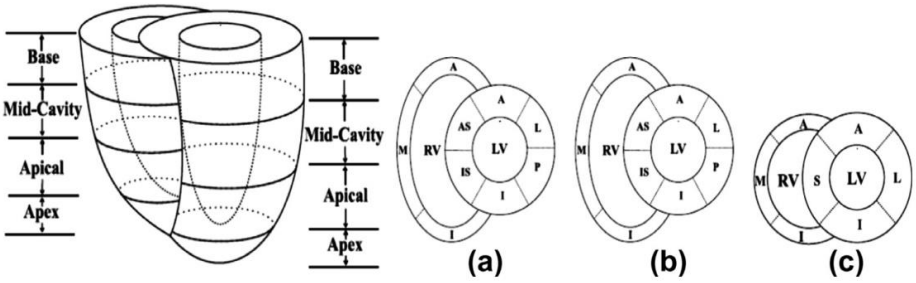

Figure 2.5 - Seventeen AHA prescribed segments for the heart (a) basal SAX view, (b) mid-LV SAX view and (c) apical SAX view. (antero-septal (AS), anterior (A), lateral (L), posterior (P), inferior (I), and infero-septal (IS)), from (Tavakoli & Amini 2013).

Since each method of cardiac imaging has advantages and drawbacks, a brief overview from the non-invasive imaging modalities is presented next. MRI will be characterized with more detail, since this project focuses on the LV reconstruction from MRI data.

2.3.1 – Ultrasonography (US)

Ultrasonographic imaging is based on the partial reflection of acoustic waves at tissue boundaries. An array of piezoelectric crystals generates the backscattered ultrasound wave and the US image contrast is governed by the difference in acoustic properties between adjacent tissues. It is used for assessment of shape, thickness and motion of the cardiac walls and of the heart valves. The US image quality is limited by relatively low contrast between myocardial and adjacent tissues, fading of the endocardial boundaries and image noise (Dell & Mcculloch 2002). Additionally, it suffers from sub-optimal visualization of the cardiac segments, operator dependence issues and air/bone interaction problems causing reverberation artifacts. Besides, in the overweight patients it is very hard to reach the heart, making it impossible to obtain an acoustic window. By measuring frequency shifts between emitted and reflected acoustic signal, Echo-Doppler Imaging can be used to compute the velocity of moving particles, providing an additional motion information displayed as a color overlay on the standard echography sequences. Typically, positive Doppler shift signals, corresponding to flow towards the transducer, are displayed at the red end of the spectrum and flow away from the transducer at the blue end. It is mostly used to study blood flow, characterized by high velocities with low

amplitude, and to measure myocardial wall motion, characterized by low velocities with high amplitude. It can also be used as molecular imaging method by targeting specific molecules with labeled microbubbles with different acoustic properties from that of the tissue (Peyrat 2009). By using recent sophisticated 3D ultrasound transducers consisting on a miniaturized array of piezoelectric crystals, it is possible to obtain 3D US images. Real time 3D scanners were introduced in the early 1990s, but in comparison to 2D echocardiography, initial images suffered from low spatial resolution. New high-tech transducer arrays have significantly improved spatial resolution and image quality – as a result, 3D imaging is enjoying more wide-spread use (Tavakoli & Amini 2013). 3D US has received substantial attention in cardiac valve diseases, which require the imaging of valvular dynamics in three dimensions (Young & Frangi 2009).

Among the current cardiac imaging modalities, US is perhaps the most prevalent because it is non-invasive, cost effective, ease to use, gives real-time feedback, it is portable, with applications at the bedside and during interventions and it is widespread available (Dell & Mcculloch 2002), (Young & Frangi 2009).

2.3.2 – Nuclear Imaging (PET and SPECT)

Injected radioisotopes (the marker) linked to compounds (the tracer) usually involved in a metabolic process are used to produce the image's signal. Positron emission tomography (PET) uses radioactive tracers labeled with radioisotopes, emitting positrons during their radioactive decay. After coming to rest, the positrons annihilate into two nearly back-to-back gamma rays of 511 keV gamma rays, which are detected with a positron camera surrounding the patient. PET can be used to measure myocardial perfusion or to identify areas of normal and reduced metabolism in order to separate viable and necrotic myocardium, for instance after a heart attack (Tavakoli & Amini 2013).

Single photon emission computed tomography (SPECT) uses tracers that emit gamma rays with energy between 50 and 500 keV. Individual photons are detected using either a rotating gamma camera or special purpose multi-detector devices. All detectors used for single photon imaging require some form of gamma ray collimation and, hence, suffer basic limitations to spatial resolution and, more particularly, sensitivity. SPECT is used to detect areas of normal and reduced perfusion in the myocardium (Peyrat 2009). Nuclear imaging is restricted to functional and perfusion information, but it is easy to use, measures relative volumes without the need for geometric assumptions, such as ejection fraction, peak filling/ejection rates, time to peak filling/ejection rates, and other related indices. It is the only modality which can conclusively determine myocardial viability and is typically used as ground-truth in multimodality studies (Tavakoli & Amini 2013). On the other hand, it has relatively low spatial resolution, it is

susceptible to background signal sources, and to variable attenuation during respiration and requires long acquisition times. It cannot be used for assessment of cardiac and coronary artery morphology.

2.3.3 – Computed Tomography (CT)

The latest advances in CT technology enabled the acquisition of time-series of 3D volumes (dynamic 4D CT). Computed Tomography measures the density of tissues with the intensity attenuation of X-Rays passing through the patient. The conventional CT scanner consists of an array of detectors and a single X-ray source (multi-detector computed tomography, MDCT), which is rotated around the sample. The transmitted fan-shaped X-ray beam is recorded at several angles, and a 2D image is reconstructed by using a back- projection algorithm (Dell & Mcculloch 2002). It results in detailed anatomical images of the moving heart with high contrast and exquisite special resolution. A high temporal resolution from MDCT scanners such as 64 (128, 256, or 320) detector-row CT scanners and dual source CT scanner are available with multiple gantry rotations in one second, acquiring several CT slices (64 slice for a 64 row CT scanner). A contrast agent can be injected to enhance the contrast between blood and cardiac tissues (late enhancement CT), enabling the visualization of scarred myocardium. The spectral CT uses a range of X-ray energies to perform tissue characterization. CT angiography is very sensitive for diagnosis of coronary artery, by-pass graft, and stent abnormalities. It is able to acquire unique visualization of the coronary arteries including narrowing, type and degree of atherosclerosis plaque. Additionally, it can also be used to simultaneously visualize the pulmonary and systemic arteries as well as the thrombosis. Cardiac CT is especially useful in evaluating the myocardium, coronary arteries, pulmonary veins, thoracic aorta, pericardium, and cardiac masses, such as thrombus of the left atrial appendage. CT scanners, however, use ionizing radiation, are more expensive and less available than US imagers (Tavakoli & Amini 2013).

2.3.4 - Magnetic Resonance Imaging (MRI)

The world's first magnetic resonance imaging machine was created by Damadian in 1972. MRI uses a pulsed radiofrequency wave in the presence of a high magnetic field to produce high quality images of the body in any plane. It has been recognized as a powerful tool for cardiovascular imaging because of its unique potential to measure blood flow, cardiac wall motion and tissue properties jointly, allowing the evaluation of ventricular volume and function, myocardial viability and vascular anatomy (Christodoulou et al. 2011), (Markl et al. 2012).

Nevertheless, this non-ionizing technology is not portable, it has to be used in a controlled room and its associated cost is very high. Contraindications to the use of MRI include pacemakers and metal implants, since they react to the strong magnetic field.

Physical Principles

Basically, for image acquisition, the patient is placed inside a very strong, stable magnetic field (between 0.2T - 7T, which is 10 000 - 30 000 times stronger than the earth's magnetic field), (Mulkern & Chung 2000). The nuclear magnetization of the hydrogen atoms within the patient's body aligns with the magnetic field. Then, different magnetic gradient fields are applied along the body, in order to obtain a gradient of Larmor precession frequency, which is proportional to the strength of the field. The body area being examined is exposed to pulses of radio waves. When the frequency of transmitted radio wave signal equals the Larmor precession frequency of the aligned protons in a certain region of the exposed body area, resonance occurs and the excited hydrogen atoms emit radiofrequency (RF) echosignals (by relaxation), detectable by an external RF coil in MRI scanners. When a RF pulse is applied at the resonance frequency of a given slice, only the protons in this slice are excited. The signal is analyzed by computer and processed into slice images of the body, which can be taken in any plane. The MR signal is a mix of signals with all the emitted radiofrequencies (encoding in the frequency-encoding direction) and phase shifts (encoding in the phase-encoding direction) that give access to the image slice in the frequency domain. The image slice is reconstructed in the spatial domain using a 2D inverse Fourier Transform (Mulkern & Chung 2000). The emitted signal depends on the proton density and the relaxation times. Magnetic resonance imaging also has the ability to acquire 3- or 4-dimensional data.

Typical cardiac MR (CMR) Images

A challenge of CMR imaging arises from the movement of the heart throughout the cardiac cycle and the movement of the lungs during the respiratory cycle, which produce motion artifacts in the image. Respiratory motion can be alleviated with breath holding during imaging. The problem of heart motion can be solved by prospective scanning with the synchronization of ECG-gated imaging, where phase encodes can then be identified and clustered around a particular time in the cardiac cycle, allowing for the generation of many images at different points in the cycle, albeit shared from different heartbeats (Mulkern & Chung 2000). About thirty phases (or images) can be obtained during one cardiac cycle with the currently available equipment, yielding a temporal resolution of about 30 ms. The number of phases decreases proportionally to the heart rate. Imaging of the heart in cine MRI covers about 10–15 slices and 15–30 frames, depending on the size of the heart, prescribed slice thickness, the heart rate, and specific

approach to image acquisition. A single examination can thus be made up of 250 images. The standard imaging plane is perpendicular to the long (apex-base) axis and called short axis (SAX) plane (Figure 2.6 b) and c)). Images acquired parallel to the long-axis are called Long Axis (LAX) images (Figure 2.6 a)), which can be scanned from different planes, originating 2-, 3-, or 4- heart chambers views (2CH, 3CH, 4CH, see page 22). Those are sometimes combined with SAX images for better visualization of the anatomy as well as for computing true 3D motion (including the through-plane motion) (Tavakoli & Amini 2013). In full-size CMR images, the heart represents a relative small surface and, to decrease the computational time, processing is usually restricted to a smaller computed region of interest (ROI), including only the heart tissue.

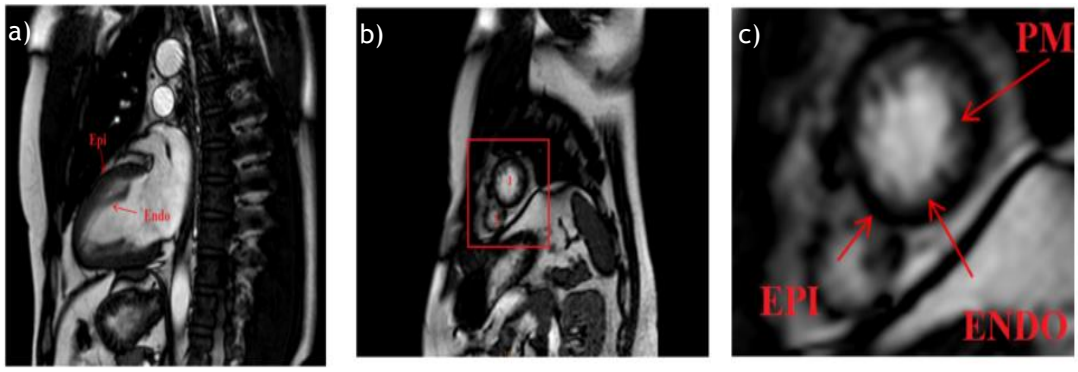

Figure 2.6 – a) Cardiac cine MRI LAX or 2CH view plane; b) Cardiac cine MRI SAX view plane (1:LV, 2:RV); c) a close- up of the SAX image showing the epicardium and endocardium and papillary muscles (PM) shape variability, (from (Tavakoli & Amini 2013).

In Figure 2.7, that represents a typical CMR image, it is possible to observe that blood pools appear bright and myocardium and surrounding structures appear dark, with a spatial resolution of around 1.5 mm per pixel. This aspect is due to the use of balanced Fast Field Echo (bFFE) MRI sequences, which have been replacing standard gradient echo for the last 5 years and considerably improving image quality (Petitjean & Dacher 2011).

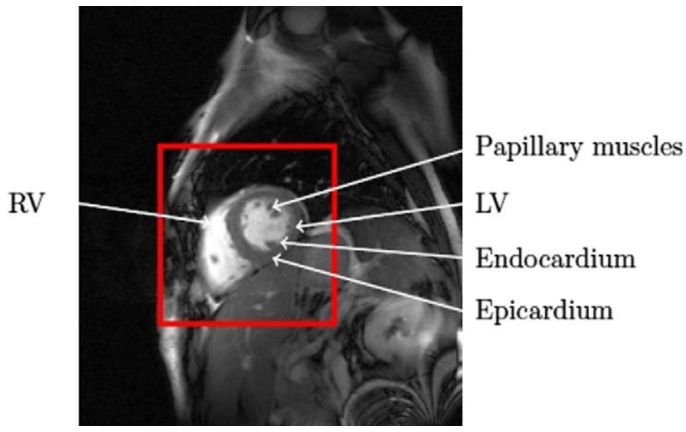

Figure 2.7 - A full size SAX CMR image and a ROI identifying the heart (from (Petitjean & Dacher 2011)).

In Figure 2.8 it is possible to observe the variability, regarding gray levels or structure shapes, present in CMR images. Gray level intensities can also differ due to the use of different MRI scans or different bFFE sequences. Some parts of the images exhibit fuzziness mostly due to the respiration motion artifacts, but also due to blood flow and partial volume effects. This former effect is a consequence of non-zero thickness of MRI slices and consequently, in some areas, a voxel can be a mixture of several tissue types. Figure 2.9, highlights the blood flow effect, showing that the boundaries between the left atrium, right atrium, and the aorta are unclear. In terms of shape, the ventricle varies over patients, over time and over the long axis. The motion-related artifacts, partial volume effect and variability inherent to CMR must be accounted in anatomy's reconstruction algorithms (Petitjean & Dacher 2011).

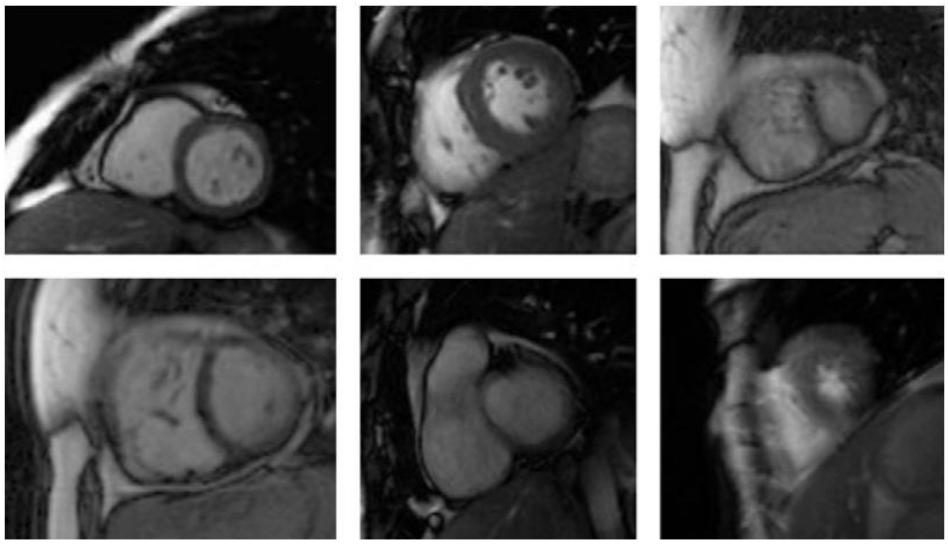

Figure 2.8 - Variability among cardiac images (from (Petitjean & Dacher 2011)).

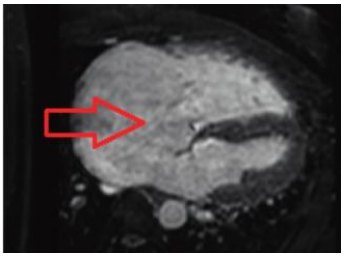

Figure 2.9 - Cardiac MRI image showing that the boundaries between the left atrium, right atrium and the aorta are unclear, as indicated by the arrow, due to the thin walls and partial volume effects (from (Zhuang 2013)).

Main CMRI Modalities

Over the last decades MRI has undergone many substantial developments, where the applicability depends on the cardiac characteristic to be evaluated.

Cardiac cine-MRI is considered the standard MR technique mainly used for global function measurements. Cine sequences MRI are collection of images (usually at the same spatial location) covering of one full period of cardiac cycle or over several periods, in order to obtain complete coverage. This time-resolved technique is able to achieve high resolution images with respect to the cardiac border but the contrast is not very intense inside the cardiac wall. The rapid acquisition time is achieved in cost of a significant slice thickness, resulting in a poor out-of-plane resolution (about 7mm). This method shows dynamic processes, such as the ejection of blood out of the heart into the aorta. By means of fast imaging and displaying the resulting images in a sequential-loop, the impression of a real-time movie is generated. Ejection fractions and stroke volumes calculated from these cine MRI images in different cardiac axes have been shown to be more accurate than any other imaging modality (Magnetic Resonance - Technology Information Portal 2014).

3D whole heart (3D-WH) MR sequence is a free-breathing, isotropic, 3D data acquisition method that scans an entire desirable volumetric slab. Thin slices can be reconstructed from the raw data in any plane without problems of “cross-talk” and without need for interslice gaps (Lee 2006). A respiratory navigator tracks diaphragmatic movement, which eliminates the need for breath-holding. Data are usually acquired during periods when cardiac motion and flow are at minimal levels (usually during mid to late diastole). The disadvantage of this method is the longer acquisition time and a lower in-plane resolution when compared with other CMRI methods, such as the cine-sequences (Bogaert et al. 2012).

A **tagged MRI** uses a special spin tagging pre pulses sequence to create temporary features – tags, producing markers inside the myocardium over time. These tags can be tracked, since they deform together with the myocardium as the heart beats. This deformation is captured by MR imaging, permitting to compute dense myocardial motions and strain. Besides better time resolution, tagged MRI can show not only the surface deformation, but also the in-wall myocardium motion, such as the twisting in the short axis circumferential direction. Tagged MR techniques are used for regional analysis and temporal registration (Tavakoli & Amini 2013).

Phase contrast (PC) sequences utilize the change in the phase shifts of the flowing protons in the region of interest to create an image. Spins that are moving along the direction of a magnetic field gradient receive a phase shift proportional to their velocity. Regions that are stationary remain black, while moving regions are represented as grey to white. PC-MRI can be used for flow imaging, to measure and quantify pulsatile blood flow and cardiac and valve function in the heart and large vessels. Recent developments allow the comprehensive acquisition and analysis of blood flow dynamics with full volumetric coverage of the vascular region of interest. 3D visualization can be performed in order to depict the configuration and changes of blood flow patterns based on the acquired velocity vectors in all three spatial dimensions. In addition to the measurements of basic flow volumes and velocities, the estimation of derived hemodynamic bio-markers such as wall shear forces, pulse wave velocity, pressure gradients and other measures have been proposed (Markl et al. 2012).

Diffusion Tensor MRI **(DT-MRI)** allows the determination of directionality as well as the magnitude of water diffusion. It measures the mobility of the water molecules inside a voxel due to their Brownian motion constrained by the tissue. In this way, the tissue structure surrounding water molecules can be characterized. This description of tissue structure is particularly useful to depict myocardial fiber architecture. Due to the acquisition of several diffusion weighted images with different magnetic diffusion gradients, it has the disadvantage of being too slow to cope with cardiac motion. (Peyrat 2009)

There are other CMRI sub modalities beyond the ones that were described, such as late-gadolinium-enhancement (LGE) imaging for visualizing scarred tissue, coronary MR angiography for visualizing the coronaries, multinuclear spectroscopy for spectroscopic imaging based on Carbon, Sodium, or Fluorine, and first-pass perfusion imaging to visualize the ischemic myocardium (Tavakoli & Amini 2013).

2.4 – Concluding Remarks

This chapter gave a brief overview on the complex anatomy, function and imaging of the human heart, with the purpose of introducing the anatomical, physiological and clinical aspects that will be important for the next chapters. Basically, the heart can be interpreted as a system composed of biological, electrical and mechanical components, each one depending on a variety of parameters, which will rule the performance in terms of blood circulation throughout the body. Among others, the extraction of parameters related to the LV, such as LV volume and pressure, are essential to obtain functional indexes of this chamber, which in turn provide the identification and characterization of pathological states, such as the aortic valve disease.

Noninvasive imaging techniques are vital and have been widely applied to clinical use. Due to its capability to monitor and assess the progression of CVD, cardiac imaging enables more accurate diagnostics and the development of effective procedures for the patients care and treatment. Cardiac image acquisition is specially a complex task, due to the involuntary movement of the heart and the respiratory movement of the thorax, which lead to the improvement of the basic imaging technologies. Nowadays, cine MRI is the gold standard for the assessment of global parameters of cardiac pump function.

The advantages associated to MRI when compared to the other modalities are:

- noninvasiveness,
- nonionizing radiation,
- capability to generate 3D and 4D images with high spatial and temporal resolutions and with good soft tissue contrast,
- possibility to image the heart at arbitrary orientations,
- ability to simultaneously evaluate both structure and function of the heart and
- it is valuable in diagnosing a large range of pathological conditions.

On the other hand, this technology is expensive, not portable, not “real-time”, it has lower resolution than CT and it cannot be used in patients with pacemakers or metal implants.

Chapter 3 - Heart Modeling

The subject of heart modelling is introduced in this chapter with focus on patient-specific cardiac models. Therefore, the scientific concepts, the applications, the challenges and the limitations associated to this task will be presented.

3.1 - Overview

The simulation and the good understanding of the human body anatomy, physiology, and dynamics can be achieved through human body models, where real problems are translated in mathematical language. Computational modeling is the use of mathematics, physics and computer science to study the behavior of complex systems by computer simulation. A computational model contains numerous variables that characterize the system being studied. Simulation is done by adjusting these variables and observing how the changes affect the outcomes predicted by the model (National Institute of Biomedical Imaging and Bioengineering 2013). In most scientific computing applications, a physical system is represented by a mathematical model, where the continuous physical domain is replaced by a discrete representation that is suitable for a numerical solution and can then be used for different simulations. Computer simulations can be applied to a wide range of fields, among them the cardiac electro-mechanical simulations. For a good simulation, a computer mathematical model which imitates a natural situation as close as possible is needed. In the case of the human heart, its irregular 3D shape and dynamics make it difficult to reproduce and to represent as a computer model. The reconstruction of a 4D model of the human heart that is intended for computer simulations can only be achieved with accurate anatomical data that provide detailed heart structure information. Finite element (FE) analysis can be used to model the complex geometry, non-linear material properties and large deformations of the heart, to enable solution of the biophysical conservation laws linking stress, strain and energy expenditure (Young & Frangi 2009).

Human body atlases attempt to provide a “standard” description of the human body or parts of it and have long been used in medicine for anatomical and physiological studies. In the past, those were constructed manually by experts in the field, but nowadays, with the advances in the processing and analysis of biomedical images, the production of digital atlases is a reality. The creation of these atlases requires the availability and processing of a representative dataset, which should include multimodal information and different scales of observation, across large patient populations. By applying parametric mathematical modeling tools, the different imaging modalities and protocols and the different data sources can be fused, enabling an efficient

statistical analysis and representation of regional heart shape and wall motion characteristics (Young & Frangi 2009). The resulting statistical heart models can then be used to reconstruct patient-specific cardiac morphology and morphodynamics from clinical data. For physiological simulations, tissue properties, such as mechanical or electrical properties, or muscle fibers direction in the myocardium, should be integrated in the statistical models. The standard procedure to generate a volumetric anatomic heart model starts with the segmentation and registration of a learning data set (Frangi et al. 2006). This is a crucial phase, since an accurate information extraction from the images is essential for a realistic reconstruction of the heart. In a second step, the resulting set of volume contours are transformed into a surface, represented by a mesh of finite elements. The *Marching Cubes* algorithm is the most essential algorithm to carry out this transformation. When the model is intended for simulations, it requires a mesh with high quality elements (almost isotropic elements), an appropriate number of elements to represent the surface feature and a gradual change of the elements size (Preim & Charl 2013). The final step is the generation of a volumetric grid from the computed surface grid. When dealing with complex boundary surfaces, such as anatomical heart structures, a family of algorithms called *Advancing Front Approaches* is widely used, where the volume elements are generated stepwise starting from the surface mesh (Preim & Charl 2013).

Taking into account that the left ventricle plays the main function on the cardiovascular system, pumping oxygenated blood from the lungs to the rest of the body through systemic circulation, the most important clinical parameters to evaluate the cardiac performance, such as LVEF or LV wall thickening, are derived from the analysis of this chamber. Besides, the efficiency of cardiac pumping function is dependent on blood flow within the LV chamber and therefore, it is essential to accurately characterize LV hemodynamics. The understanding of LV hemodynamics is crucial to improve clinical diagnostic and prognostic information. Consequently, a considerable part of recent work on heart modeling focuses on the computational reconstruction of the LV anatomy and function, in regard to different aspects, such as wall deformation, fluid dynamics, electrical activity or scar tissue characterization.

3.2 - Applications

Modeling of the heart gives access to the cardiac shape, motion, physical structure and associated functional parameters of the heart chambers, including:

- measurement of ejection fraction,
- wall-thickening and wall-motion analysis,
- cardiac output,

- myocardial blood flow and
- mapping of the electrical activity.

These models allow to quantitatively study the physiological and pathological mechanism of cardiac diseases, such as aortic valve diseases, arrhythmias, atrial and ventricular fibrillation, and hence help improve their diagnosis and treatment. Besides the information captured by medical imaging, the models might also contain mechanical and electrical assumptions, providing information that is not directly observable, but has an impact on the disease process, such as tissue stress and measures of pump efficiency. This can play an important role in diagnostic and treatment processes, and even in the development or optimization of medical devices. For instance, models for heart failure and electrical rhythm disturbances incorporate the description of ion channel kinetics into the organ-level solution of reaction–diffusion equations for computing the activation sequences in ventricular and atrial tissue. These applications also couple the mechanisms for myofilament force generation at the subcellular level to the fluid-mechanical properties of the chamber and heart wall to capture contractile dynamics (Smith et al. 2011).

Heart models have their major application in simulation processes, which allows to improve treatment and surgery planning. Model simulations enable physicians to predict the response of a real system that is being study under changing conditions. Some examples of cardiac simulations are:

- computational fluid dynamics (CFD), to access blood flow,
- simulation of electric potential propagation in cardiac tissues, which is of great interest for improving drug design, therapy in arrhythmia or the development of better pacemakers,
- simulation of elastic deformation, which can be applied on the simulation of surgery procedures, such as minimally invasive surgery.

Besides, heart models have been increasingly used to guide invasive therapeutic procedures. It has been proposed, for instance, to overlay heart models onto live fluoroscopy data to support ablation procedures for treating atrial fibrillation (Rhode et al. 2005; Knecht et al. 2008) or stem cell injection for myocardial repair (Gutiérrez et al. 2007; Lehmann et al. 2009). An interactive support can be achieved with real-time modeling, coupling the model with interventional data in order to bring additional information that could not be observed during a medical intervention. For instance, augmented reality (AR) consists in superimposing on the scene that the practitioner perceives additional information coming from a computerized model, usually through visual devices. This enhanced perception proves to be useful in many types of interventions, reducing the invasiveness of the intervention (Blanquer et al. 2004)

Other important applications of heart models are medical teaching and training, and medical research, helping physicians and researchers to better visualize and analyze the heart and allowing them to conduct innumerous of simulated experiments in order to find the better

solution for the problem in hands. It is important to refer that any developed technology or methodology must be validated, in order to achieve credibility and to become clinically applicable.

In 2011, (Trayanova 2011) reviewed the applications of whole-heart modeling in the context of electrophysiology and electromechanics. Later on, (Trayanova et al. 2012)presented a review on the applications on computational cardiology, focusing on the contribution of cardiac modeling to the development of new therapies as well as the advancement of existing ones for cardiac arrhythmias and pump dysfunction.

3.3 - Patient Specific Modelling

The integration of computational heart models with patient clinical data result on numerical models of electrical conduction and of mechanics with patient-specific parameters. These have the potential for predictive use and can largely improve diagnosis, treatment planning and interventions for cardiovascular diseases, such as ventricular restoration, valve replacement or coronary bypass surgery (Ringenberg et al. 2013; Tang et al. 2010). With these patient-specific models clinical experts can personalize mechanical and electrophysiological simulations. For instance, integrating patient-specific myocardium scar location and myocardium thickness in a generic heart model, gives access to personalized myocardial viability, which is essential for electrophysiological simulations targeted to treatments like cardiac resynchronization therapy (Weese et al. 2013). Another suggestive example is the reconstruction and analysis of a patient's infarcted myocardium, which can provide predictive support and guiding for successful ablation procedures (Ringenberg et al. 2012). For personalized cardiac reconstruction, a generic model can be matched to the patient's heart anatomy given by the imaging data: since statistical models provide not only an average layout of the structure, but also encode deviations from this average, it is possible to deform the structure, within statistically justified bounds (Hoogendoorn et al. 2013). The reconstruction through a specific model also enables to represent the finer scale anatomical features that are not captured by the imaging process. For instance, the fast conduction tracts or muscle fiber directions, which are essential in excitation propagation, which in turn is required for personalized simulations. Therefore, a good surface correspondence between the generic model and the patients imaging data is essential (Kaus et al. 2004).

However, generic (or statistical) models require a large dataset that shall incorporate the high level of variability inherent to cardiac anatomy and function (see Section 3.4). In this project, since there was not a sufficient amount of data to construct a statistical LV model, a strategy to reconstruct the anatomy of the inner LV in different phases of the cardiac cycle from MRI data of a child with aortic valve regurgitation was developed. The output consists on geometric and anatomically accurate surface meshes of the LV cavity in 11 phases of the cardiac cycle, which

can be conjugated with other imaging modalities and patient's physiological parameters to analyze the respective blood flow in the LV and ultimately simulate therapies regarding the aortic valve regurgitation (such as valve replacement). Understanding fluid dynamics inside the LV and other cardiac chambers is critical to:

- identify subtle cardiovascular disorders in their early stages,
- optimize treatment of a dysfunctional or failing heart,
- develop better ventricular assisting devices or artificial hearts, and
- further advance the designs of prosthetic heart valves.

The shape, size, and dynamics of the LV and other cardiac chambers, proper mechanical function of the cardiac valves, ventriculoaortic coupling, negative or positive inotropic drugs, and neurohumoral effects are some of the various factors that affect heart function and, thus, intraventricular blood flow.

According to (Borazjani et al. 2013), future research directions to advance patient-specific LV simulations include development of methods capable of :

- resolving heart valves
- achieving higher temporal resolution,
- fully automatically generating 3D geometry, and
- incorporating actual flow measurements into the numerical solution of the 3D cardiovascular fluid dynamics.

3.4 - Challenges and Limitations

Heart modeling, which plays an important role in cardiac healthcare, has undergone a great development in recent years. Nevertheless, the construction of a comprehensive cardiac model, including atria and ventricles, coronary and conduction systems, and fiber orientation still faces a number of challenges and limitations, since it should comprise morphology, material properties, mechanical flow, pressure and stress conditions. The main associated challenges were described by (Tang *et al*. 2010) and (Hoogendoorn *et al*. 2013) and are presented bellow:

- The presence of complex as well as small cardiovascular structures: ventricle geometries are complex, their walls have complex multilayer structure and myofiber architecture.
- Myocardium tissue's mechanical properties and heart motion are complex and involve active contraction and large deformation from different structures (e.g., chambers and valves) and strong fluid- structure interactions.
- Correction of motion-related artifacts originated from the beating heart or from respiration
- High variability in image datasets (intra-subject, inter-subject, temporal and pathological) due to the multi-region nature of the heart with cardiac and vascular structures with

different size and geometry (intra-subject), large global variations throughout the population (inter-subject) and heart motion (temporal).

- Correct topological relationships between the different structures are very important for the model to be used in cardiac simulations. The transitions between structures should be seamless and at same time the mesh quality has to be maintained.
- High variability requires the processing of a large population for statistical modeling, which precludes case-by-case parameter tuning. The need of high-resolution images to accurately extract and represent cardiac features also enlarges the data sets. Besides, accuracy implies fine meshing which requires large memory. Thus, a trade-off between realism and computation has to be found.
- At last, data acquisition under in vivo condition is often difficult mainly due to the coarse slice thickness limitations of current in vivo MRI (Ringenberg et al. 2013).Thus, great part of cardiac models are currently developed and validated using data collected from invasive measurements in animal populations under controlled conditions, which are useful to demonstrate the proof of concept function and development of mechanistic concepts, but not to validate and customize them for human clinical application (Smith et al. 2011).

3.5 – Concluding Remarks

In sum, modeling of the heart has many applications regarding the cardiac personalized healthcare. The main difference between modeling and data processing and analysis is the use of computational methods for predictive purposes, providing physically accurate information that is not contained in the medical data themselves. Nevertheless, image processing and analysis, particularly segmentation and registration, are essential to extract detailed heart structure information and to circumvent the problem of high variability, respectively. Although many research in this area has been done, resulting in cardiac models with acknowledge clinical importance, there are still many challenges that have to be overcome in order to achieve a translation into clinical applications.

Chapter 4 – Related Work

In order to improve diagnosis and treatment of cardiac diseases, cardiac reconstruction, either static (3D) or dynamic (4D), has been a subject of intensive research in the last decades with an enormous amount of published work, where a great variety of methods to process images from different modalities and other clinical data are developed to obtain cardiac models for different medical applications. (Frangi et al. 2001) provide a comprehensive survey of the developed work prior to 2001, focusing on 3D cardiac modeling techniques, classified in surface models, volume models, and deformable models and based on different modalities, namely angiography, cardiac US, isotope imaging, cardiac CT, and MRI. In the remainder of this chapter, the published work on cardiac modelling in the past six years that has been relevant to the development of this project is reviewed. It focuses on projects that involved the reconstruction of the left ventricular anatomy and simulation purposes.

4.1 – Recent Work on LV Reconstruction for Simulation Purposes

Recently,(Tang et al. 2010) gave a brief review on the development in ventricle modeling and its potential application in surgical planning and management of tetralogy of Fallot patients, considering the following aspects: data acquisition, model selection and construction, material properties of the tissue, ventricle layer structure, tissue fiber orientations, pressure condition, model validation and virtual surgery procedures (changing patient-specific ventricle data and performing computer simulation). In 2011, (Trayanova 2011) discussed the state-of-the-art in whole-heart modeling and its applications in cardiac electrophysiology and electromechanics research, focusing only on ventricular models, since the ventricles are the major pump, as well as the perpetrator of the most lethal arrhythmias.

A common approach to extract a cardiac surface from CMR images relies on the following three main phases:

1. segmentation of ROI,
2. registration of images and
3. surface mesh extraction from labeled region.

Depending on the goal of the surface mesh to be computed and on the available dataset in terms of type, quantity and quality, different techniques have been developed for each phase of the computational cardiac reconstruction. The remainder of this chapter provides an overview of the developed work regarding cardiac modeling in the last years, giving special attention to the projects that focused on the geometric reconstruction of the LV anatomy.

In order to explore the correlation between function and anatomy for a given patient and test different hypothesis and plan therapies, a framework toward patient-specific models of the myocardium, integrating information about the anatomy, the electrophysiology, and the mechanics, was presented by (Sermesant et al. 2008). The patient-specific myocardial shape was developed by adapting a biventricular mesh to preliminary segmented (3D) MR image of the ventricular cavity of a given patient. Deformable models evolved under the influence of both external forces, computed from the preliminary segmentation (voxel labeling based on intensity), and internal forces, computed from the laws of mechanics. The difference in intensity values of myocardium and blood pool enabled a first extraction of the ventricular blood pools with a region-growing approach. For each ventricle, it was necessary that the user interactively placed a few control points to define the valve annuli and initial seeds inside the cavities. The algorithm automatically expanded the seeds and consequently, the voxels with similar intensities were covered, resulting in a 3D surface representing the preliminary segmentation. Afterwards, a deformable surface mesh was used to enforce the right topology and smooth the borders. In order to extract the endocardial surfaces from each image of the sequence, the mesh was propagated along the time sequence, where an internal force ensures its smoothness while a region-based external force made it evolve according to the image gray-level intensities. In this way, the 3D labeling of both left and right blood pools in each cardiac phase was obtained. To complete the personalization of the model, the shape model was combined with the developed electrophysiological model and with personalized biomechanical parameters. Finally, to illustrate the overall framework, the LV function of a patient with valve regurgitation was simulated by adjusting the electromechanical model to the patient's data, resulting in the visualization of simulated contraction at each vertex of the mesh, electrical propagation, and the 3D strain in real time to assess the cardiac function.

With another scope, (Tang et al. 2010) also combined different personalized cardiac features. The scope was to develop a model that included right and left ventricles, patch and scar tissues, isotropic and anisotropic material properties, two-layer structure, fiber orientation, and passive and active contractions, in order to evaluate and optimize human pulmonary valve replacement/insertion surgical procedure and patch design. The RV/LV 3D geometry was reconstructed from segmented contours of SAX cine MR images under the ADINA computing environment. The shape model included patch, scar, and valve positions and was conjugated with a fluid model, a passive and an active anisotropic solid models and a two-layer model with fiber orientation. The final model was used to compute 3D flow, deformation and stress-strain distributions that served as basis for the investigations related to the surgical procedure.

A detailed investigation of left ventricle (LV) flow patterns in normal subjects was performed by (Long et al. 2008), by means of patient-specific modelling from MR images. In the study, the

prescribed LV wall movements based on the MRI measurements drove the blood flow in and out of the LV in computational fluid dynamics simulation. The simulated flow patterns were positively validated with MRI-measured flow fields from MR phase contrast velocity maps. To generate a 3D smooth and structured computational LV cavity mesh, multi-slice cine MR images of the LV including inflow and outflow tracts were acquired and segmented. For the creation of the 3D LV model, constructive solid geometry was used to describe the complex ventricular morphology as the combination of a set of simple geometric primitives computed from a set of arbitrarily placed control points. A total of 16 meshes were generated from the original image data in one cycle, which afterwards were used to compute temporal cubic spline interpolation in order to generate a complete time series of models. The resulting meshes were used for CFD simulations, providing complete spatial and temporal coverage of the LV. In addition the full 3D motion of the valves was also modelled and used to define the extent of the LV at different phases of the cardiac cycle.

Recently and also in the context of CFD, (Nguyen et al. 2013) presented a semi-automated method to conduct geometry reconstruction, LV mesh smoothing and CFD simulation. The reconstruction of 3D LV geometry from SAX and LAX MR images was accomplished using CMRtools suits (CVIS, Imperial College, UK) in combination with the algorithm used in the aforementioned work of (Long et al. 2008). LV geometries served as input of the developed method that started with a smoothing process using subdivision surfaces, eliminating rough edges. In order to perform CFD simulations of intra-ventricular flows, unstructured tetrahedral meshes were generated from the smoothed and refined surfaces, using the Delaunay triangulation algorithm. The motion of LV walls captured in the raw images was translated into dynamic motions of mesh boundaries using fast radial basic function (RBF) interpolation. The parameters associated to the wall motion, namely the wall velocity, and the tangential and normal unit vectors to the wall, were used as wall boundary conditions for simulations of blood flows over a cardiac cycle taking into account the pumping motion of LV walls. Despite the positive results, the method was only applied to a single volunteer, which hampers the generalization of the method. Besides, the authors still need to achieve in vivo validation of the flow pattern results to enable the translation of the method into clinical practice.

The functional effects resulting from the geometrical change found in the LV after surgical ventricular restoration (SVR) were studied by (Lee et al. 2013), who conducted the first mathematical analysis on the effects of SVR using patient-specific finite-element LV models. These models were created using untagged MR images at early diastole, which were segmented interactively by outlining the LV endocardial and epicardial borders (excluding papillary muscles and trabeculation) using CMR tools. Using Rapidform (INUS Technology), the 3D LV epicardial and endocardial surfaces were reconstructed by triangulation of the set of LV contour points derived

from the segmentation process. Afterwards, a mesh was projected between the reconstructed 3D endocardial and the 3D epicardial surface, leading to FE models of the LV, suitable for the mathematical analysis.

The cardiac resynchronization therapy (CRT) was subject of study of (Niederer et al. 2012), which integrated multiple diagnostic data sets into a biophysical computational modeling framework to determine the distribution of local active tension or work in the heart pre and post CRT. The personalized human heart model was created by manual segmentation of end diastolic cine MRI data and construction of a tri-cubic Hermite mesh and was used for simulating mechanical deformations. For simulating cardiac electrophysiology, a second, higher resolution, tetrahedral element mesh, was constructed, where the fiber orientation was derived from animal studies augmented with human data. Late enhancement MRI studies were used to identify regions of myocardial scarring. The shape model was combined with a set of biophysical parameters to simulate electrical activation and mechanical deformation.

(Nickisch et al. 2013) took advantage of model-based segmentation to obtain a personalized model for subsequent biophysical simulations of the heart. The goal was to encode in the patient-specific model structures that are important for excitation propagation, but are hardly identifiable in clinical images, such as the fast conduction tracts or muscle fiber directions. In this approach, a generic model consisting on a mesh that carries the additional electrophysiological information is adapted to the patient's images for segmentation. The positions of the structures in an average anatomy can be obtained from histological studies or specialized measurements beforehand. During the adaptation of the segmentation mesh to image data, the structures are deformed in the same way as the mesh, resulting in a personalized model for subsequent cardiac simulations.

In regard to model-based cardiac segmentation, a recent work from (Tavakoli & Amini 2013) presents a survey of shape modeling applications to cardiac image segmentation and registration from MRI, CT, US, PET, and SPECT. The reviewed techniques were categorized into statistical models, deformable models/level sets, biophysical models, and non-rigid registration using basis functions. In sum, the four categories for heart segmentation present advantages and drawbacks. Statistical methods are independent of image intensity, but require a training phase with a large dataset. Deformable models are versatile and match specific shapes and energy function, but they depend on parameters and are sensitive to noise. Biophysical models are also intensity-independent and they don't require training. Nevertheless, they violate the physical assumptions and are dependent on parameters. At last, non-rigid registration using basis functions, present smoothness and have the potential to be used for a variety of modalities and objects, without a training phase. On the other hand, this method contains convergence issues and depends on

parameters. However, the boundaries of each class are not fixed and many authors combined them to circumvent the challenges associated to the task of cardiac modeling.

Considering the motion related artifacts in 3D MRI images that can affect the correct geometrical representation of the LV, (Tan et al. 2013) proposed an automatic algorithm that uses a geometry-driven optimization approach to restore the shape of 3D left ventricular models created from MRI data. The main goal was to restore the LV shape such that the LV epicardial surface was smooth after the restoration and that the general shape characteristic of the LV was not altered. Therefore, the minimum principal curvature was used as a quantification of the surface smoothness and a limited memory quasi-Newton algorithm, was used to correct the positions of all SAX- slices to achieve an optimal shape with minimal concavity. The authors observed improvements in the smoothness of the LV mesh (in terms of concavity) with a preserved overall shape of the LV mesh without over smoothing.

Regarding the surface mesh generation from segmented images, the most widely used method is the *Marching Cubes* algorithm. However this method generates meshes with strong irregular triangles and pronounced stair-case artifacts, when applied to an image with strongly anisotropic voxels without any additional processing (Preim & Charl 2013). To overcome this problem and improve mesh quality, a number of techniques, including mesh smoothing, simplification and optimization (and even combination of the techniques) can be applied. In this context, (Skrinjar & Bistoquet 2009) proposed a different approach for surface mesh generation of the epicardium and endocardium of the four cardiac chambers. Therefore, a premeshed sphere was mapped to the surface of the segmented volume object. The mapping was defined by the gradient field of the solution of the Laplace equation between the sphere and the surface of the object and resulted in smooth meshes despite the strong voxel anisotropy.

A proof-of-concept simulator for cardiac excitation and contraction in the human heart was presented in the Living Heart Project by (Baillargeon et al. 2014), in order to understand the key features associated to the creation of an integrative and predictive model of the living human heart. The spatio-temporal evolution of electrical potentials and mechanical deformation across the heart were simulated in the developed heart model with all four chambers, connected through four valves. Therefore, the underlying geometry from the 3D anatomic model of the human heart extracted from CT and MRI images by (Zygote Media Group and Inc. 2013) was adapted, to create a solid model, a finite element model, and a muscle fiber model. The circulatory model from (Zygote Media Group and Inc. 2013) was also adapted, in order to obtain a blood flow model. By the combination of these models, the authors were able to extract two common metrics of cardiac function, namely the long-axis shortening and pressure-volume loops, which agreed well with clinical observations. Nevertheless, taking into account the variety of

simplifications (biological, mechanical and electrical) assumed in the model's construction, the authors presented a list of necessary improvements to accomplish a more realistic simulator of the human heart.

In the context of cardiac modelling it is indispensable to refer the euHeart project (http://www.euheart.eu/), a recent European research initiative (carried out from 2008 until 2012) that focused on the methods for personalizing cardiac simulations for diagnosis improvement, treatment planning and delivery, and optimization of implantable devices of cardiac resynchronization therapy, radiofrequency ablation, heart failure, coronary artery disease and aortic and valvular diseases. The project significantly advanced the state-of the-art in cardiac simulations, but due to the reduced number of patient cases in which the simulations were performed, the clinical validation and the translation into clinical practice was not accomplished. The image analysis methods developed in this project were reviewed by (Weese et al. 2013) demonstrating that the use of biophysical or physiological constraints in image analysis has the potential to improve data interpretation in many case.

4.2 - Concluding Remarks

This brief overview on the state-of-the-art of cardiac modeling, let us conclude that recently a large amount of work has been dedicated to the development of methods that allow the creation of cardiac models suitable for personalized simulation. Nowadays, the focus is on models that are able to represent not only the anatomy of the heart, but also its electrophysiology, its mechanical behavior, and the alterations caused by pathologies and surgeries. Medical images allow the extraction of very important cardiac information, such as anatomy and flow patterns, but, in order to achieve more realistic cardiac models and simulations, many mathematical and biophysical models, describing the heart's performance, must be integrated.

Notwithstanding the enormous progress made in this field, the full automation and the translation into clinical practice remain challenges to be overcome.

Chapter 5 - Materials and Methods

The goal of this dissertation is to develop a strategy for the anatomically accurate reconstruction of the inner LV geometry in different phases of the cardiac cycle. The input consists on spatio-temporal MR images and the output shall consist on temporal 3D surfaces, describing the anatomy of the LV endocardium accurately and with a mesh suitable for FE analysis. The resulting surface meshes will support blood-flow analysis and simulations in the context of aortic valve disease (AVD). This chapter reports how this task was accomplished and for each methodological step, the main goal is presented and the methods used to achieve it are described in detail. All the materials, including software, hardware and dataset, used for the development of this project are also reported.

The developed framework to reconstruct the inner wall of the LV in different phases of one cardiac cycle as geometric surface meshes is represented in Figure 5.2 by means of a pipeline. Briefly, transversal-, short- and long-axis (TRA, SAX and LAX, respectively) cine-MR images in conjunction with static 3D-whole heart (3D-WH) MR images were processed and combined to obtain an anatomically accurate surface of the LV cavity in eleven cardiac phases. A static 3D LV surface is extracted from one scanned time instant of the cardiac cycle and then, this is used to support the construction of smooth surfaces from the remaining scanned cardiac phases.

5.1 - Materials

The cardiac MR (CMR) study was conducted on a whole body 1.5 Tesla MR scanner (Achieva R 3.2.2.0, Philips Medical Systems, Best, The Netherlands) using a five-element cardiac phased-array coil (Philips Medical System, Best, The Netherlands). The images' visualization, analysis and processing were performed in a standard personal computer running under Windows 7.

The acquired images were stored in DICOM (Digital Image and Communication in Medicine) format files and each patient's study was stored in a DICOMDIR format file (a media directory, which provides index and summary information for all the DICOM files on the media). Afterwards, the images were imported into the MicroDicom Viewer Software. This is free software (http://www.microdicom.com), which allows the opening of DICOM and DICOMDIR files and provides the common tools for manipulation of DICOM images. Taking into account that many MRI sequence types were applied to each patient, those that could be relevant for the LV reconstruction had to be identified and selected using this software.

The image processing and LV surface reconstruction was computed in ZIBAmira (http://amira.zib.de), a software platform for 3D and 4D data processing, analysis and

visualization. This software was the main tool used for the project's development, allowing, among other processing tasks, image segmentation and registration, surface generation, volume rendering, metrics measurements, remeshing and animated 3D visualization.

5.2 - Dataset

The data provided by the DHZB consisted on cardiac MR DICOM images from 4 anonym patients with an aortic regurgitation or aortic stenosis, who gave informed consent to utilize their medical data in this project. The patients were submitted to MR scans according to the sequences prescribed in the work-flow and scan protocol for the study of this disease. Thus, each patient DICOMDIR file consisted on a series of different MR sequences, from which the ones that enabled a good visualization of the LV anatomy and motion were selected, namely:

- the 3D-WH, (voxel size in mm (VS): 1.42 x 1.42 x 2),
- the cine-SAX, (VS: 0.875 x 0.875 x 7),
- the cine-TRA, (VS: 1 x 1 x 6),
- the cine-2CH (2 chambers: LV + LA, VS: 1.3 x 0 x 1.3),
- the cine-3CH (3 chambers: LV+LA+RA, VS: 1.3 x 1.3 x 0) and
- the cine-4CH (4 chambers: LV+LA+RV+RA; VS: 1.35 x 1.35 x 0) sequences.

All patients' images were observed in the MicroDicom software and the patient that presented images with fewer artifacts was selected to develop a methodology for the LV reconstruction. The selected patient is an 8 years old child with aortic regurgitation, weighting 31 kg and with a heart rate of 73 bpm.

The volume acquired with the 3D-WH sequence is composed of 80 axial slices with 2mm of thickness, covering the whole heart, in the three main directions (feet-to-head, anterior-to-posterior and right-to-left), scanned at the beginning of the R-wave on the ECG (between the end of the diastole and beginning of the systole). The dynamic cine-SAX sequence captured the heart's anatomy from the apex to the aortic arch in the short-axis direction in 14 slices with spacing of 7 mm, whereas the cine-TRA sequence only scanned the cardiac anatomy from the mid-level heart to the aortic arch into 30 transversal slices with 6 mm of interval. The long-axis (LAX) cine-sequences returned cardiac images of a single cut-plane, where the corresponding chambers (2CH, 3CH and 4CH) and respective valves are visible. Except for the 3D-WH sequence, the images in each slice position were acquired during 5-to-10s breath-holds capturing 25 cardiac phases over the heart cycle, with a temporal resolution of 33 ms given the patient's heart rate. The first frame of each temporal MRI sequence (cine-sequences) is always scanned at the beginning of the R-wave on the ECG. Figure 5.1.1 shows a representative slice from the set of images acquired in the first time instant of each MR sequence. The relative orientation between them can also be observed.

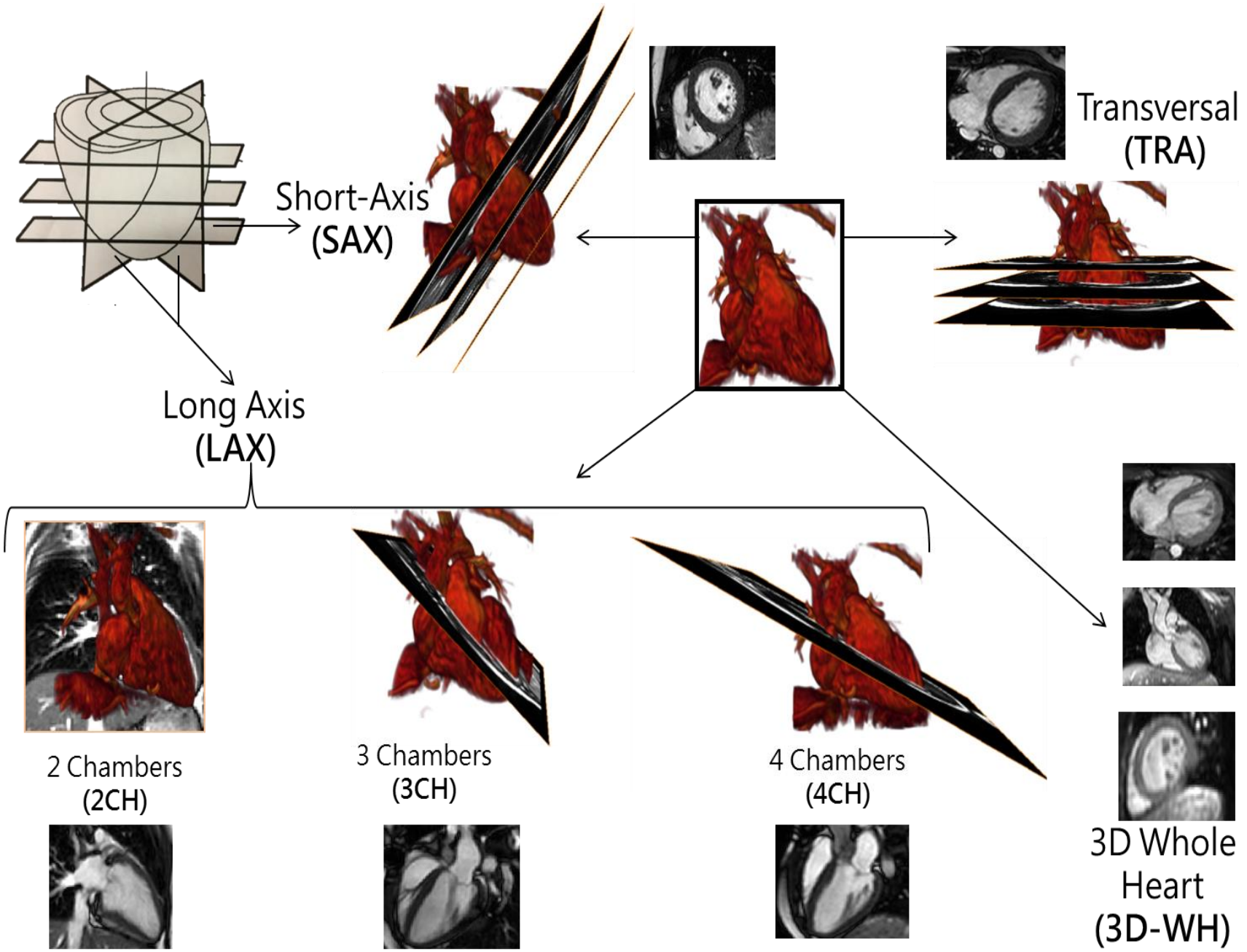

Figure 5.1.1 – Examples of images from the CMR sequences used for the reconstruction of the inner LV.

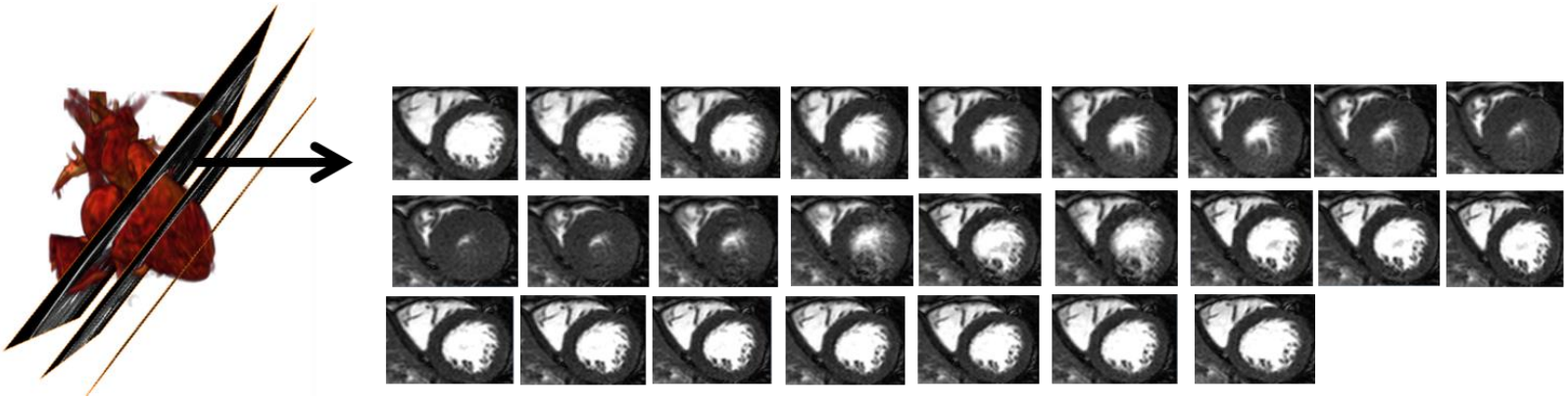

Figure 5.1.2 – Example of a cine-SAX MRI sequence from a mid-heart slice, capturing 25 instants of the cardiac cycle.

5.3 - Brief Overview

Figure 5.2 depicts the developed framework for the reconstruction of the LV surface. The visualization, processing and analysis methodologies were conducted under the software Amira and will be described in detail in the following sub-sections.

To reconstruct the first static 3D model of the LV surface (Phase A), the first frame of each temporal MRI sequence (which correspond to the images scanned at the beginning of an R-wave in the ECG) was used. The process started with the manual registration of the images from the different MR sequences. Afterwards, the inner LV region in all images was interactively segmented and, in the 2D-LAX images, the respective contours were extracted. Those were used to guide the correction of slices' displacements in the static 3D SAX and TRA images, caused by the patient's motion, in order to obtain a restored and smooth endocardial surface, without motion-related artifacts. With the purpose of combining the anatomical information present in the different types of MRI sequences, the transformed TRA and SAX inner LV labels were fused with the 3D-WH label into a single LV label. The fused label served as input data for the generation of a preliminary surface, which required a smoothing process. Finally, the surface mesh quality was improved in terms of elements' isotropy, so that it was suitable for the computation of blood-flow analyses and simulations. The surface area and respective enclosed volume, before and after shape restoration, labels' fusion and surface smoothing were extracted, in order to analyze the impact on the surface of the respective applied techniques.

In a second phase (Phase B), the LV surfaces from other instants of the cardiac cycle were reconstructed. To capture the natural deformation of a beating heart, it was enough to reconstruct the LV surface in 10 more time points (TPs) along the cardiac cycle. Therefore, the SAX and TRA images from each of these 10 time instant were interactively segmented, but the transformations applied to each slice were performed automatically, using as reference the transformations applied to the correspondent slice of the first TP (from Phase A). The results were evaluated qualitatively, by visual inspection, and quantitatively in terms of surface area, enclosed volume and respective variation during one cardiac cycle.

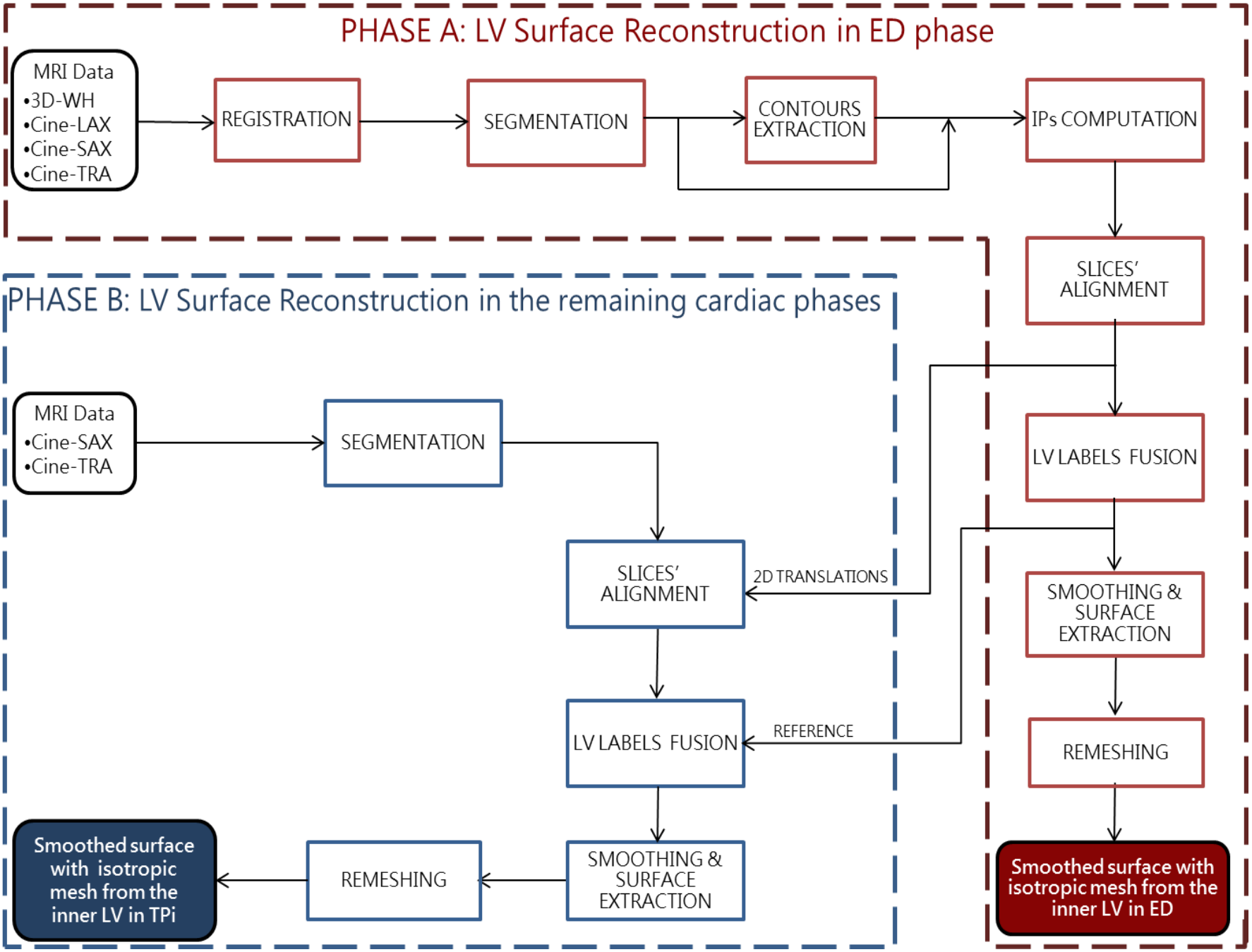

Figure 5.2 - Pipelined framework developed for the geometrical reconstruction of the inner LV anatomy in 11 phases of the cardiac cycle (LV: Left Ventricle, ED: End Diastole IPs: Intersection Points, TP: Time Point).

5.4 - 4D Inner LV Surface Reconstruction

Each phase of the framework presented in Figure 5.2 will be described in detail below. The final surfaces should represent the inner LV anatomy accurately and the respective mesh should be suitable for posterior cardiac blood flow simulation.

5.4.1 - Phase A: Inner LV Surface mesh generation in the ED phase

The first phase of the 4D inner LV reconstruction consisted on the development of a framework for the surface mesh construction of the LV endocardium from the images acquired in the first TP of the cine sequences, which corresponds to the beginning of the R-wave in the ECG. The reason to start with this TP is that it is the only instance of the cardiac cycle also scanned by the 3D-WH sequence. Besides, during the captured cardiac phase, usually between the end of the diastole and the beginning of the systole, the LV is in its maximum state of dilatation and the respective captured images present the LV filled with blood and with low flow velocity. Consequently, in general, the endo- and epicardial contours are well represented along the whole ventricle. On the remainder of the presented document, this cardiac phase, captured during the first MRI acquisition TP, will be mentioned as end diastolic (ED) phase, although it can also correspond to the initial systole. The distinction of the two phases is hardly performed by visually inspection of the images, since the region corresponding to the LV blood pool in these consecutives phases is very similar.

A.1 Visual Inspection of DICOM images

The images from each sequence in the ED phase were loaded into *Amira*, resulting in 6 objects in the *amira mesh* format. Three of these objects, namely the 3D-WH, the SAX and the TRA, consisted on a stack of images, whereas the other three objects, the 2CH, 3CH and 4CH contained a single image. The attachment of the *orthoslice* module to an object, allows the visualization of each slice from an object in the three main orientations (*Axial*/*xy*: slices are perpendicular to the z-axis, *coronal*/*xz*: slices are perpendicular to the y-axis, and *sagittal*/*yz*: slices are perpendicular to the x-axis). In order to rapidly identify the LV cavity and respective contours, the enhancement of the LV blood-pool was performed by manually controlling the displayed gray level (GL) range. The data values can be mapped to colors or GL by one of two mapping methods. The less complex mapping technique uses an external colorfield with two threshold values selected by the user. The default colormap is a linear gray ramp, so the range determines which data values are mapped to black and which are mapped to white. In the case

of cardiac images, this enhancement of the LV blood-pool was achieved, by limiting the grey-level range to a short interval of intermediary values. For instance, in a mid-SAX-image with a GL range from 0 to 2818, the blood pool can be enhanced by converting the colormap range into values from 400 to 800 (as shown in Figure 5.3, the GL above 800, which correspond to the blood-pool, are mapped to white, and the ones below 400, such as the myocardium, are mapped to black).

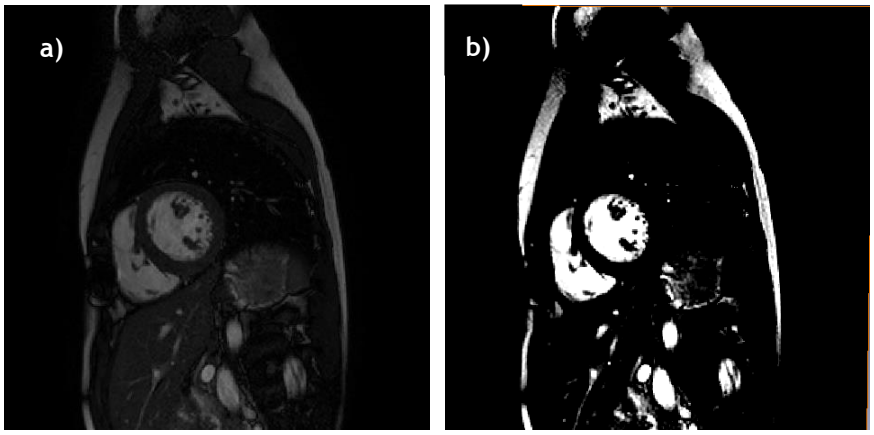

Figure 5.3 - Enhancement of the cardiac blood-pool by changing the colormap range from 0 to 2818 (a) into 400 to 800 (b).

A.2 Pre-Processing: Sequences Registration

The goal of this phase was to correct possible misregistration artifacts among the sequences, due to patient's motions during acquisition, or due to different positions of the thorax during each breath-hold. Therefore, the 3D-WH stack was used as reference, since this was the first acquired sequence and it presents the highest out-of-plane resolution (2mm), allowing a higher number of intersection lines between the reference images and the images to be registered. First, the 2CH, 3CH and 4CH images' position was manually corrected in form of a 3D translation by moving the images in the rendering scene until the best matching among them and with the 3D-WH stack was reached. The best matching criterion consists on the intensity similarity between the images with different orientations in the respective intersection lines, taking the contours regions in higher consideration. If necessary, the same method is applied to correct the position of the SAX-and TRA image stacks, but therefore, the previously corrected 2CH, 3CH and 4CH are used as reference, since they have a higher in-plane resolution and they are already registered with the 3D-WH stack of images.

A.3 Inner LV Segmentation

The inner LV was interactively segmented in all sequences with Amira's Segmentation Editor, illustrated in Figure 5.4. Here, the segmentation is done by first selecting voxels and then assigning these voxels to a particular material, in this case the *innerLV*. The resulting labels are stored in a *LabelField*, which can always be edited with the Segmentation Editor.

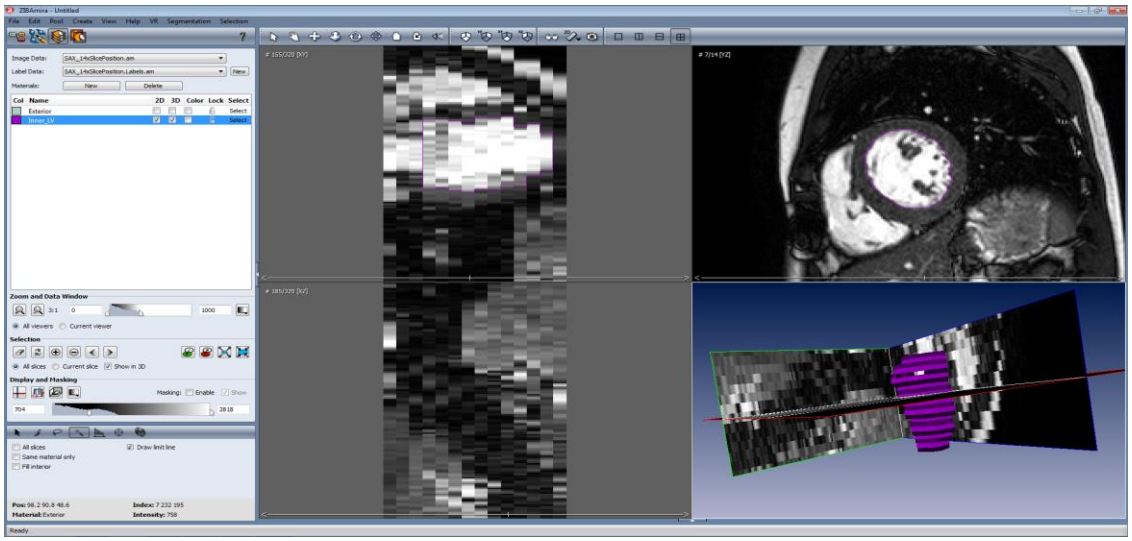

Figure 5.4 – Amira's Segmentation Editor.

The reasons why it was opted for an interactive instead of a full automatic method for the segmentation are listed below:

- the provided data consisted on CMR images from only 3 patients, an insufficient amount of data for the development of automatic methods that require a training dataset or prior information, such as statistical models (Petitjean & Dacher 2011);
- insufficient data to validate a developed automatic method;
- the Amira *Segmentation Editor* provides many interactive, effective and efficient tools for this purpose and allows the editing of the label field at any time.

Before starting the segmentation, the view orientation, where the images have higher resolution is selected and the images' brightness and contrast are changed, by adjusting the histogram range to be displayed, in order to enhance the LV blood-pool. Afterwards, a mask, which GL range can be specified by means of a slide bar, is applied to the data, so that the whole inner LV in all images becomes "masked". This is very useful for the selection step, because only the "masked" voxels can now be selected. The *Segmentation Editor* offers many tools for the selection task, from which the *magic wand* and the *brush* were used. The first tool performs a so-called R*egion Growing* either in 2D or in 3D. Clicking with the mouse on a voxel selects the largest connected area that contains the voxel itself and all connected voxels previously masked

and connected. The *fill interior* toggle is set, so that holes inside the selected region are filled automatically. Automatic filling is only done in 2D mode and it removes islands of arbitrary size in the current selection, adding all pixels completely surrounded by the already selected pixels to the selected area. This allows the inclusion of the papillary muscles that are inside the inner LV region, but not on the inner LV periphery. Finally, the *draw limit line* button lets the user specify additional barriers for 2D R*egion Growing*, by drawing arbitrary polylines in the viewer window. Voxels covered by such a limit line will not be considered for region growing. For example, in the basal-SAX-slices, the applied mask also masks pixels of the LV wall and a line is drawn to limit the region growing to the inner LV area (Figure 5.5).

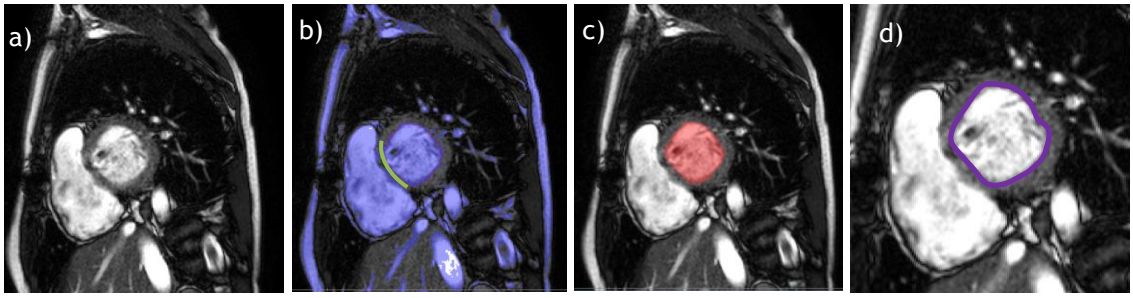

Figure 5.5 – Segmentation Process: a) original image, b) masked image, with drawn limit line in green, c) selected region, d) segmented region with respective contour in purple.

In sum, the pixels that correspond to the inner LV in an image stack are selected by selecting a seed point in one slice and drawing some limit lines in the basal slices. Since this selection is based on GL values, the peripheral papillary muscles and trabeculations are excluded and consequently, the outer contour of the inner LV label becomes very irregular. As recommended by the cardiac imaging experts involved in this project, the papillary muscles and trabeculations that are totally surrounded by blood in the inner LV should be consider as part of this volume, but if they are connected with the LV wall they should be excluded, except for very small/thin connection. Thus, to smooth the periphery of the selected region, the *brush* tool, which allows voxel selection by painting them with a brush of adjustable size, is used and the small size peripheral muscular areas are added to the selected region. The last step consists on adding the selected voxels to the desired material, namely the *innerLV*. In the *Segmentation Editor*, the segmented region can be visualized by means of contours on the respective slices in the 2D-viewers or as a point cloud overlaid on the slices in the 3D-viewer, facilitating the detection of necessary segmentation corrections (Figure 5.4).

A.4 Exclusion of irrelevant slices

After the segmentation process, the slices that didn't contain any label were removed from each stack of labeled images (with *Amira*'s *Crop Editor*), in order to discard irrelevant information and reduce the computation cost.

A.5 Extract Contours

The contour from the 2CH labeled image was extracted with the module *ComputeContours*. It computes contours for a 3D label set using 2D cutting planes orthogonal to the desired local axis (x, y or z). In this case the cutting plane had the same coordinates as the 2CH slice. It results in a *LineSet* data object, where the independent line segments are stored. To visualize the resulting object, the modules *LineSetView* and *LineRaycas*t, can be used. They present many parameters, such as line radius or line color, which can be adjusted to obtain a better representation. Afterwards, the contours from the 3CH and 4CH labeled images were computed in the same way.

A.6 Contours' Intersections with the 3D SAX image

The goal of this step was to obtain a stack of images containing not only the SAX's inner LV label (*innerLV)*, but also the respective intersection points with the three contours extracted from the *innerLV* in the 2CH, 3CH and 4CH images. Later, this stack will be used to correct the in-plane position of each SAX labeled slice. To compute the intersections, the *LineSet* objects were converted into objects of type *SpatialGraph*, with the same geometry as the *LineSet* and with all lines mapped to segments (edges), which three dimensional course is given by a sequence of points in 3D space. The segment density (total segment length) contained within each grid cell in a uniform grid was computed with the *SpatialGraphDensity* module, where the grid cell size was set to 0.5 mm in the three directions, in order to obtain an accurate representation of the contours in the form of slices (voxel size in mm: 0.5 x 0.5 x 0.5). Afterwards, these images were added to the 3D labeled SAX image, in order to obtain a stack of SAX labeled images with the intersection points (IPs) that represent the 3 long-axis (LAX) contours (Figure 5.6).

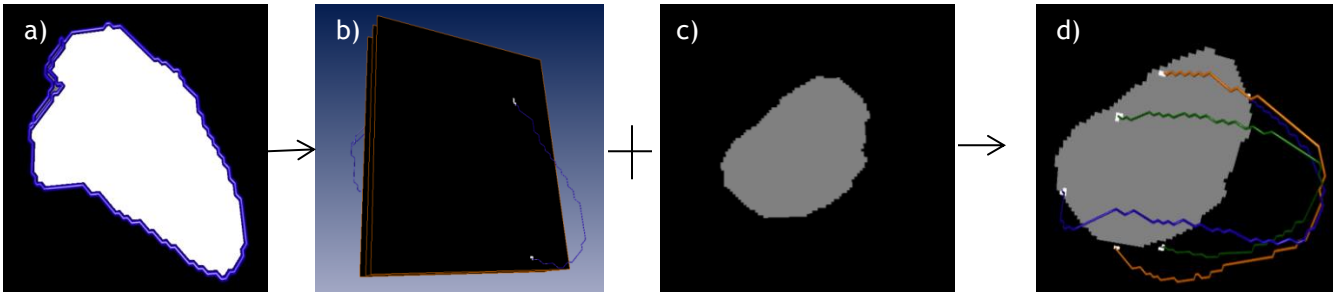

Figure 5.6 – Process to obtain a stack of labeled SAX (or TRA) images and the correspondent intersections with the LAX contours. a) The 2CH LV label and respective contour in blue, which is converted in a spatial graph (b) 3 representative slices of the 3D spatial graph extracted from the 2CH contour *lineset* (in blue)) . The spatial graph is added to the labeled stack represented in c) by a labeled slice from the TRA stack. The same process is applied to the other LAX contours and the final result is represented in d) with an example of a TRA labeled image with the respective IPs (white) extracted from the 3 LAX contours that are also represented (in orange green and blue).

A.7 Slices' Alignment

The fact that each 2D SAX and TRA dynamic image is acquired with ECG-triggering during different patient's apneas and the consequent non-exact repeatability of breath-holding maneuver over all acquisitions leads to relative displacement between slices. For 3D reconstruction of cardiac shape and deformation it is mandatory to correct these misregistration errors (Figure 5.7).

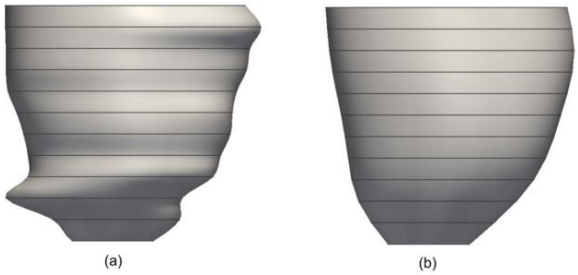

Figure 5.7 – 3D left ventricle shape models, (a) with motion artifacts, and (b) desired result after shape restoration representing the natural asymmetric shape of the ventricle (Tan et al. 2013).

In Amira, the *AlignSlices* module, computes an automatic alignment of two adjacent slices (or of the whole image stack), applying algorithms based on the *least-square distance* or on the *center-of-gravity*. However, taking into account that the general shape of inner LV does not present symmetrical configuration in the long-axis direction (Figure 5.7), neither a completely circular shape along the short axis, due to the intrusions of papillary muscles in the LV wall, the available algorithms in Amira for slice alignment could not be used for this purpose. Therefore, the goal of this step was to correct the position of each SAX-slice by aligning them with the contours previously extracted from the LAX sequences' images, generating a stack of SAX images, in which the *innerLV* is aligned with the labels from the 2CH, 3CH and 4CH images. This task was

performed interactively using the *AlignSlices* module, which also allows manually controlled in-plane transformations of each slice in a stack. The slices' alignment was guided by the intersection points extracted from the LAX contours. The goal was to, in each slice, minimize the overall distance of the labeled region to the respective intersection points. Since the *AlignSlices* module overlays two consecutive slices and one of them is chosen to suffer a transformation (the lower slice), the IPs of the lower slice to be transformed had to be represented on the one that would not suffer the transformation (the upper slice), so that their position was not altered and they could be used to guide the necessary correction/translation of the lower slice. Therefore, the stack of images containing the IPs was translated 7mm (the SAX-voxel high) upwards, and was then added to the labeled SAX-stack, in order to obtain a stack of images, where each slice contained the own *innerLV* region and the IPs of the previous slice. This stack served as input data for the *AlignSlices* module. The process started by displaying simultaneously the two first slices in the apex and then the lower slice was manually translated in the plane so that the distance between the IPs (represented in the upper slice) and the inner LV label was minimal (Figure 5.8).

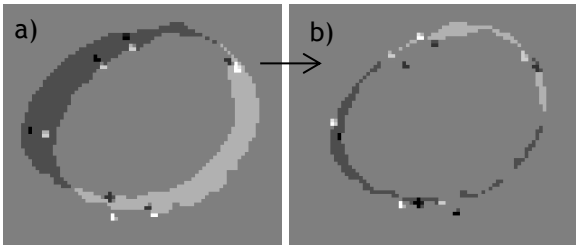

Figure 5.8 –*AlignSlices* module Viewer showing the inner LV labels of two consecutives mid SAX images (gray) and the IPs (black and white). The goal is to translate the lower slice (darker gray label), so that its distance to the white points in a) (represented in the upper slice) is minimal. The desired result is illustrated in b).

The same method was applied to correct the position of the following slices. The final output consisted on labeled images with corrected position, but also containing the IPs. Thus, the transformation applied to each single slice in this stack was copied to the labeled SAX-images by attaching to the *AlignSlices* module a reference 3D field (the previous output) from which the 2D-translation applied to each slice in the stack is read and transferred to the respective image in the field that must be transformed (the labeled SAX-stack).

A.8 Evaluation of Shape Restoration

In order to visualize the effect of the slices translations, the transformed images were superimposed on the original labeled images, using the *Colorwash* module attached to the *Orthoslice* module. With the *Colorwash* module, the original labeled image displayed by the *Orthoslice* is modulated so that it also encodes the second field, the transformed labeled image.

The modulation technique *Label Blending*, combines the images in a way that the label of the transformed images appears overlaid and colored on the respective original labeled images. The transparency of the colored image can be controlled by a slider, which facilitates the comparison of the labels' position. The contours were also displayed, allowing a better evaluation of the slices' alignment (Figure 5.9).

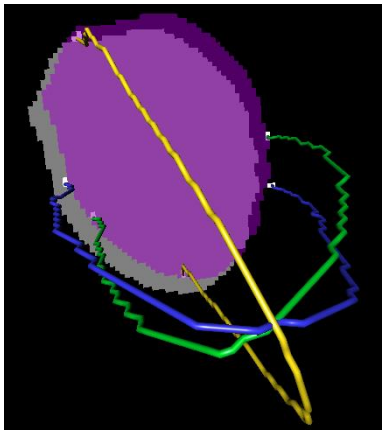

Figure 5.9 – Visualization of the inner LV label of a representative SAX slice in its original position (grey region) "colorwashed" with the 2D-translated one (purple region). The distance of the label boundary to the contours is compared in order to evaluate the translation.

The segmented 3D-WH images were also used to evaluate the slices' alignment. Therefore, the volume between the 3D-WH *innerLV* and the **original** SAX-*innerLV* was obtained and compared to the volume between the 3D-WH label and the **transformed** SAX-label. This volume was computed with the *Arithmetic* module, where the arithmetic expression was defined as "output = abs(A-B)", resulting in a binary image that represents the quantitative difference between the 3D-WH and SAX labels. The respective volume values were calculated with the *MaterialStatistics* module, which returns the number of voxels in the binary "image" multiplied by the size of a single voxel. Besides, the areas of the 3D SAX-*innerLV* before and after transformation were also calculated and compared.

A.9 Alignment of TRA labeled images

After validating the previously described methodology to correct the misregistrations artifacts in the labeled SAX-stack, the steps A.7 and A.8 were repeated, but using the labeled TRA images instead of the SAX ones.

A.10 Labels Fusion

Considering that the 3D-WH, SAX and TRA sequences contain different anatomical information by differing in the orientation and also in the voxel size, it seemed useful to combine the information provided by each type of image. On one hand, the segmentation performed in the cine sequences is more reliable than the one from the 3D-WH, due to better in-plane resolution, 0.9 mm and 2mm, respectively. On the other hand, the high interval between the acquired 2D-SAX-images (7 mm) might result in the exclusion of the heart's apex or base (and consequently the valves). Thus, the goal of this step was to get a final stack of 2D-images, with an inner LV label obtained from the combination of the different segmented inner LV labels. Therefore, those were fused, by simply adding them and binarizing the result, with the *Arithmetic* module, which performs calculations on up to three input data objects according to a user-defined arithmetic expression. This expression was evaluated on the grid of the first data object, the stack of labeled 3D-WH images, since this was the stack with better out-of-plane resolution (higher number of slices).

A.11 Surface Extraction and Smoothing

The surface from the combined labels was extracted by the *SurfaceGen* module, which computes a triangular approximation of the interfaces between different material types in a LabelField, in this case the *innerLV* and the *Exterior*. It applies an algorithm developed at ZIB, the G*eneralize Marching* Cubes, which is an extension to the *Marching Cubes* Algorithm. The *Labelfield* is divided into an uniform grid and surface faces are calculated for every grid cell in the grid. The size of a grid cell is dependent on the resolution of the acquired images. This is called the triangulation of the grid cells. The grid cell has eight different corners that can be labeled as *innerLV* or *Exterior*. If all corners lie in the same region of the *Labelfield* no isosurface passes through that grid cell, but if one or more corners lie in different regions an isosurface intersects the grid cell, and it needs to be triangulated. The isosurface is complete when all grid cells have been triangulated. In order to circumvent staircase artifacts and remove sharp edges, a surface smoothing was mandatory. The *SurfaceGen* module allows the generation of a smoothed surface and the choice of how the smoothness is computed, namely:

a) *None:* no sub-voxel weights are used and the resulting surface will look staircase-like;
b) *Existing weights*: pre-computed weights are used. Such weights can be generated with the resample module or the smoothing filter in the image segmentation editor. A simple way to obtain weights is to use a smoothing filter on the labels, where every pixel is set to the maximum intensity where the current label occurs (*innerLV*) and zero otherwise (*Exterior*). Afterwards, all the images are blurred using a Gaussian filter, resulting in images containing pixels somewhere between the maximum and minimum intensity.

Finally, at every position in the grid, the weights of the different materials are set to the corresponding intensities found in the smoothed images.

c) C*onstrained smoothing* and *unconstrained smoothing* generate sub-voxel weights, such that the surface is naturally smooth. In the *constrained smoothing* mode a kernel of size 4 used and the module guarantees that no label is modified: any two voxel centers that have been labeled differently before the smoothing are separated by the generated surface afterwards. This is not necessarily the case for every small detail in the unconstrained case and in this case the kernel size is 5. The amount of smoothing can be controlled, by changing the variable *SmoothKernelSize*.

In order to compare the effect of the smoothing type on the LV volume and geometry, three surfaces were generated, one without smoothing and the two others with constrained and unconstrained smoothing. The triangulated surfaces can be visualized with the *SurfaceView* module, where many parameters, such as *color*, *draw style or shading*, can be controlled.

A.12 Surface Remeshing

This module implements the surface remeshing approach described *in* (Zilske et al. 2008). It is based on *Lloyd relaxation* and does not explicitly regularize the vertex connectivity. It attempts to generate a mesh with vertices placed isotropically across the surface in order to achieve a high triangle quality. Since vertex placement is modulated by either the curvature or by a density field, isotropy of vertex placement will only hold with respect to the modulated vertex distribution. The number of vertices and triangles in the final surface can be determined, and are dependent from each other, thus, setting one of the values will result in a modification of the other values. In regular surfaces, the number of triangles is twice as large as the number of vertices. The percentage of the original mesh size was set 100%, so that the number of triangles was maintained.

A.13 Surfaces Comparison

In order to evaluate the global impact of the applied methods for shape restoration on the reconstruction process, a qualitative and/or a quantitative comparison of the input and output data of the following methodological steps were performed:

- sequences' registration: visual inspection of the correspondence between the intensities of the images with different orientations;
- slices' translation: area and volume comparison of the original and transformed labels complemented with visual analysis
- fusion of the labels: the area and volumes of the 3D-WH and the SAX labeled images were compared to the ones of the fused labeled image.

In addition, steps A.10, 11 and 12 were applied to the original segmented SAX -, TRA and 3D-WH labels. Beside the visual comparison of the resulting geometries, the area and the volume involved by the resulting surfaces (extracted from the original segmented images) were compared with the ones from the corrected surface, so that the effect of the framework as a whole could be analyzed.

The module *SurfaceArea* computed the areas and the enclosed volumes of the *innerLV* surfaces in question. The volume computation simply sums the signed volumes of all of the tetrahedra joining surface triangles to the origin (point with coordinates x=0, y=0, z=0). The sign of the volumes depends on triangle orientation relative to the origin, so volumes are computed correctly even for non-convex surfaces. The result is the volume of the enclosed surface. The geometry was qualitatively evaluated by observing the extracted surfaces in the 3D-viewer from many different perspectives.

5.4.2 - Phase B: Inner LV Surface mesh generation in other cardiac phases

The goal of phase B was to reconstruct the 3D inner LV from images acquired in the remaining phases of the cardiac cycle, using the transformations applied to the correspondent images ED phase, in order to avoid the manual tasks of motion related corrections. First the LV surface in the end systolic (ES) phase was reconstructed, followed by the reconstruction in an intermediary phase between the ED and the ES. In each sequence, the ES images correspond to the images where the LV presents the smallest area, which in the evaluated patient was the 9^{th} scanned time point (9TP), identified by visual inspection of the blood-pool area. Thus, the images captured in 5^{th} time point (5TP) served as data for the reconstruction of the LV in an intermediary phase of the cardiac cycle. In order to achieve a better temporal resolution of the reconstructed spatio-temporal LV, the surfaces from 8 more phases of the cardiac cycle were generated. The variation of the eleven reconstructed shape objects in terms of area and volume shall represent the natural deformation of a beating heart.

Considering that the cine-sequences have a high temporal resolution (about 30 ms between each slice acquisition) and that it is performed on breath-holding mode, the in-plane translation of the slices acquired in the same heart position is minimal (the whole body is static during each slice scanning of about 10 s). Thus, the corrections computed for the images acquired during the ED phase could be applied to the ones acquired on the other cardiac phases. Only the methodological steps of phase B that differ from the ones of phase A will be described below, namely the *Sequences Registration*, the *Slices' Alignment* and the *Labels Fusion*.

B.1 Sequences Registration

In order to register the original 2CH, 3CH and 4CH images and the SAX- and TRA image stacks of the remaining cardiac phases, each of them suffered the 3D translation applied to the respective image/stack in the ED phase. Using the *TransformEditor* from each data object, it was possible to simply copy the transformation and paste it into the editor of the respective object to be transformed.

B.2 Slices' Alignment

The slices' alignment of the SAX-and TRA images in the remaining cardiac phases was also computed through the *AlignSlices* module, but this time without user interaction and without IPs. The module allows the connection to a reference 3D field, in this case the SAX or the TRA corrected images from the ED phase, from which the 2D-translation applied to each slice in the stack is read and transferred to the respective image in the field that must be transformed.

B.3 Labels' Fusion

Once again, the labels' fusion consisted on the stacks' addition and posterior binarization of the result. In order to obtain a final 3D inner LV label in the remaining cardiac phases with the same dimensions as the ones from the final label computed in the ED phase, this last was used as first input in the arithmetic operation for labels' fusion. Thus, the expression "output = SAX_label+TRA_label" was evaluated and returned on the grid of the first input data object, the stack of images that contained the final inner LV label in the ED phase. Finally, 3D smoothed surfaces with homogeneous meshes, representing the LV cavity in the remaining cardiac phases were obtained by applying the methods described in A.11 and A.12.

5.5 - Concluding Remarks

A strategy to reconstruct the anatomic surface of the inner LV from a patient with an aortic regurgitation by means of CMR images, acquired after a specific clinical protocol was presented. It combines the information provided from different types of MRI sequences and it is supposed to correct motion-related artifacts. The whole reconstruction process is conducted in the Amira software and it is more complex in the initial phase (ED), where a considerable user interaction is required. However, the transformations and processing used in the ED were adapted to the remaining cardiac phases, resulting in a simple and more automatic process to

extract the geometry of the inner LV of these phases. In sum the workflow consists on the following steps:

1. Manual sequences' registration based on pixels' intensities correspondence, to correct misregistrations among the different sequences.
2. Inner LV segmentation with the Amira's *SegmentationEditor* based on the intensities thresholds and *Region Growing* algorithm.
3. Contours extraction from LAX labeled images, representing the innerLV boundaries that will guide the following correction of motion-related artifacts.
4. Slices translations in the SAX and TRA labeled images, by interactively minimizing the distance of the inner LV label to the LAX contours.
5. Fusion of the SAX, TRA and 3D-WH inner LV labels to combine the information from the different types of images.
6. Surface extraction from the fused label, based on the *Marching Cubes* algorithm.
7. Surface smoothing, to remove sharp edges and staircase artifacts
8. Surface remeshing, based on *Lloyd relaxation* algorithm, to obtain a triangular mesh with high quality.

The results will be presented and discussed in the following chapters.

Chapter 6 - Results

In this section, the results obtained in each methodological step for the reconstruction of the inner LV in 11 phases of the cardiac cycle will be described, represented in figures, graphics or tables and briefly discussed. The dataset consisted on the following MRI sequences of an 8 years old child with an aortic regurgitation:

- the 3D-whole heart (3D-WH, 80 slices, voxel size in mm (VS): 1.42 x 1.42 x 2)
- the cine-short-axis (SAX, 14 slices, VS: 0.875 x 0.875 x 7),
- the cine-transversal (TRA, 30 slices, VS: 1 x 1 x 6),
- the cine-2 chambers (2CH: LV + LA, 1 slice, VS: 1.3 x 0 x 1.3),
- the cine-3 chambers (3CH: LV+LA+RA, 1 slice, VS: 1.3 x 1.3 x 0) and
- the cine-4 chambers (4CH: LV+LA+RV+RA; 1 slice, VS: 1.35 x 1.35 x 0).

All the presented figures consist on screenshots from the results' visualization in Amira.

6.1 - ED Phase

In this phase, the images scanned during the first acquisition time point (TP) from all cine-sequences and also the 3D-WH images were used to reconstruct the static inner left ventricle (LV) surface in the end diastolic (ED) cardiac phase.

6.1.1 - Sequences' Registration

The transformation applied to each of the long-axis (LAX) images, namely the 2CH, 3CH and 4CH images, consisted on manual 3D translations, so that the correspondence, in terms of gray level (GL), at the intersection lines from each of these images with the 3D-WH images was improved (Figure 6.1). The applied translation to each LAX image was also guided by the intersection line between each other (2CH with 3CH, 2CH with 4CH and 3CH with 4CH), where once again a better correspondence in terms of pixels intensities was sought (Figure 6.2). Thus, in the case of the 3CH image, the applied translation didn't improve the correspondence with the 3D-WH image (Figure 6.1 b)), but it improved the alignment with the 2CH and 4CH images (Figures 6.2 b) and c)). The misalignment of each image with the 3D-WH images and respective correction are illustrated in Figure 6.1, with the original images on the left and the translated images on the right, which present a higher correspondence with the 3D-WH image (in the transversal view-plane) in terms of pixel intensities. In Figure 6.2, the misalignment between the original LAX images and the respective correction can be detected by observing the intersection lines of the images with different orientations.

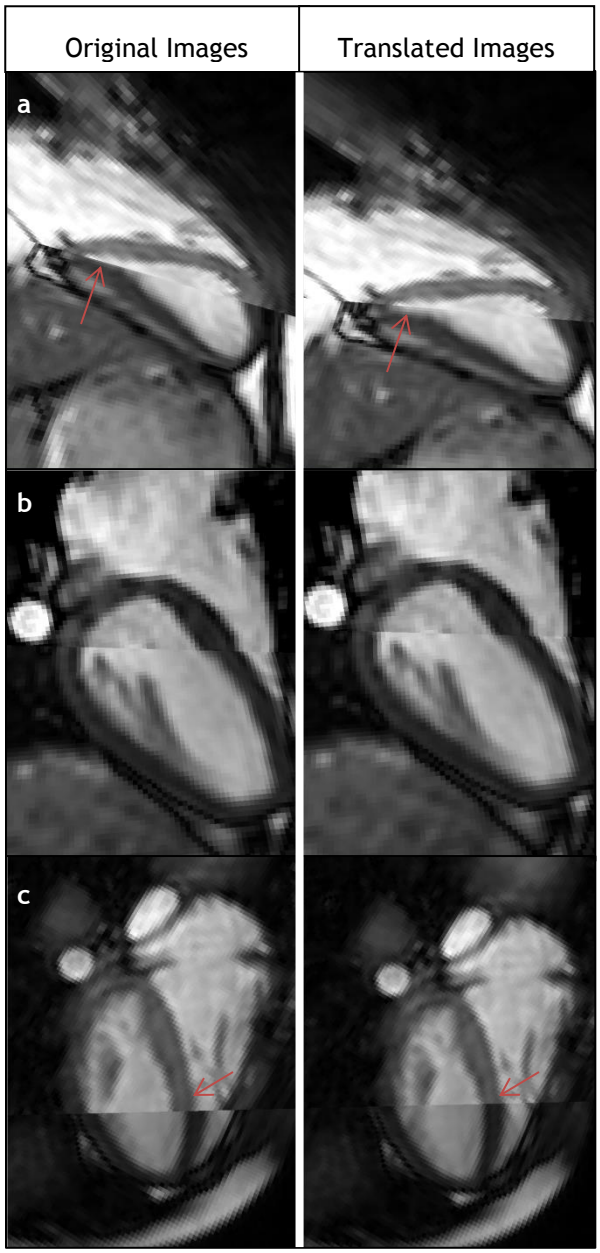

Figure 6.1 - Intersection of a 3D-WH image with a) 2CH, b) 3CH and c) 4CH images, before and after 3D translation of the LAX images. The arrows point to regions with misregistrations and the respective correction.

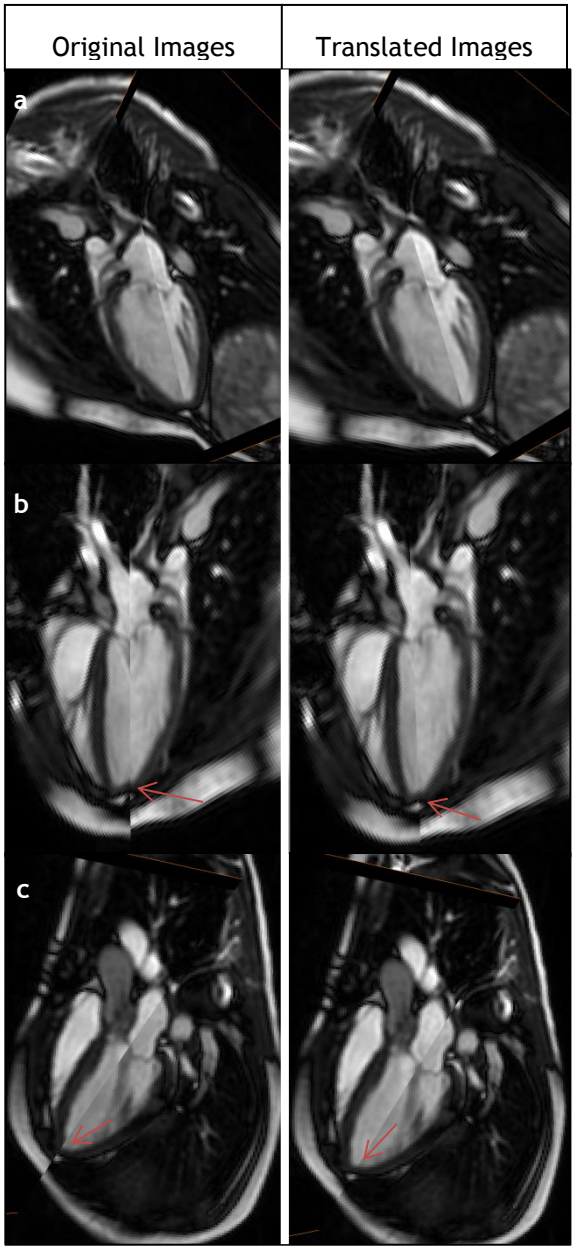

Figure 6.2 - Intersection of a) 2CH and 3CH, b) 2CH and 4CH and c) 3CH and 4CH images, before and after 3D translation of the images. The arrows point to regions with misregistrations and the respective correction

Table 6.1 presents the final translation values (in mm) in each direction regarding the respective local axis for the 2CH, 3CH and 4CH images, from where it is possible to conclude that the 4CH images required the a highest level of correction.

Table 6.1 – Final 3D translations (in mm) applied to the LAX sequences', for image registration between them and with the 3D-WH images.

	Translation's direction		
MRI sequence	**x**	**y**	**z**
2CH	-0,10	0,06	-3,16
3CH	0,51	-0,29	-0,76
4CH	1,94	4,49	-3,54

The origin of these misalignments lies on the uncontrollable patient's motion and on the non-exact repeatability of breath holding position during each sequence acquisition. Since the rigid body motion of the heart due to the respiration is mainly a translation in the cranio-caudal direction, while the rotation consists only on a couple of degrees (McLeish et al. 2002), the applied registration method compensates for 3D translational errors but not for rotation.

Analyzing the intersection lines between the translated LAX images with the SAX image stack and also the intersection lines between the 3D-WH images and the SAX stack, it was possible to conclude that this stack shouldn't suffer any kind of 3D translations, first, because the slices position in respect to the local z-axis was in agreement with the other types of image and second, because the in-plane position of each slice in the stack could be incorrect due to the scanning during different breath-holds. Nevertheless, the need to correct these sequences' position changes from patient to patient, depending on their motion during image acquisition. The same situation was observed in the case of the TRA images.

6.1.2 - Inner LV Segmentation

For each type of MRI image, the inner LV label obtained from the blood-pool segmentation is represented in Figure 6.3, where the original image is "colorwashed" in purple with the segmented region. In the cases of 3D-WH, SAX and TRA, one representative slice from each 3D stack is shown. It is possible to observe the inclusion of the papillary muscles when totally imbedded in the blood-pool, and their exclusion when connected with the LV wall (Figure 6.3 b).

The segmentation was more challenging in the 3D-WH images, which present a lower in-plane resolution. In the apical slices of this type of images and also of the SAX images, the inner LV contour was more difficult to identify. The GL from each voxel in a slice is computed from the average of the emitted signals by all the hydrogen atoms contained in the respective organ volume, which in the

apical slices might include the wall muscle and blood, leading to a weaker emitted signal and consequently a lower GL value and blurred contours.

Another challenge associated to the segmentation task, was the identification of the LV barriers with the left atrium (LA) and with the aorta in the images where the respective valves were not clearly represented. In these cases, the segmentation was guided by the basal limits of the surrounding LV wall, where the valves are inserted (Figure 6.3 a). Since no segmentation ground-truth was available, the obtained results had to be evaluated qualitatively by an expert in the field of cardiac segmentation, who classified them as accurate. In case of wrongly segmented regions, such as the inclusion of valves in the blood-pool region, the necessary corrections detected by the expert were applied.

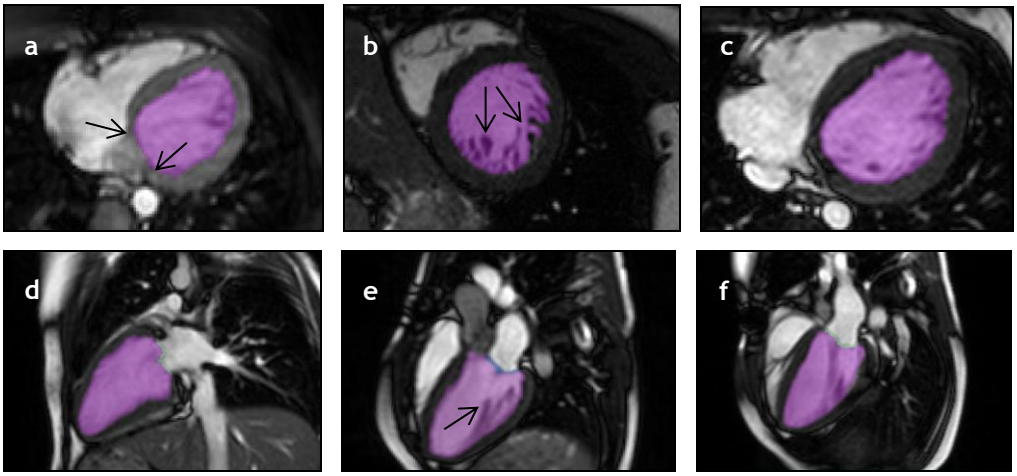

Figure 6.3 – Segmentation results. The original images are overlaid with the respective segmented inner LV region in purple. a), b) and c) are representative slices of the 3D-WH, SAX and TRA stacks, respectively. In d) 2CH, e) 3CH and f) 4CH the mitral valve was also segmented, which is visible in green; the arrows in a) point to the LV wall extremities, that were used to define the upper limits of the inner LV region when the valves were not identifiable; the arrows in b) and e) point out the included and excluded papillary muscles or trabeculations.

6.1.3 - Alignment of labeled SAX slices

The contours extracted from the labeled 2CH, 3CH and 4CH images are illustrated in Figure 6.4 and their intersections with the stack of SAX labeled images are represented in Figure 6.5, and in Figure 6.6 by means of the computed intersection points (IPs). In these last two figures, it is possible to observe that the long axis (LAX) contours don't intersect the boundary of the inner LV label in all slices of an image stack, which demonstrates the presence of motion related artifacts in some slices.

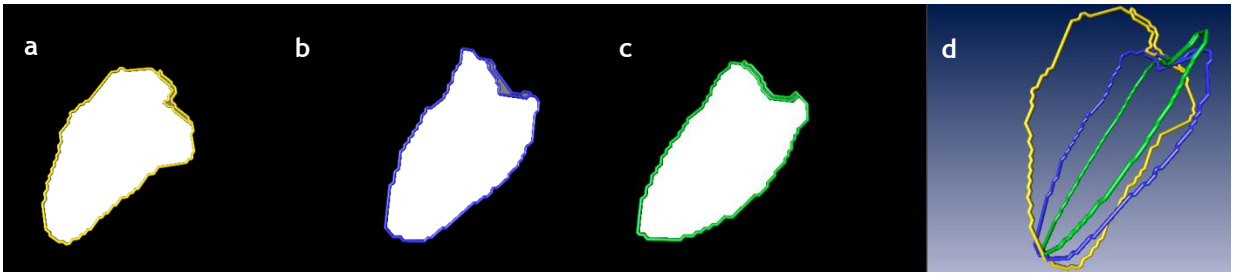

Figure 6.4 – Extracted contours overlaid on the respective inner LV label, a) 2CH, b) 3CH and c) 4CH. d) 3D visualization of the extracted contours.

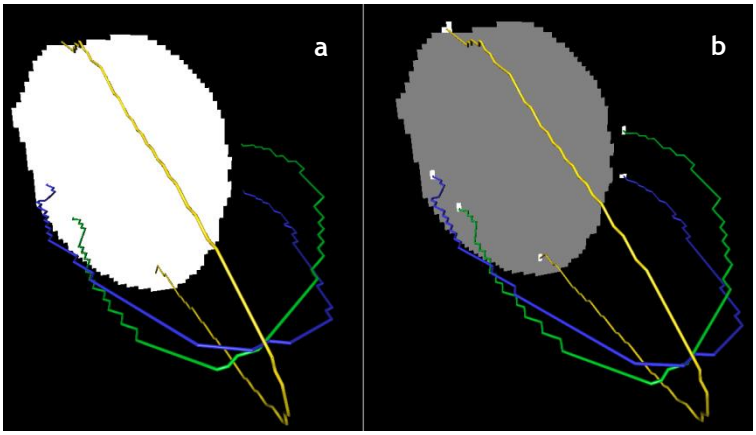

Figure 6.5 – a) Intersection of each long-axis (LAX) contour with a labeled short-axis (SAX) image. b) LAX contours with the correspondent intersection points (IPs) with the labeled SAX image (gray) in question represented as white dots.

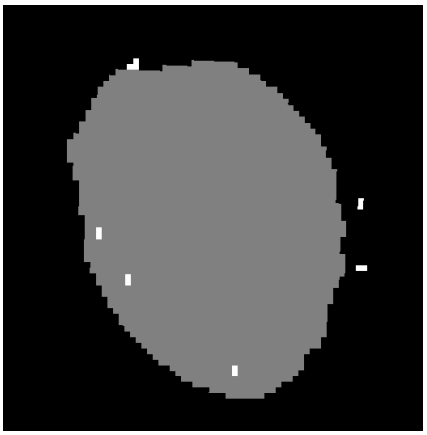

Figure 6.6 – Inner LV SAX label (gray) and respective IPs (white), that will guide the 2D translation of this SAX slice, in order to correct motion-related artifacts.

The result of attempting a better match between the *innerLV* and the contours can be observed in Figure 6.7 by two representative slices, where the gray region represents the original label and the purple one represents the corrected label with an overall lower distance to the IPs (white).

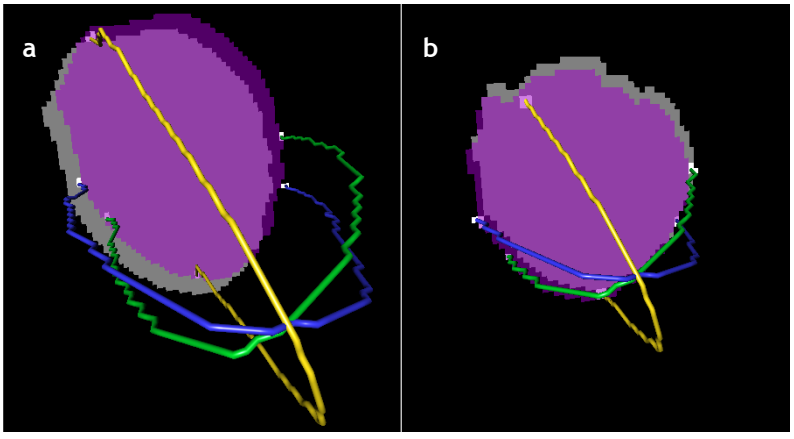

Figure 6.7 – Visualization of the SAX slices' alignment. The gray region represents the inner LV label in its original position and the purple region represents the 2D-translated one; a) slice 3 and b) slice 8 of the SAX stack.

It was not possible to obtain a perfect match of the *innerLV* in each slice with all the correspondent IPs, probably due to a slight imprecision in the segmentation step, especially in the presence of the valves, which GL values are similar to the ones of the blood-pool. Nevertheless, for each slice, the overall correspondence was improved. The correction of the in-plane position is also visible in Figure 6.8, where the original and corrected labels are presented from different view-planes in order to demonstrate the better alignment between the consecutive slices.

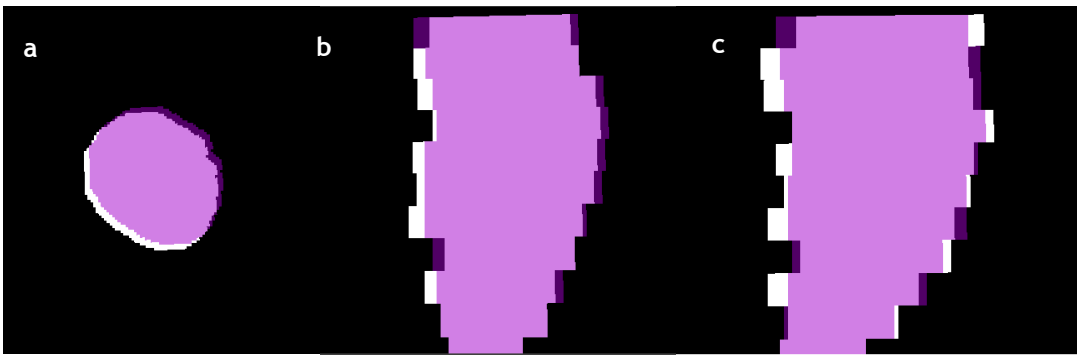

Figure 6.8 - Visualization of SAX slices' alignment from different local view-planes: a) xy b) xz and c) yz planes. The white region represents the inner LV label in its original position and the purple region represents the 2D-translated one.

The illustrations in Figures 6.7 and 6.8 demonstrate the fact that the misregistration artifacts can be different for each slice of a dynamic MRI sequence, due to the non-exact repeatability of breath-holding during the scanning of each slice. Thus, the registration process between different types of cine-sequences cannot be computed by transforming the whole stacks, but instead, it is necessary to correct the displacement of each slice in the stack individually.

Similar results were obtained for the alignment of the TRA labeled slices, which can be observed in Figure 6.9.

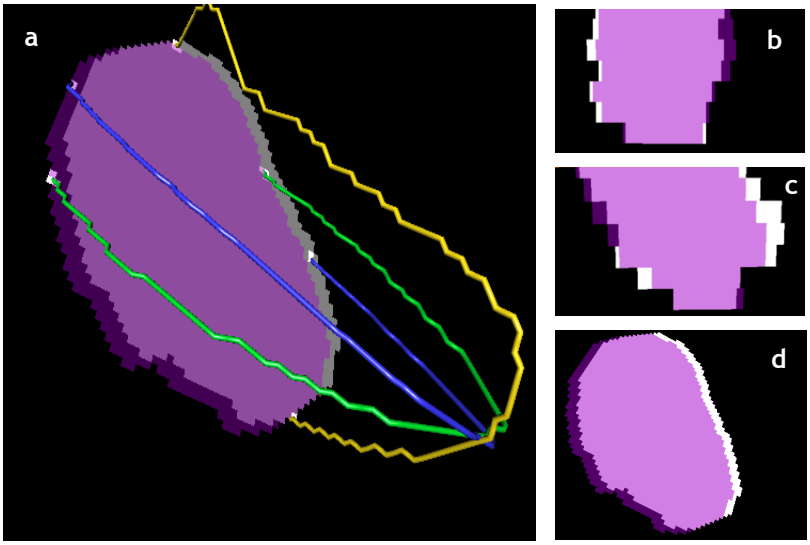

Figure 6.9 - Alignment of the labeled TRA slices: a) Intersection with the contours extracted from the 2CH, 3CH and 4CH inner LV labels and respective IPs, which were used to guide the 2D translation of each slice. Visualization from different local view-planes: b) yz c) xy and d) xz planes. The gray and white regions represent the inner LV label in its original position and the purple region represents the 2D-translated one.

In order to quantitatively evaluate the slices' alignment from the SAX and TRA labeled stacks, the volume difference between the inner LV labels and the 3D-WH label was compared to the ones between the respective corrected labels and the 3D-WH label. The resulted values for these volumes are given in Table 6.2. In both cases, the slices' alignment led to a better correspondence with the 3D-WH labels, which can be deduced from the reduction of the volume difference.

Table 6.2 – Inner LV volume difference of the original and aligned labeled slices in relation to the 3D-WH label in the ED phase.

	SAX		**TRA**	
	Original	Aligned	Original	Aligned
Volume Difference (cm^3)	20,74	14,45	36,98	33,13
Volume Diff. Reduction (%)	30,3		10,4	

The reduction of the volume difference between the labels before and after alignment is also presented, in terms of percentage. This was more significant in the case of the SAX images, because the respective stack contains almost twice the number of labeled slices (12), covering the whole heart, than the TRA stack of labeled images (7), which only covers the upper half of the heart. Thus, the higher percentage of volume difference reduction is not necessarily related to a better alignment, but probably to the higher amount of corrected slices.

6.1.4 - Labels' Fusion and Surface Extraction

The fusion of the corrected 3D inner LV labels computed from the 3D-WH, SAX and TRA images resulted on a stack of binary images with the same dimensions as the 3D-WH stack. This 3D image presents the inner LV region computed with the information provided by all types of acquired images, namely:

- the 2CH, 3CH and 4CH, which were used to correct motion-related artifacts and
- the 3D-WH, SAX and TRA, that allowed the extraction of the inner LV region from different positions and planes.

The surface of the fused *innerLV* was first extracted without any type of smoothing and it is represented in Figure 6.10. It is possible to recognize a high level of irregularity and roughness on surface, mainly due to the different voxel size (see page 62) and different orientation of the joined labels, but also because of the large slice thickness in the SAX and TRA stacks, which lead to the staircase effect.

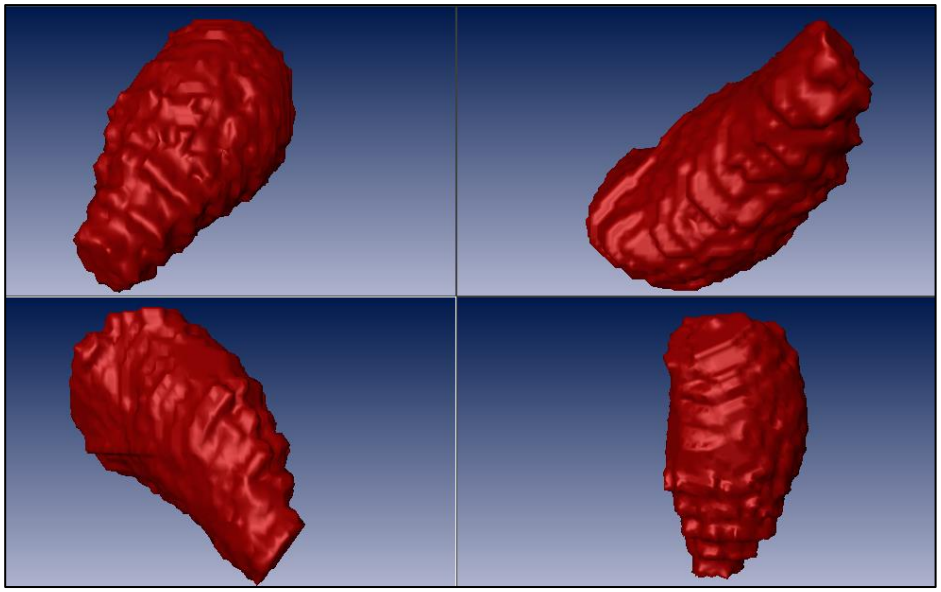

Figure 6.10 – Inner LV surface extracted from the fused 3D-WH, SAX and TRA labels, presented from different perspectives.

Thus, in the attempt to obtain an homogeneous shape of the inner LV, two more surfaces were generated, applying a constrained and an unconstrained smoothing, with kernel sizes of 4 and 5, respectively (see section 5.4.1, phase A.11, pages 57/58). In Figure 6.11 the effects of each smoothing type can be observed, from where it is possible to conclude that the constrained method leads to a slightly smoother surface but with no significant difference when compared to the unsmoothed one, in contrast to the unconstrained smoothing, which allowed the removal of the small details (saliences) and at the same time preserved the overall inner LV shape (Figure 6.12).

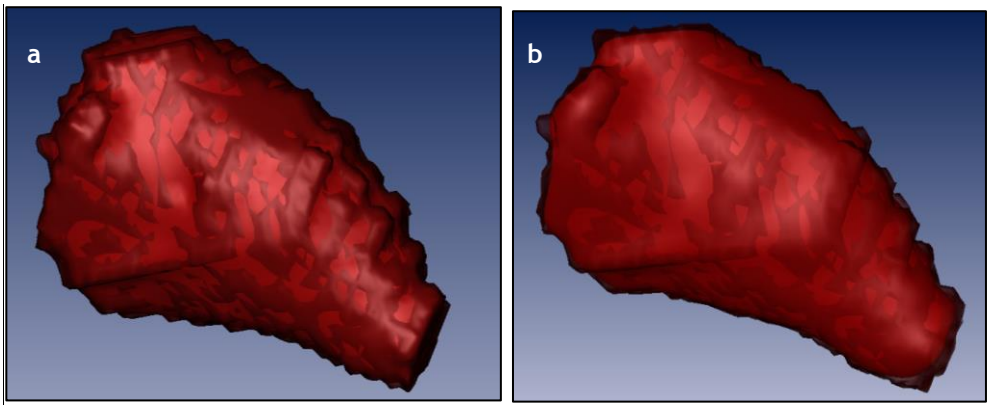

Figure 6.11 – Comparison of original (transparent) and smoothed (shaded) surfaces. The shaded surfaces in a) underwent a constrained smoothing process and in b) an unconstrained smoothing process.

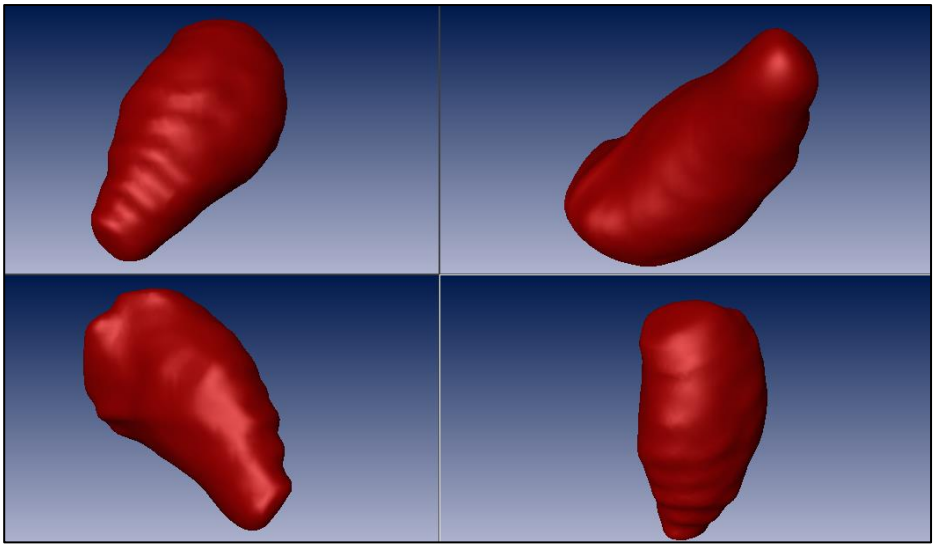

Figure 6.12 – Different perspectives from the inner LV surface extracted from the fused 3D-WH, SAX and TRA labels and smoothed (unconstrained smoothing) with the Amira's *SurfaceGen* module.

The volumes and surfaces of each smoothing type are given in Table 6.3. The reduction of the surface area from the original surface to the unconstrained smoothed surface (16% less) is higher than to the constrained one (11%), and the volume variation in both cases is not significant (less than 3%). This quantitative results support the conclusion extracted from the visual inspection, i.e. the unconstrained smoothing returns more satisfactory results than the constrained one.

Table 6.3 - Effect of different smoothing types on the surface area and respective enclosed volume

Smoothing	Volume (cm^3)	Area (cm^2)
None	95,3	130
Constrained	93,4	116
Unconstrained	92,4	111

For the visualization of the smoothing effect, a cut-plane in each local orientation (axial, sagittal and coronal) of the 3D fused inner LV label and the respective unconstrainedly smoothed surface are presented simultaneously in Figure 6.13. The transparent smoothed surface covers almost the whole area of the labeled images, leaving out only the sharp edges.

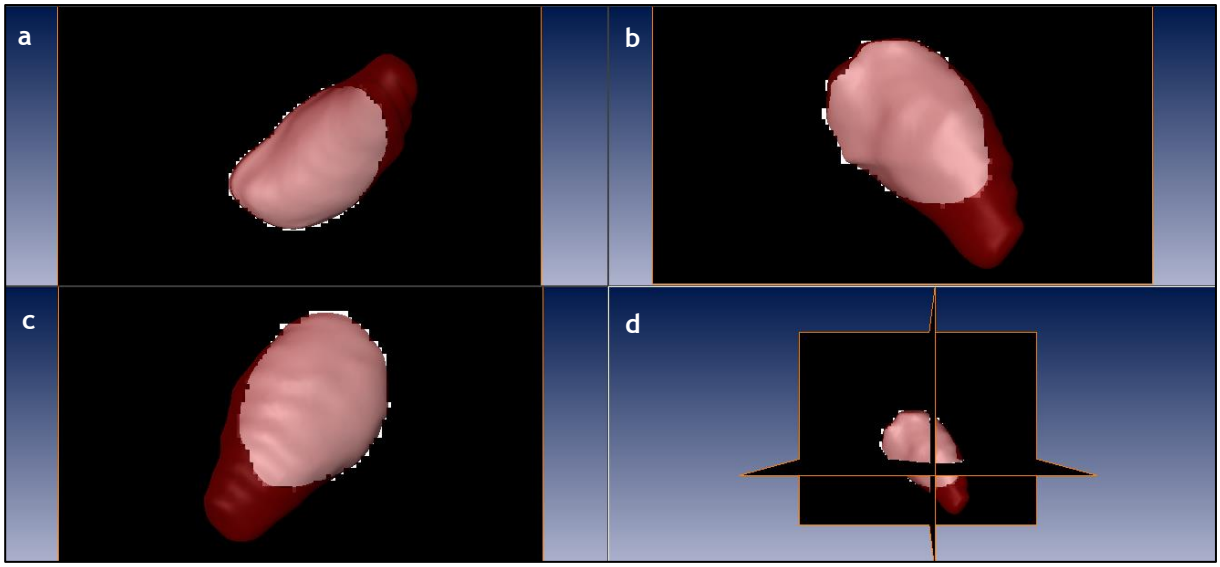

Figure 6.13 – Unconstrained smoothed inner LV surface extracted from the fused 3D-WH, SAX and TRA labels, and respective cutting-planes in different orientations: a) axial, b) coronal, c) sagittal and d) simultaneous visualization of the three cutting-planes and the inner LV surface.

To evaluate the effect of inner LV labels fusion, the area and volumes enclosed by the smoothed surfaces extracted from each label field (3D-WH, SAX and TRA) after slices' alignment and from the fusion of all of them were calculated and are presented in the Table 6.4. Since the TRA scan captured only half of the LV region, the respective volume is much smaller than the remaining ones. In regard to the fused labels, it is possible to conclude that the respective volume is larger than the one from the SAX and 3D-WH inner LV labels (12,8% and 15,5 %, respectively). A similar, but less intensive effect can be observed in regard to the area. Taking into account that the sequences are aligned between each other (the cine sequences were transformed with the support from the LAX images, that in turn were registered with the 3D-WH stack), these volume and area increases are not associated to misaligned slices, but instead, it might be interpreted as a complementation among the different labels for the definition of the inner LV boundaries.

Table 6.4 – Volumes and Areas from smooth surfaces extracted from the individual inner LV labels and from the fused one

	3D-WH	SAX	TRA	Fusion
Area (cm^2)	100	101	79	111
Volume (cm^3)	78,1	80,6	55,7	92,4
% of "Fusion" Volume	84,5	87,2	60,2	-

The triangulated mesh of the final surface can be visualized by setting the *drawstyle* parameter of the *SurfaceView* module to "outlined", resulting in an opaque shaded display with the triangle edges superimposed. The surface mesh is given in Figure 6.14, where it is possible to observe the anisotropic size and distribution of the respective triangles.

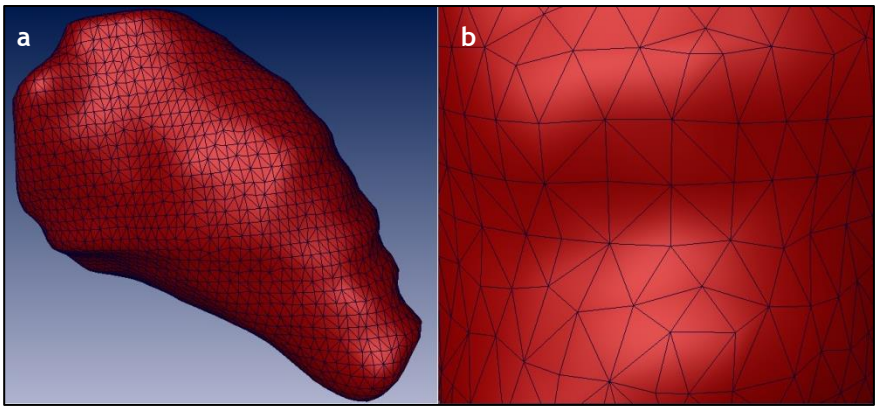

Figure 6.14 - a) Inner LV surface mesh. b) Zoom-in of the mesh, highlighting the triangles anisotropy.

Considering the posterior cardiac simulations, it is important to achieve a higher mesh quality on the surface, represented by a higher level of surface mesh homogeneity. Thus, a surface remeshing considering the best isotropic vertex placement across the surface was computed. The mesh improvement in terms of elements' isotropy and overall homogeneity is clearly shown in Figure 6.15.

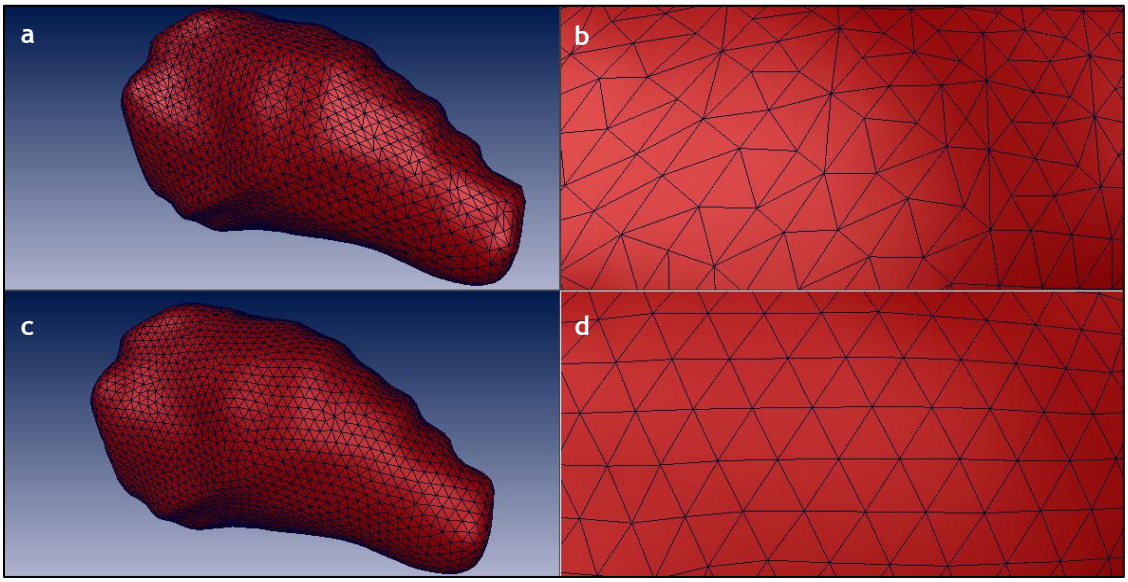

Figure 6.15 - Surface remeshing : a) original inner LV surface mesh, b) zoom-in of the surface mesh, c) remeshed surface and d) zoom-in of the remeshed surface

6.2 - ES Phase

The transformations transferred from the 2CH, 3CH and 4CH images in the ED phase to the ones in the end diastolic (ES) phase resulted in most cases on a better, although not perfect, correspondence in terms of intensity values in the intersection lines of the images. This result can be observed in Figure 6.16, where the intersections of the 2CH, 3CH and 4CH images, before and after 3D translations, are presented.

The result of the inner LV segmentation of the original SAX-images in the ES phase is shown in Figure 6.17 with a representative slice "colorwashed" with the respective segmented region and also by the respective label surface. The equivalent results for the TRA images can be observed in Figure 6.18. Due to the LV maximum state of contraction, the absence of the rounded shape previously observed in the ED phase, is evident in both cases, especially in the SAX label that covers the whole inner LV region. Besides, due to the thickening and contraction of the LV wall, the distance between apex and base decreases rapidly and the ventricles shorten by approximately 7 mm (Baillargeon et al. 2014), which was confirmed with the SAX segmentation's result that consisted in a lower amount of slices (8) where the blood pool of the LV was present.

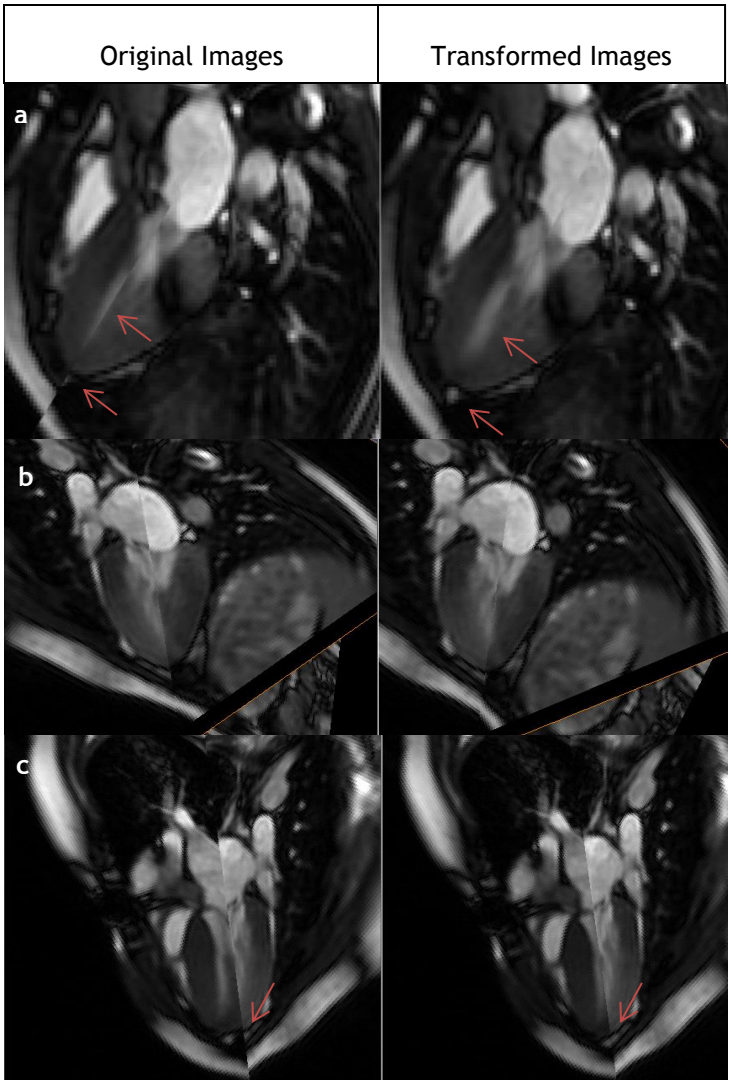

Figure 6.16 - Intersection of a) 4CH and 3CH, b) 2CH and 3CH and c) 2CH and 4CH images of the ES phase, before and after 3D translation of the images. The arrows point to regions with strong misregistrations and the respective correction.

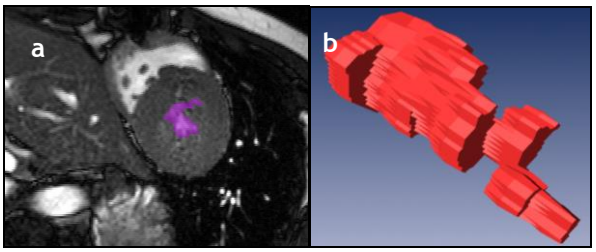

Figure 6.17 - SAX segmentation results for the ES phase. The representative original image is overlaid with the respective segmented inner LV region in purple (a). The inner LV surface generated from the label field is represented in b).

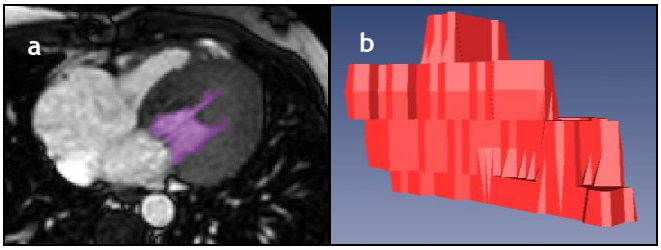

Figure 6.18 - TRA segmentation results for the ES phase. The representative original image is overlaid with the respective segmented inner LV region in purple (a). The inner LV surface generated from the label field is represented in b).

The alignment of the SAX and TRA labeled slices in the ES phase was performed by transferring the 2D-translation applied to each slice of the ED phase to the respective slice in the ES phase. The results are given in Figure 6.19 and in Figure 6.20 by means of the original and corrected surfaces representation.

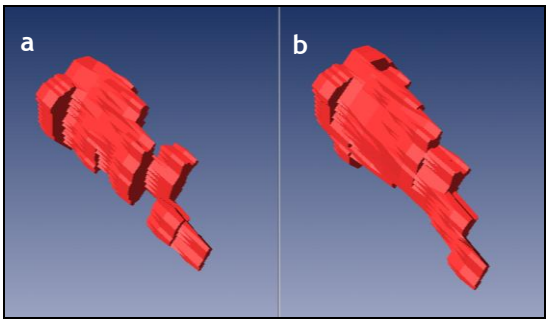

Figure 6.19 - Comparison of the inner LV surface generated from the SAX label field before (a) and after (b) slices' alignment.

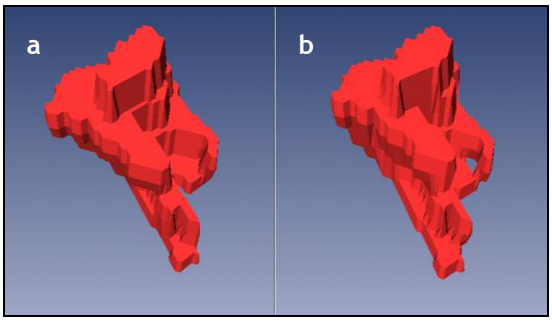

Figure 6.20 - Comparison of the inner LV surface generated from the TRA label field before (a) and after (b) slices' alignment.

In order to evaluate the transferred translations, the intersection between the original 3D labeled images and the original LAX images were compared with the intersection between the LAX images and the corrected 3D labeled images. Therefore, each LAX image was separately "colorwashed" with the original and with the corrected labeled SAX and TRA images. Figure 6.21 corresponds to the SAX images and Figure 6.22 to the TRA ones.

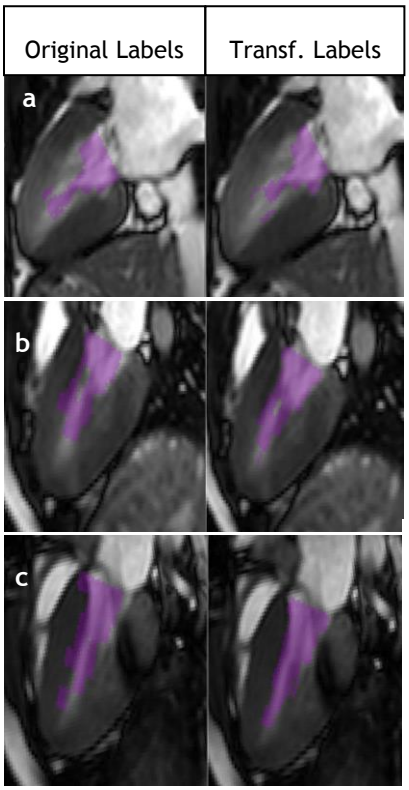

Figure 6.21 Original and transformed SAX innerLV label (purple) overlaid on the a) 2CH, b) 3CH and c) 4CH images.

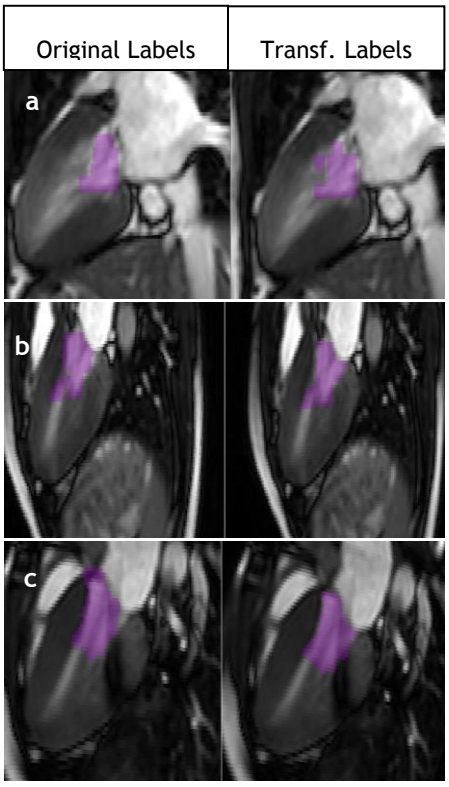

Figure 6.22 Original and transformed TRA inner LV label (purple) overlaid on the a) 2CH, b) 3CH and c) 4CH images.

It is possible to observe in all cases that the corrected labeled images present a higher level of correspondence between their blood-pools and the LAX images than the original labeled images, validating the method for slices' alignment in the different stacks of images. This result was expected, since for each slice position, the scanning is performed during a single breath-hold with a good temporal resolution, during which no patient motion is expected, resulting in similar slices' position of each acquired cardiac phase.

The inner LV regions extracted from the SAX and TRA images were combined with the inner LV region obtained in the ED phase to reconstruct the final surface in the ES phase, which is presented from different perspectives in Figure 6.23. The shrinked and irregular shape associated to LV contraction is clearly present, which will affect the respective surface mesh homogeneity and consequently require a remeshing process. The surface's discretization and posterior remeshing results are given in Figure 6.24, where the reduction of the triangles' anisotropy, especially in embossing regions, can be observed.

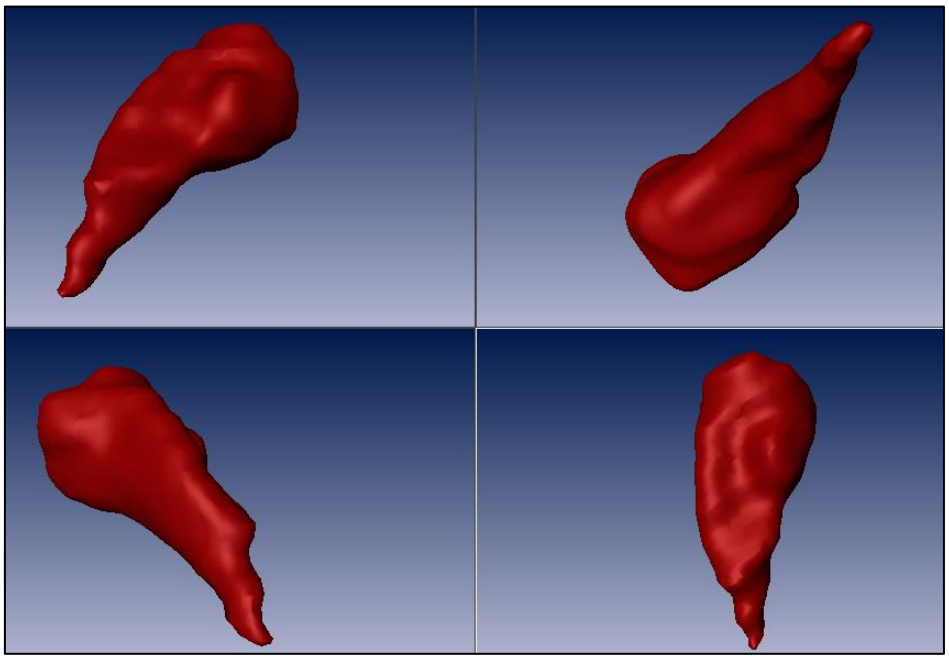

Figure 6.23 - Smoothed inner LV surface extracted from the fused SAX and TRA labels in the ES phase, presented from different perspectives.

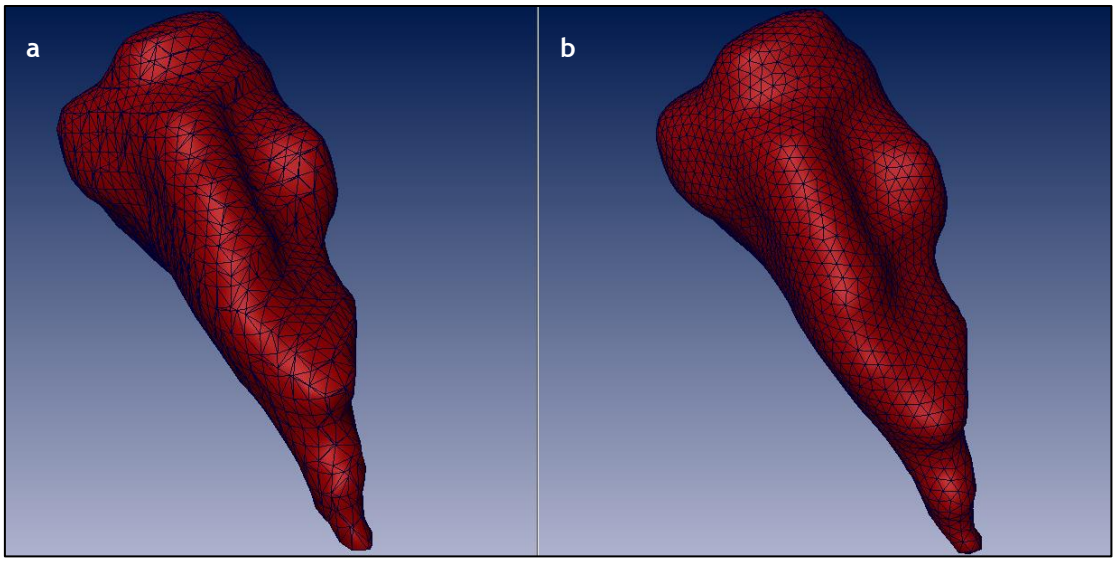

Figure 6.24 – Surface remeshing: a) original inner LV surface mesh and b) remeshed surface in the ES phase.

6.3 - Intermediary Cardiac Phase

Taking into account that the framework to reconstruct the inner LV surface in the ES phase generated good results, the same methods were applied for the same reconstruction in an intermediary phase of the cardiac cycle (TP5). In Appendix A the results obtained for each reconstruction step of the intermediary phase can be consulted, whereas the final inner LV surface can be observed from different perspectives in Figure 6.25 and the respective mesh, before and after remeshing, in Figure 6.26.

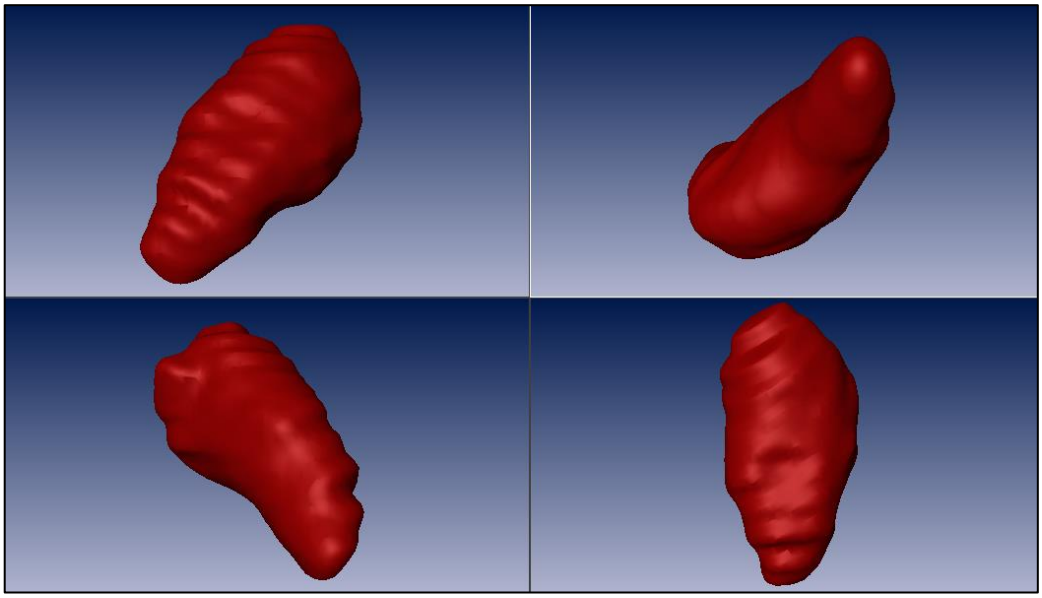

Figure 6.25 - Smoothed inner LV surface extracted from the fused SAX and TRA labels in the intermediary phase, presented from different perspectives.

Once again, the translations transferred from the ED, lead to a higher level of correspondence between the blood pool region of the different types of image and in smoother SAX and TRA surfaces. As final result, a more accurate 3D representation of the heart's anatomy in the intermediary phase between the ED and the ES was achieved.

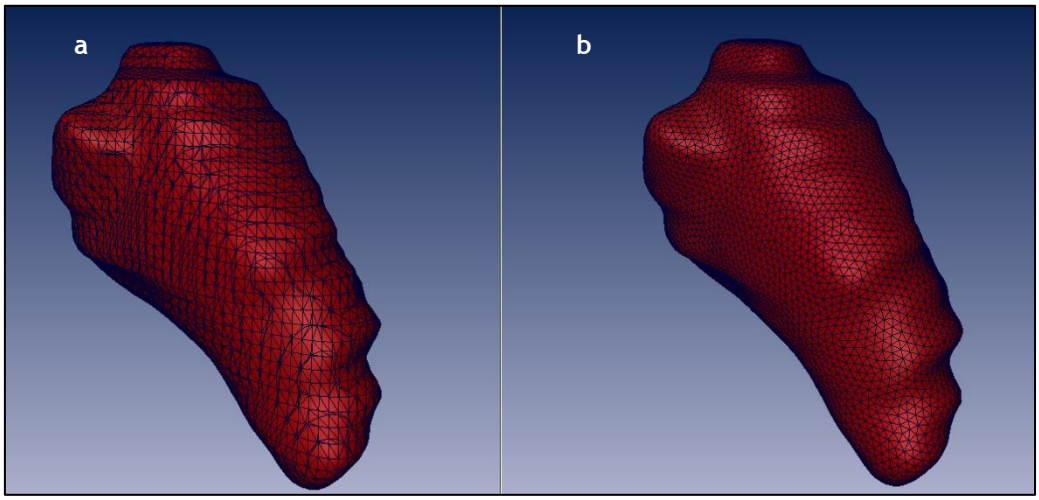

Figure 6.27 –Surface remeshing: a) original inner LV surface mesh and b) remeshed surface in the intermediary phase (TP5).

In order to quantitatively analyze the effect of each technique on the reconstructed surfaces, the area and volume values obtained from the reconstructed surfaces for each type of sequence (3D-WH, SAX and TRA) and the respective fusion, before and after all type of translations, for the three reconstructed cardiac phases (ED, TP5 and ES) are given in Table 6.6. For comparison purposes, Table 6.7 presents the mean values for ED and ES volumes calculated for a group of patients with a valve disease reported by (Taniguchi et al. 2007).

Table 6.6 - Calculated volumes and areas of the generated surfaces in the different phases of the framework for the reconstruction of the inner LV surface from an 8 years old patient with an aortic valve disease. The volume is given in cm^3 and the area in cm^2. (Orig.=Original images, Transl.= translated images)

	End Diastolic Phase				Intermediary Phase				End Systolic Phase			
	Volume (cm^3)		Area (cm^2)		Volume (cm^3)		Area (cm^2)		Volume (cm^3)		Area (cm^2)	
Sequence	**Orig.**	**Transl.**	**Orig.**	**Transl.**	**Orig.**	**Transl.**	**Orig.**	**Transl.**	**Orig.**	**Transl.**	**Orig.**	**Transl.**
3D_WH	78,1	-	100	-	-	-	-	-	-	-	-	-
SAX	78,9	80,6	102	101	49,8	45,4	76	72	9,7	4,0	45	18
TRA	54,8	55,7	79	79	30,2	30,3	53	54	7,6	6,5	33	20
"Fusion"	98,0	95,3	138	130	71,7	70,7	124	120	19,5	19,2	61	59
"Fusion" smoothed	95,4	**92,4**	113	**111**	63,7	**67,9**	90	**93**	13,9	**16,8**	36	**39**

Table 6.7 - Data adapted from (Taniguchi et al. 2007) for a group of patients with aortic regurgitation and for a control group.The end-diastolic (EDV) and the end-systolic volumes (ESV) were calculated by multiplying the population's mean body mass with the EDV Index and with the ESV Index, respectively. The pathology in cause has as consequence a much higher EDV and ESV than in "normal" cases.

Patient's data	**Taniguchi et al. 2007**	
Disease	Aortic Regurgitation	None
Nr of Patients	82	30
Mean Age (years)	48 ±14	43 ±11
EDV (ml)	335 ± 104	130 ±16
ESV (ml)	178 ± 90	45 ±10

The following ascertainments can be extracted from Table 6.6:

1. Quantitatively, the 2D translation applied to the images of the SAX and TRA sequences has no significant impact on the area and on the volume enclosed by the respective surfaces. Nevertheless, the visual inspection allowed to conclude that the geometry of the corrected LV surface improved.
2. In the three phases and before smoothing, the area and volume of the surface extracted from the fused translated images is lower than from the fused original ones, confirming that the 2D translations (i.e. the applied in-plane slices' shifts) lead to a better match between the labels of the different sequences.
3. The fusion of the labels increased the volume and the area in all cases (when compared to the individual labels), but especially in the ES phase, which can be interpreted as a complementation of information regarding the LV region.
4. The smoothing of the surfaces, reduced the volume and areas of all surfaces extracted from the fused labels, but more significantly in the original ones, suggesting a higher level of irregularity in the surfaces extracted from the original labels than from the corrected ones.
5. The surfaces' volume and area decreased from the ED phase until the ES phase, as expected, since during this period the LV myocardium is contracting, ejecting the blood out of the ventricular cavity.
6. The left-ventricle ejection fraction (LVEF) of the patient in case is 88%, when calculated from the original SAX labels (standard clinical procedure), and 81%, when calculated from the volumes enclosed by the final reconstructed surfaces (translated and fused).
7. The volume values found in the literature for patients with valvular disease are relative different from the ones obtained in this project, due to the age difference in the studies' populations.

6.4 - Remaining Cardiac Phases

The qualitative (or visual) results obtained in the ES and intermediary phases inspired confidence on the developed reconstruction methodology, despite the reduced quantitative impact in terms of areas and volumes values. Thus, the surfaces in 8 other phases of the cardiac cycle were reconstructed with the same strategy. Table 6.8 presents the area and volume of the final reconstructed LV cavity in 11 eleven phases of the cardiac cycle. The respective volume values were calculated with the *MaterialStatistics* module, which returns the number of voxels in the binary "image" multiplied by the size of a single voxel. The total sum of the triangles' area on the region's boundary return the surface's area.

Table 6.8 - Volume and area extracted from the surfaces generated in different phases of one cardiac cycle.

Cardiac Phase	1	3	5	7	9	12	15	18	20	22	25
LV Volume (cm^3)	92,4	91,7	67,9	39,2	16,8	24,6	72,3	83,5	90,5	92,3	112,9
LV Area (cm^2)	111	111	93	68	40	50	96	107	110	111	127

In order to visualize the area and volume variation during a cardiac cycle, the respective values were plotted in two graphs, depicted in Figures 6.28, where the surface reconstructed in each cardiac phase can also be visualized by a small icon. A plot showing the results obtained by (Long et al. 2008) for the LV volume variation is given in Figure 6.29. The Wiggers Diagram (Richardson, 1998), introduced in Chapter 2, was adapted so that the variation of the LV volume during one cardiac cycle became highlighted (Figure 6.30). Comparing the obtained results with the ones in the literature, it is possible to observe the same variation profile of the LV volume, which corresponds to the natural deformation of a beating heart: During the systole, which in this case correspond to the first 9 scanned frames, the ventricular volume decreases rapidly, followed by a slower blood-filling, corresponding to the diastole.

The rate of LV volume variation for the computed time points during one cardiac cycle can be observed in Figure 6.31. The graphic shows the numeric results, and the geometric results are once again represented by small icons following the graphic evolution. Each surface represents the reconstructed surface in one specific frame and the distance to the reconstructed surface in the following frame, encoded in a color range: high distance values between surfaces are represented in red, whereas low distances are represented in white. Thereby, the regions of the surface that deform at most between two cardiac phases can be detected. The surface icon in the dashed rectangle shows the shape of the surface reconstructed from the 7th frame and the intense red areas indicate the regions where the distance to the surface reconstructed in the 9th time point is higher. The volume variation

rate between this two time points is indicated in the bar at frame 9 (around 11%). High negative values of volume variation rate can be interpreted as an intensive contraction of the left ventricle, which is the case between the time points 7 and 9, whereas a rapid blood filling due to the relaxation of the LV can be detected between the time points 12 and 15, where the volume variation rate is high and positive (around 15%). This deformation analysis can be complemented with the "distance" surfaces, which indicate the regions where the LV deforms the most. Thus, the reconstructed surfaces can be used to conduct a primary analysis of the LV deformation and blood-flow, parameters that are necessary to conduct cardiac functional analysis and biomechanical studies.

The integrated interpretation of the results can be found in the next chapter, where the developed workflow is discussed.

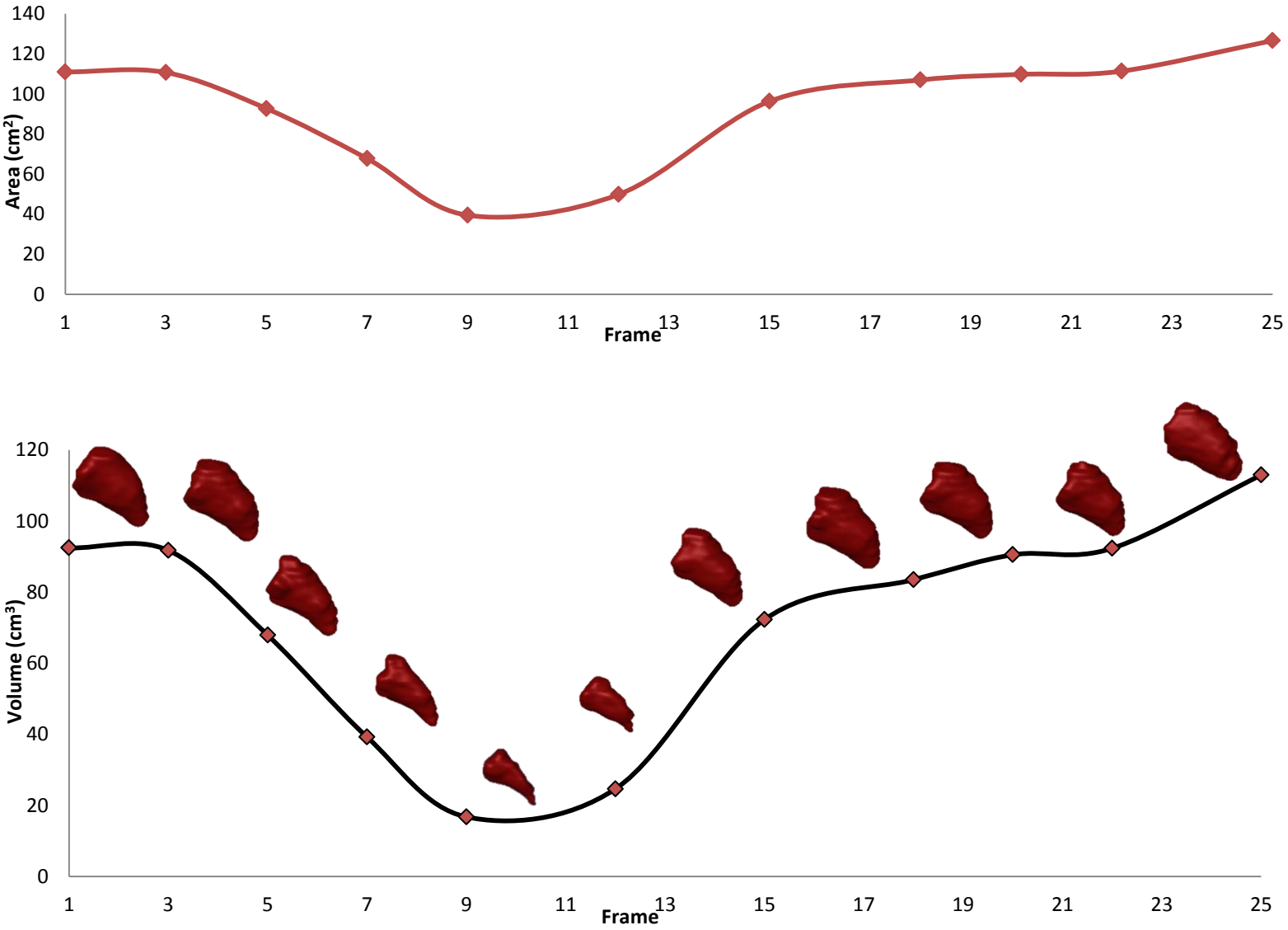

Figure 6.28 - Variation in the LV area (up) and volume (down) in one cardiac cycle extracted from the reconstructed surfaces. The small icons represent the extracted surface in each cardiac phase.

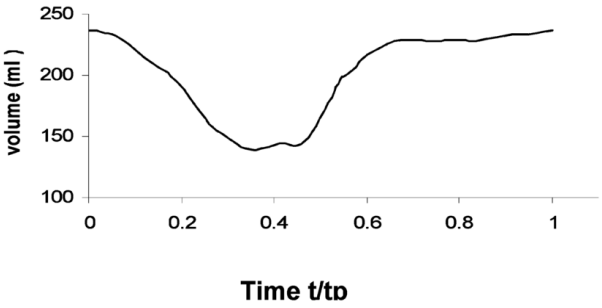

Figure 6.29 - Variation in the LV volume in one cardiac cycle for a normal subject, from (Long et al. 2008).

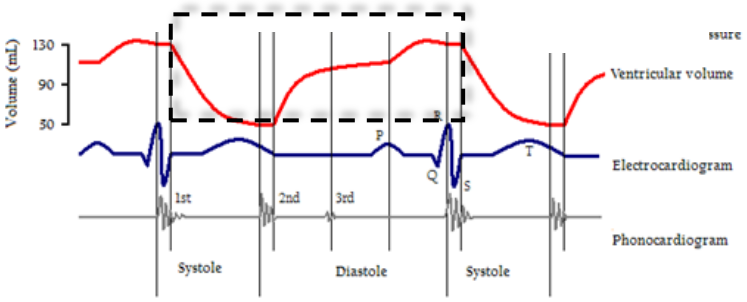

Figure 6.30 – Wiggers Diagram [Richardson 1998] - It shows the ventricular volume and the ECG of the cardiac function during a cardiac cycle (adapted from http://en.wikipedia.org/wiki/Cardiac_cycle).
The window highlights one cardiac cycle from the beginning of systole until the late diastole.

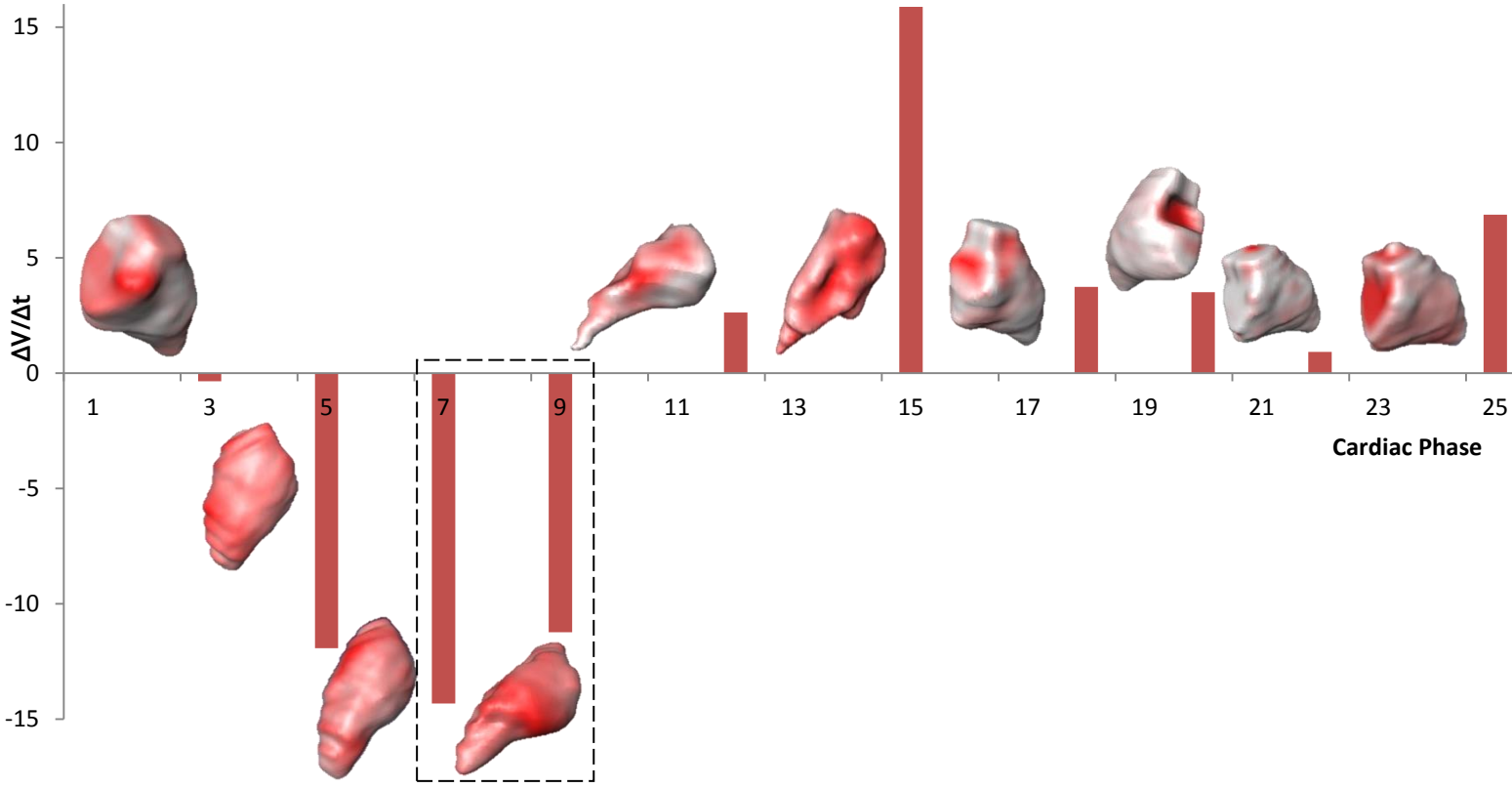

Figure 6.31 - LV volume variation rate calculated from the values presented in Table 6.8. Each surface icon, is placed between two time points and it shows the reconstructed surface in one specific frame and the distance to the reconstructed surface in the following frame, encoded in a color range: high distance values between surfaces are represented in red, whereas low distances are represented in white. The surfaces are displayed from a perspective, from which the regions that deformed the most could be visible (intensive red). The distance range encoded by the colors varies for each pair of surfaces. The figure in the dashed rectangle shows the shape of the surface reconstructed from the 7th frame and the intense red areas indicate the regions where

the distance to the surface reconstructed in the 9th time point is higher. The volume variation rate between this two time points is indicated in the bar at frame 9 (around 11% less).

6.5 – Concluding Remarks

The results obtained in each step of the developed framework for the reconstruction of the inner LV surface accomplished the previewed objectives. The final result consisted on anatomically accurate and smooth surfaces with a high-quality triangular mesh in eleven phases of the cardiac cycle, representing the natural shape variation of a beating heart. Therefore, the anatomic information contained in the different types of CMR images was used and combined in diverse manners. The segmentation of the inner LV region was performed after the requirements of the experts in cardiology involved in this project and the main misalignments between the sequences and among the slices in the SAX and TRA sequences were corrected by means of 3D and 2D translations, respectively. These transformations that were established in the ED phase were transferred and used to correct motion-related artifacts from the images in the other cardiac phases. By taking advantage of the different visualization modules available in Amira, it was possible to continuously analyze the obtained results, which at the end inspired confidence on the developed methodology. The final results were quantitatively evaluated by comparing the surfaces' area and volume in the different processing steps for three cardiac phases, namely the ED, the ES and the intermediary phase, which supported the conclusions extracted by visual inspection. Nevertheless, the lack of data from other patients and also of a ground-truth made it impossible to study the framework's level of generalization, to perform a statistical analysis and to validate it objectively. Considering the posterior cardiac flow simulations, in the future the inner LV surface in the remaining phases of the cardiac cycle should be reconstructed. After evaluating the performance of the reconstructed surfaces in blood-flow simulations, the manually performed tasks should be automatized (or at least require a lower level of user intervention) and a proper dataset for anatomical evaluation purposes should be established.

Chapter 7 – Discussion

In this project, a strategy for the anatomical reconstruction of the inner LV surface on different phases of the cardiac cycle had to be developed considering three main issues:

- the provided data, which consisted on different MRI sequences according to a specific protocol for the study of aortic valve and root diseases,
- the use of the software Amira (since some of the related projects are or will be computed with this software), and
- the required output: a shape representing accurately the anatomy of the inner LV suitable for cardiac deformation recovery and posterior patient-specific finite-element modeling in the context of aortic valve diseases.

This lead to the construction of a framework that consisted on the following main operations:

1) Sequences registration
2) Inner LV segmentation
3) Slices' alignment
4) Labels fusion
5) Smooth surface extraction
6) Isotropic surface-mesh generation.

The respective methodologies, challenges and results are integrated among them and with the correspondent state-of-the-art and discussed in the following subsections. Afterwards, a global quantitative evaluation is performed, by analyzing, comparing and interpreting the area and volume values extracted from the LV surface in different conditions. At the end, the main considerations regarding the whole developed framework is presented.

7.1 - Sequences' Registration

The common procedures for LV volume computation rely on cine-SAX images, since they present a good temporal resolution and also a high in-plane resolution, which allows the detection of the different anatomical contours (Tavakoli & Amini 2013). On the other side, this type of sequence is also characterized by a high slice thickness (up to 10 mm), which might result in loss of valuable anatomical information, especially in the apex and in the base (Carminati et al. 2014). In the developed framework this limitation has been overcome by the

combination and interpolation of multiple 2D views. Taking into account that the available data consisted on many types of MRI sequences that differed on the images orientation and scanned regions, it seemed useful to combine some of them, in order to obtain as much information as possible for an accurate anatomical LV reconstruction. In this context, it was mandatory to register the different types of sequences. Since the rigid body motion of the heart due to the respiration is mainly a translation in the cranio-caudal direction, while the rotation consists only on a couple of degrees (McLeish et al. 2002)the applied registration method compensates for 3D translational errors but not for rotation. This task was the most time-consuming one, since it was manually computed and the intersection between all images should be taken into consideration. (Carminati et al. 2014) presented an automatic and unsupervised method for the misalignment between the sequences based on pixel intensities at the intersections lines of the images. Basically, the intensities profiles in each intersection line of the images with different orientations were extracted and used as input of a cost function to guide the correction, based on the maximization of the correlation of the pixel intensities along the intersections between each slice. It resulted on a 2D translation in the image plane with improvement in 70% of the slices in need for correction. Taking into account that the handled data consisted on stacks of 2D-images and in order to maintain the planes equally spaced, besides the rotation, also the 3D translation was neglected. This method could be adapted to improve the manually performed registration task of this project, since it is a fast and automatic method that involves most of the CMR sequence types used in this project and it demonstrated valuable improvements.

7.2 - Inner LV Segmentation

At the level of interactive image segmentation, the main adversities were related to the 3D-WH sequence, where a larger amount of slices with lower in-plane resolution (when comparing to the TRA and SAX images) had to be segmented requiring a higher level of user intervention. In this type of images, besides the fuzziness present in some slices, the low contrast between different cardiac structures impeded an accurate inner LV region identification. Nevertheless, these difficulties only had to be faced once, since this sequence was performed only during the ED phase. As expected, in all types of sequence, the segmentation of the apical and basal slices was more challenging. The partial volume effect, a consequence of a voxel covering several types of tissues due to the non-zero thickness of MRI slices, can lead to fuzziness of these images (Petitjean & Dacher 2011). The identification of the LV cavities was also affected by the blood flow. Besides, this former effect is noticeable in the images from the intermediary phase, when the blood velocity is higher. In regard to the ES phase, this is a phase characterized by the maximal contraction, thickening and shortening of the LV wall, in order to eject the blood from the LV cavity (Young & Frangi 2009). As a consequence, the blood pool represented in the respective MR images consists on a very small, blurred and irregular bright area, which boundaries were difficult to establish, especially in the apical slices.

Recent literature about cardiac segmentation focuses on the development of automatic methods (Zhuang 2013, Tavakoli & Amini 2013) mainly due to the tediousness, the time consumption and the many sources of variability associated to this task (see Section 3.4). Before constructing an user independent method for the segmentation of the inner LV, it is mandatory to learn the interpretation of cardiac MR images and identify the challenges and limitations of the respective segmentation, as described above. The reasons why it was opted for an interactive instead of automatic method for the segmentation were already described in Chapter 5 (section 5.3, subsection A.3) and in sum, rely on the reduced data in the dataset and on the good efficiency of the Amira's *SegmentationEditor*.

7.3 - Slices' Alignment

When the cine sequences are used to track the heart's motion, such as the cine-SAX- and TRA sequences used in this project, the scanning method consist on the acquisition from several time points but only from one spatial location for each breath hold. If the phase of the breathing cycle is not similar during all acquisitions, slices acquired during different apneas will be misaligned relative to each other, and a volume built from the image series will not represent the subject's cardiac anatomy accurately (Lötjönen et al. 2004). For both cine stacks, these artifacts were evident when the respective images were displayed simultaneously with the LAX images, where it was possible to observe different levels of mismatching for each slice. The developed method for the slices' alignment in the stacks was governed by the 3 contours extracted from the LAX images. Taking into account that the former images were already aligned between each other and with the 3D-WH stack and that they presented a high in-plane resolution, the respective contours could be consider as true representations of the endocardial contours in different orientations. The use of a single contour to correct the slices shift would not be effective, since the motion artifacts usually consist on translations in more than one direction. Conversely, their combination provided a sufficient set of landmarks representing the cavity's boundaries, which could be used to guide the translation of each slice. This task was effectively completed with the Amira *AlignSlices* module, but it consisted on a manually and user dependent method, namely the matching of the inner LV label boundaries in each slice with the respective intersections points (IPs) with LAX contours by manual 2D-translations. The results show that in the first three reconstructed phases (Table 6.6), the area and volume of the surface extracted from the fused translated images is lower than from the fused original ones, confirming that the 2D translations (i.e. the applied in-plane slices' shifts) lead to a better match between the labels of the different sequences. In the future, an automatic method based on the minimization of the distance between the inner LV label and the IPs should be developed. In recent literature, such as the aforementioned (Carminati et al. 2014) or (Elen et al. 2010) and (Wei et al. 2013), it is possible to find automatic methods that take advantage from the combinations of images with different orientations, typically acquired in clinical routine, namely the cine-SAX- and LAX images. In contrast to the method here presented that relies on the matching of

segmented regions, these authors propose more complex techniques for motion artifacts correction, based on the voxel intensities correspondence in the intersection lines of the images. Regarding the developed method, despite the need of user intervention for the slices' alignment in the ED phase, in the remaining cardiac phases of the cardiac cycle this task became completely automatic, by transferring the 2D translation applied to each image in the ED phase to the respective slices in the remaining cardiac phases.

7.4 - Labels' Fusion

From the available dataset, it would be possible to generate a surface representing the inner LV from each MRI sequence that contained more than one 2D image of the LV, namely the 3D-WH, the cine-SAX- and TRA sequences. However, in the case of the 3D-WH images, the accuracy in the anatomy representation would be low, since these images have a low in-plane resolution that encumbers the segmentation task. In contrast, the cine images have a high in plane resolution but, at the same time, a high spacing between each slice, which could result in loss of important anatomical information, especially from the heart's apex and base. Besides, it would result in a surface with an intense "staircase" effect. In the case of the TRA sequence, the fact that it only covered half of the LV anatomy makes it impossible to extract the desired surface from this data. In this context, the idea of combining the information provided from all images to circumvent the described limitations seemed reasonable. In fact, in the ED phase, the results demonstrated that the volume computed from the fusion of the three extracted label fields increased in about 20%, when comparing to the surfaces extracted from the SAX label and from the 3D-WH one. The volume value obtained from the fused labels is in higher agreement with the ones reported in literature for the LV volume of patients with aortic regurgitation (Taniguchi et al. 2007). Despite this higher agreement, the difference between the values is still high, which is a consequence of patients' age difference: the patient participating in this project was an 8-years old child, in contrast to the patients that contributed for the measurement of the presented literature volume, with a mean age of 48 ± 14 years old.

The fusion of the labels increased the volume and the areas in all cases, which can be interpreted as a complementation of information regarding the LV region from the different types of CMRI sequences, supporting the conclusions made by the visual geometric evaluation of the surfaces. This effect is specially noticed in the ES phase (Table 6.6 and Figures 6.19 and 6.20), where the labels extracted from the individual sequences represent a very irregular shape. Taking into account that in this contraction phase of the LV it is very hard to clearly identify the boundaries of the irregular LV cavity, the combination from different view planes allows a better delineation of this region in the 3D space by complementation of information.

For the best of the author's knowledge, this was the first time that these types of MRI sequences were fused to reconstruct the anatomy of the inner LV, although, in current

literature, the combination of different images, such as delayed-enhancement MRI (Ringenberg et al. 2012) or tagged MRI (Wang & Amini 2012) with cine-MRI, and even the combination of different modalities such as CT, MRI and US (Tavakoli & Amini 2013) are frequently reported, but for other purposes than the anatomical reconstruction, such as scar tissue delineation or the cardiac motion recovery.

7.5 - Surface Smoothing

At this phase of the LV reconstruction framework, the representation of the LV cavity consisted on an anatomically detailed 3D label in a stack of binary and aligned 2D images. In order to better visualize the final segmentation results and motion corrections, a surface rendering was computed. Besides, considering the posterior biophysical simulations, there is a need for a surface mesh as a basis for volume grids that are usually used for this purpose. In Figure 6.10, it is possible to recognize the non-anatomical staircase artifact and a noisy surface, which are typical in results from the *Marching Cubes* algorithm applied to segmented information from tomographic medical image data that exhibits anisotropic voxels (Preim & Charl 2013). For a correct and convenient perception and representation of the heart shape, these artifacts were minimized by a smoothing operation applied to the labeled field before surface extraction, taking into account the preservation of anatomical accuracy. The overall shape of the inner LV was preserved in the reconstructed phases of the cardiac cycle, and the noisy details were removed. The numeric results show that the smoothing of the surfaces reduced the volume and areas of all surfaces extracted from the fused labels, but more significantly in the original ones, suggesting a higher level of irregularity in the surfaces extracted from the original labels. However, in the ES phase, where the LV cavity presents a naturally shrinked and irregular shape, the unconstrained smoothing could lead to the loss of some important details, such as the tip of the apex. An attempt to circumvent this problem was done by changing the smoothing type in the *SurfaceGen* module from *unconstrained* (kernel size 5) to *constrained smooth* (kernel size 4). Besides, the *constrained smoothing* method ensures that no label is modified: any two voxel centers that have been labeled differently before the smoothing, namely as *innerLV* or *Exterior*, are separated by the generated surface afterwards. Regarding the unconstrained smoothing, this is not necessarily the case for every small detail, which lead to a smoother surface, but also to the loss of some apical voxel. The unconstrained smoothing method preserved the apex structure but at cost of smoothness, resulting in a noisy surface. The effect of each smoothing type in the ES phase can be visualized in Appendix B. At the end, the smooth surface generated with the unconstrained smoothing method was used for posterior volume and areas analysis and for surfaces visualization, because the excluded apex region could correspond to an erroneous segmentation, typical of the apical slices (and especially difficult to identify in the ES phase). According to (Preim & Charl 2013), one can apply a number of techniques to improve the trade-off between smoothness and accuracy of a surface generated from medical data. The authors divided the approaches in two different stages, namely at the image level, by post-

processing the segmentation results and at the polygonal mesh level, by smoothing and processing the mesh generated from the segmented regions. This is a relevant problem in shape representations for medical applications and it already gave rise to many refinements, which should be subject of study in future work on this project.

7.6 - Surface Remeshing

The final step of the reconstruction framework consisted on the remeshing of the surface, in order to obtain an appropriate basis for the volume grid for future cardiac simulations. The final remeshed surfaces were smooth and accurate, with high triangle quality and a gradual change in the triangle size (Figure 6.15), which after (Preim & Charl 2013) represent the essential surface meshes requirements for simulation purposes.

7.7 - Summarized Quantitative Evaluation

In order to quantitatively analyze the effect of each technique on the reconstructed surfaces, two tables are given in Chapter 6:

1. one presenting the area and volume values obtained from the reconstructed smoothed surfaces for each type of sequence (3D-WH, SAX and TRA) and the respective fusion, before and after all type of translations, for three cardiac phases (ED, TP5 and ES) (Table 6.6)
2. and another with the values for ED and ES volumes for patient with a valve disease found in (Taniguchi et al. 2007) (Table 6.7).

Regarding the values obtained in this project, no significant differences are observed between the volumes of the original labeled images and the transformed ones (before the fusion). Nevertheless, the applied transformations lead to the reconstruction of an inner LV surface with a better and smoother geometry for simulation purposes and anatomically more accurate. This evaluation was confirmed by an expert in blood-flow simulations, who will use the generated surfaces to study the blood-flow in the patients with an aortic valve disease. This observation was confirmed by the decrease in the volume and areas from the fused corrected labels when comparing with the fused original labels, suggesting a higher agreement between the corrected images. Regarding the effect of the labels' fusion, in all cases it lead to a surface involving a higher volume than the surfaces generated from the individual labels, especially in the ES phase, where the segmentation of the inner LV region in all types of images is cumbersome. This volume increase can be interpreted as a complementation of information provided by the different types of MRI sequences, since it presents a higher level of agreement with the literature values for the volumes of the inner LV for patients with an aortic regurgitation in the ED and ES phase. As expected, the volume and area of the smoothed "fused" surface are lower than the ones from the "fused" surface generated without smoothing, since the associated sharp edges are attenuated by the smoothing process. This effect is more accentuated in the surface extracted from the fused

original labels, suggesting a lower level of irregularity in the surfaces extracted from the corrected ones, which contributes to the statement that the applied transformations lead to a better match between the different sequences, and ultimately to a more accurate representation of the surface.

Comparing the final inner LV volumes obtained for the ED and ES phases with the ones presented in the literature for patients with aortic regurgitation (Table 6.7) a high discrepancy is noticeable, probably due to the age difference of the patients that participated in each study, but also due to the different techniques utilized for the calculation on the volumes.

Finally, the results concerning the variation of LV volume during one cardiac cycle confirm that the developed method is able to extract correct representations of the LV cavity in different phases of the cardiac cycle, since the variation profile coincides with the ones found in the literature and also with the natural deformation of a beating heart. Besides, with the temporal reconstruction it is possible to:

- precisely define the cardiac phases that represent the ED and the ES, which are used to calculate parameters of the LV function, such as the LV ejection fraction. Thus, the reconstructed surfaces can serve as a primary analysis of the LV function and performance.
- Identify the level of deformation in different regions of the LV and in different intervals of the cardiac cycle, which can significantly vary between healthy and pathological hearts.

The quantitative evaluation of the obtained results in each step has been supported with the qualitatively analysis by the author and by experts in the field of cardiac segmentation and cardiac flow simulations. Therefore, the Amira software played a crucial role, by allowing the visualization and combination from the data in many different ways, for instance the slices' alignment as shown in Figures 6.8, 6.21 and 6.22 or the smooth surfaces generation in Figures 6.12 and 6.13. Quantitative results were obtained by the calculation of the volumes enclosed by each reconstructed surface, which were consistent with the ones presented in the literature. At the end, the visual evaluation of the results and the obtained volume values inspired confidence on the developed methods. Nevertheless, in future work, it is indispensable to obtain a ground truth for effects of comparison, and a much higher number of patients data should be tested to validate the method and study its generalization level, which is especially difficult for techniques applied to the cardiac images due to the associated numerous sources of variability. Future perspectives also include the application of the method to the remaining 14 cardiac phases, in order to obtain a higher temporal resolution for the cardiac motion and deformation recovery and to study their influence on the blood flow.

Chapter 8 – Conclusions and Future Perspectives

The present dissertation explores the field of cardiac modelling and proposes a strategy to computationally reconstruct the 3D anatomy of the left ventricle (LV) cavity in different phases of the cardiac cycle for posterior patient-specific simulations. First, it introduces the background of heart modeling and describes the main concepts associated to this field. Before the establishment of a reconstruction framework, it is important to understand the complex anatomy and physiology of this involuntary moving organ to be able to interpret the data formed by the main imaging technologies available nowadays, namely, MRI, US, CT, PET and SPECT. All of them have associated advantages and disadvantages, but MRI data were chosen to develop this project, mainly because it is a non-ionizing technology that provides images of any part of the human body from any angle and direction with good spatial and temporal resolutions. Besides, there are different types of acquisition modes that enable the imaging of the different components of the cardiovascular system and their function.

The fact that cardiovascular diseases are the number one cause of death in the world lead to a great investment in cardiac research in the past years. This, together with the rapid development of imaging techniques gave the possibility to construct many different types of heart models, from the simple anatomical ones to more complex ones, such as electrophysiological or dynamic cardiac models, which combine medical images and clinical parameters with biophysical models.

Cardiac analysis has focused mostly on the LV, since this primary heart chamber controls systemic perfusion and is responsible for pumping blood throughout the entire body. The extraction of clinical parameters related to the LV, such as LV volume and pressure, are essential to obtain functional indexes of this chamber, which in turn provide the identification and characterization of pathological states, such as the aortic valve disease. In this pathology, the timing and type of treatment (surgery, catheter based intervention or medication/follow-up) are crucial to prevent potentially life threatening sequelae (e.g. heart failure) and, on the other hand, to avoid too early procedures. Therefore, personalized LV models that represent the current state of the patient's cardiac anatomy and function, and which also enable personalized simulations of the possible interventions are essential. This need lead to the interest in developing personalized anatomical and geometrical LV models suitable for cardiac flow simulations, giving rise to this dissertation's project, which presents a strategy to translate MRI data used in clinical practice into 3D finite element models of the inner LV cavity. The developed framework has as input different types of cardiac MRI sequences, which essentially differ in the orientation, scanned volume and resolution, and the final output consists in smooth surfaces with high mesh quality that represent accurately the shape and anatomy of the LV cavity in different phases of the cardiac cycle and can be adopted to conduct cardiac flow simulations. The proposed framework presents simple

methodologies to interactively, using the Amira software, overcome the main challenges associated to the complex tasks of cardiac modelling, namely the registration between different types of images, the segmentation of the irregular and variable inner LV region, the correction of motion related artifacts and the reconstruction of a smooth surface mesh. The reconstruction of the LV in the first time frame requires a high level of user intervention but for the remaining cardiac phases this intervention is significantly reduced by transferring to each image the respective established transformations from the first reconstructed phase. At the end, a set of surfaces representing the LV cavity in different phases of one cardiac cycle were obtained, from which it was possible to:

- observe the natural cyclical deformation of a beating heart,
- detect the correct end systolic and end diastolic phases,
- calculate the ejection fraction of the LV and also
- detect the regions of the LV surface that deform at most between two reconstructed surfaces.

These accurate results are important to conduct a primary analysis of the anatomical and functional state of the patient's heart and can posteriorly serve as one of the inputs for the development of a patient-specific mechanical model of the LV, not only in the case of AVD but also in other pathological cases. With this project it was possible to identify the challenges associated to the LV modelling and to delineate and validate an interactive strategy to overcome the inherent challenges of this research field, which in the future can serve as basis to develop a more automatic framework.

Despite the abounding applications that can be found for the developed LV models, such as patient-specific simulations for diagnostics and treatments, surgical support, medical training and medical teaching, the translation of these models into clinical practice still has to be achieved. Thus, the main future perspectives and improvements to validate the developed strategy and achieve the translation into clinical practice include:

- the reconstruction of the LV cavity in the remaining cardiac phases, in order to obtain a higher temporal resolution for the cardiac motion and deformation recovery and to study their influence on the blood flow;
- the establishment of a ground truth for effects of comparison and validation of the methods;
- the application of the developed method to a higher number of patients' data to validate the method and study its generalization level, which is especially difficult for techniques applied to the cardiac images due to the associated numerous sources of variability;
- and finally, the development of automatic methods to fulfill each user-dependent task of the proposed methodology.

References

American Heart Association, Heart Disease and Stroke Statistics, Update (at-a- glance version), 2009. http://www.americanheart.org/presenter.jhtml?identifier=3037327 [Accessed on February, 2014]

Baillargeon, B., Rebelo, N., Fox, D. D., Taylor, R. L., & Kuhl, E. (2014). The Living Heart Project: A robust and integrative simulator for human heart function. *European Journal of Mechanics - A/Solids*, 1–10.

Billet, F., Sermesant, M., & Ayache, N. (2004). Cardiac motion recovery and boundary conditions estimation by coupling an electromechanical model and cine-mri data.

Blanquer, I., Hernandez, V., Lonsdale, G., Dean, K., Lloyd, S., McClatchey, R., Claerhout, B. (2004). The Healthgrid White Paper. *The HealthGrid Association*, 1–90.

Bogaert, J., Dymarkowski, S., Taylor, A. M., & Muthurangu, V. (2012). *Clinical Cardiac MRI* (p. 709). Springer Science & Business Media.

Borazjani, I., Westerdale, J., Mcmahon, E. M., Rajaraman, P. K., Heys, J. J., & Belohlavek, M. (2013). Left ventricular flow analysis: recent advances in numerical methods and applications in cardiac ultrasound. *Computational and Mathematical Methods in Medicine*, 2013, 395081.

Carminati, M. C., Maffessanti, F., & Caiani, E. G. (2014). Nearly automated motion artifacts correction between multi breath-hold short-axis and long-axis cine CMR images. *Computers in Biology and Medicine*, *46*, 42–50.

Cerqueira, M. (2002). Standardized myocardial segmentation and nomenclature for tomographic imaging of the heart: A statement for healthcare professionals from the Cardiac Imaging Committee of the Council on Clinical Cardiology of the American Heart Association. *Journal of Nuclear Cardiology*, *9*(2), 240–245.

Christodoulou, A. G., Zhao, B., Zhang, H., Ho, C., & Liang, Z. P. (2011). Four-dimensional MR cardiovascular imaging: method and applications. *Conference Proceedings: ... Annual International Conference of the IEEE Engineering in Medicine and Biology Society. IEEE Engineering in Medicine and Biology Society. Conference*, *2011*, 3732–3735.

Dell, W. G. O., & Mcculloch, A. D. (2002). Imaging three-dimensional cardiac function. *Annu. Rev. Biomed. Eng.*, *02*, 431–456.

Deng, D., Jiao, P., Ye, X., & Xia, L. (2012). An image-based model of the whole human heart with detailed anatomical structure and fiber orientation. *Computational and Mathematical Methods in Medicine*, *2012*, 891070.

Elen, A., Hermans, J., Ganame, J., Loeckx, D., Bogaert, J., Maes, F., & Suetens, P. (2010). Automatic 3-D breath-hold related motion correction of dynamic multislice MRI. *IEEE Transactions on Medical Imaging*, *29*(3), 868–78.

Frangi, A. F., Radeva, P. I., Santos, A., Lorenz, C., & Berg, J. von. (2006). A comprehensive shape model of the heart. *Medical Image Analysis*, *10*(4), 657–670.

Gutiérrez, L.F., Silva, R.,Ozturk, C, Sonmez, M., Stine, A. M., Raval, A.N., Venkatesh K. R., Vandana S., Ronnier J. A., Myron A. W., Elliot R. M., Robert J. L. (2007). Technology

preview: X-ray fused with magnetic resonance during invasive cardiovascular procedures. *Catheterization and Cardiovascular Interventions*, 70(6), 773–782.

Hoogendoorn, C., Duchateau, N., Sánchez-Quintana, D., Whitmarsh, T., Sukno, F. M., De Craene, M., Frangi, A. F. (2013). A high-resolution atlas and statistical model of the human heart from multislice CT. *IEEE Transactions on Medical Imaging*, *32*(1), 28–44.

Kaus, M. R., von Berg, J., Weese, J., Niessen, W., & Pekar, V. (2004). Automated segmentation of the left ventricle in cardiac MRI. *Medical Image Analysis*, *8*(3), 245–54.

Knecht, S., Skali H., O'Neill M. D., Wright M., Matsuo S., ChaudhryG. M., Haffajee C.I. (2008). Computed tomography-fluoroscopy overlay evaluation during catheter ablation of left atrial arrhythmia. *Europace*, 10, 931–938.

Laschinger, J. C., Vannier, M. W., Gronemeyer, S., Gutierrez, F., Rosenbloom, M., & Cox, J. L. (1988). Noninvasive three-dimensional reconstruction of the heart and great vessels by ecg-gated magnetic resonance imaging: a new diagnostic modality. *The Annals of Thoracic Surgery*, *45*(5), 505–514.

Leal, J., Luengo-Fernández, R., Gray, A., Petersen, S., & Rayner, M. (2006). Economic burden of cardiovascular diseases in the enlarged European Union. *European Heart Journal*, *27*(13), 1610–9.

Lee, L. C., Wenk, J. F., Zhong, L., Klepach, D., Zhang, Z., Ge, L., Guccione, J. M. (2013). Analysis of patient-specific surgical ventricular restoration: importance of an ellipsoidal left ventricular geometry for diastolic and systolic function. *Journal of Applied Physiology (Bethesda, Md.: 1985)*, *115*(1), 136–44.

Lee, V. S. (2006). Cardiovascular MRI: Physical Principles to Practical Protocols. *Lippincott Williams & Wilkins*.

Long, Q., Merrifield, R., Xu, X. Y., Kilner, P., Firmin, D. N., & Yang, G.-Z. (2008). Subject-specific computational simulation of left ventricular flow based on magnetic resonance imaging. *Proceedings of the Institution of Mechanical Engineers, Part H: Journal of Engineering in Medicine*, *222*(4), 475–485.

Lötjönen, J., Kivistö, S., Koikkalainen, J., Smutek, D., & Lauerma, K. (2004). Statistical shape model of atria, ventricles and epicardium from short- and long-axis MR images. *Medical Image Analysis*, *8*(3), 371–86.

Magnetic Resonance - Technology Information Portal, 2014. http://www.mr-tip.com/. [Accessed on February, 2014]

Markl, M., Frydrychowicz, A., Kozerke, S., Hope, M., & Wieben, O. (2012). 4D flow MRI. *Journal of Magnetic Resonance Imaging: JMRI*, *36*(5), 1015–36.

McLeish, K., Hill, D. L. G., Atkinson, D., Blackall, J. M., & Razavi, R. (2002). A study of the motion and deformation of the heart due to respiration. *IEEE Transactions on Medical Imaging*, *21*(9), 1142–50.

Mulkern, R. V., & Chung, T. (2000). From signal to image: magnetic resonance imaging physics for cardiac magnetic resonance. *Pediatric Cardiology*, *21*(1), 5–17.

Nguyen, V.-T., Loon, C. J., Nguyen, H. H., Liang, Z., & Leo, H. L. (2013). A semi-automated method for patient-specific computational flow modelling of left ventricles. *Computer Methods in Biomechanics and Biomedical Engineering*, 37–41.

Nickisch, H., Barschdorf, H., Weber, F. M., & Krueger, M. W. (2013). From image to personalized cardiac simulation : encoding anatomical structures into a model-based segmentation framework. *Lecture Notes in Computer Science (including Subseries Lecture Notes in Artificial Intelligence and Lecture Notes in Bioinformatics)*, *Volume 774*, 278–287.

Niederer, S. A., Lamata, P., Plank, G., Chinchapatnam, P., Ginks, M., Rhode, K.,Smith, N. P. (2012). Analyses of the redistribution of work following cardiac resynchronisation therapy in a patient specific model. *PloS One*, *7*(8), e43504.

Nishimura, R. A. (2002). Aortic valve disease. *Circulation*, *106*(7), 770–772.

Petitjean, C., & Dacher, J.-N. (2011). A review of segmentation methods in short axis cardiac MR images. *Medical Image Analysis*, *15*(2), 169–84.

Peyrat, J.-M. (2009). Comparison of cardiac anatomy and function: statistics on fibre architecture from dt-mri and registration of 4d CT images. *Nice - Sophia Antipolis University*, *Ph.D. Thes*.

Preim, B., & Charl. (2013). Visual Computing for Medicine, 2nd Edition.

Ringenberg, J., Deo, M., Devabhaktuni, V., Berenfeld, O., Snyder, B., Boyers, P., & Gold, J. (2013). Accurate reconstruction of 3D cardiac geometry from coarsely-sliced MRI. *Computer Methods and Programs in Biomedicine*, 113, 483-493.

Ringenberg, J., Deo, M., Devabhaktuni, V., Filgueiras-Rama, D., Pizarro, G., Ibañez, B.,Gold, J. (2012). Automated segmentation and reconstruction of patient-specific cardiac anatomy and pathology from in vivo MRI. *Measurement Science and Technology*, *23*(12), 125405.

Rhode, K.S., Sermesant, M., Brogan, D., Hegde, S., Hipwell, J., Lambiase, P., Rosenthal, E., Bucknall, C., Qureshi, S.A., Gill, J.S., Razavi, R., Hill, D.L. (2005). A system for real-time XMR guided cardiovascular intervention. I*EEE Transactions on Medical Imaging*, 24, 1428–1440.

Sermesant, M., Peyrat, J.-M., Chinchapatnam, P., Billet, F., Mansi, T., Rhode, K., Ayache, N. (2008). Toward patient-specific myocardial models of the heart. *Heart Failure Clinics*, *4*(3), 289–301.

Skrinjar, O., & Bistoquet, A. (2009). Generation of myocardial wall surface meshes from segmented MRI. *International Journal of Biomedical Imaging*, *2009*, 313517.

Smith, N., Vecchi, A. De, Mccormick, M., Nordsletten, D., Camara, O., Alejandro, F., Rezavi, R. (2011). euHeart : personalized and integrated cardiac care using patient-specific cardiovascular modelling.

Tan, M.-L., Su, Y., Lim, C.-W., Selvaraj, S. K., Zhong, L., & Tan, R.-S. (2013). A geometrical approach for automatic shape restoration of the left ventricle. *PloS One*, *8*(7), e68615.

Tang, D., Yang, C., Geva, T., & Del Nido, P. J. (2010). Image-based patient-specific ventricle models with fluid-structure interaction for cardiac function assessment and surgical design optimization. *Progress in Pediatric Cardiology*, *30*(1-2), 51–62.

Taniguchi, K., Takahashi, T., Toda, K., Matsue, H., Shudo, Y., Shintani, H.,Sawa, Y. (2007). Left ventricular mass: impact on left ventricular contractile function and its reversibility in patients undergoing aortic valve replacement. *European Journal of Cardio-Thoracic*

Surgery: Official Journal of the European Association for Cardio-Thoracic Surgery, *32*(4), 588–95.

Tavakoli, V., & Amini, A. A. (2013). A survey of shaped-based registration and segmentation techniques for cardiac images. *Computer Vision and Image Understanding*, *117*(9), 966–989.

Trayanova, N. A. (2011). Whole-heart modeling: applications to cardiac electrophysiology and electromechanics. *Circulation Research*, *108*(1), 113–28.

Trayanova, N. A, O'Hara, T., Bayer, J. D., Boyle, P. M., McDowell, K. S., Constantino, J., Vadakkumpadan, F. (2012). Computational cardiology: how computer simulations could be used to develop new therapies and advance existing ones. *Europace: European Pacing, Arrhythmias, and Cardiac Electrophysiology : Journal of the Working Groups on Cardiac Pacing, Arrhythmias, and Cardiac Cellular Electrophysiology of the European Society of Cardiology*, *14 Suppl 5*, v82–v89.

Vahanian, A., Alfieri, O., Andreotti, F., Antunes, M. J., Barón-Esquivias, G., Baumgartner, H., Zembala, M. (2012). Guidelines on the management of valvular heart disease (version 2012). *European Heart Journal*, *33*(19), 2451–96.

Vota, E., Bao Le, T., Stevanella, M., & Fusini, L. (2014). Toward patient-specific simulations of cardiac valves: state-of- the-art and future directions. *J Biomech .*, 217–228 *46*(2), 217–228.

Wang, H., & Amini, A. A. (2012). Cardiac motion and deformation recovery from MRI: a review. *IEEE Transactions on Medical Imaging*, *31*(2), 487–503.

Weese, J., Groth, A., Nickisch, H., Barschdorf, H., Weber, F. M., Velut, J., Hose, D. R. (2013). Generating anatomical models of the heart and the aorta from medical images for personalized physiological simulations. *Medical & Biological Engineering & Computing*, *51*(11), 1209–19.

Wei, D., Sun, Y., Ong, S.-H., Chai, P., Teo, L. L., & Low, A. F. (2013). A comprehensive 3-D framework for automatic quantification of late gadolinium enhanced cardiac magnetic resonance images. *IEEE Transactions on Bio-Medical Engineering*, *60*(6), 1499–508.

Young, A. A., & Frangi, A. F. (2009). Computational cardiac atlases: from patient to population and back. *Experimental Physiology*, *94*(5), 578–96.

Zhuang, X. (2013). Challenges and Methodologies of Fully Automatic Whole Heart Segmentation: A Review. *Journal of Healthcare Engineering, 4*(3), 371–407.

Appendix A – Results in Time Point 5 (TP5)

The results obtained in each step of the inner LV reconstruction in the intermediary phase (TP5) of the cardiac cycle are resented bellow.

Figure 1- Intersection of a) 4CH and 3CH, b) 2CH and 3CH and c) 2CH and 4CH images of the intermediary phase of the cardiac cycle (TP5), before and after 3D translation of the images.

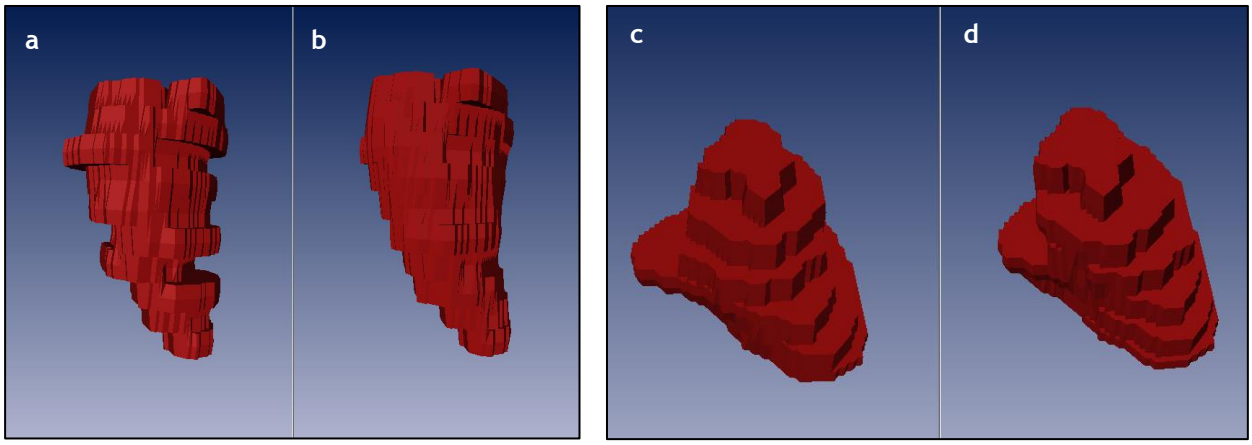

Figure 2 - Comparison of the inner LV surface generated from the SAX label field (a) before and (b) after slices' alignment and from TRA label field before (c) and after (b) slices' alignment.

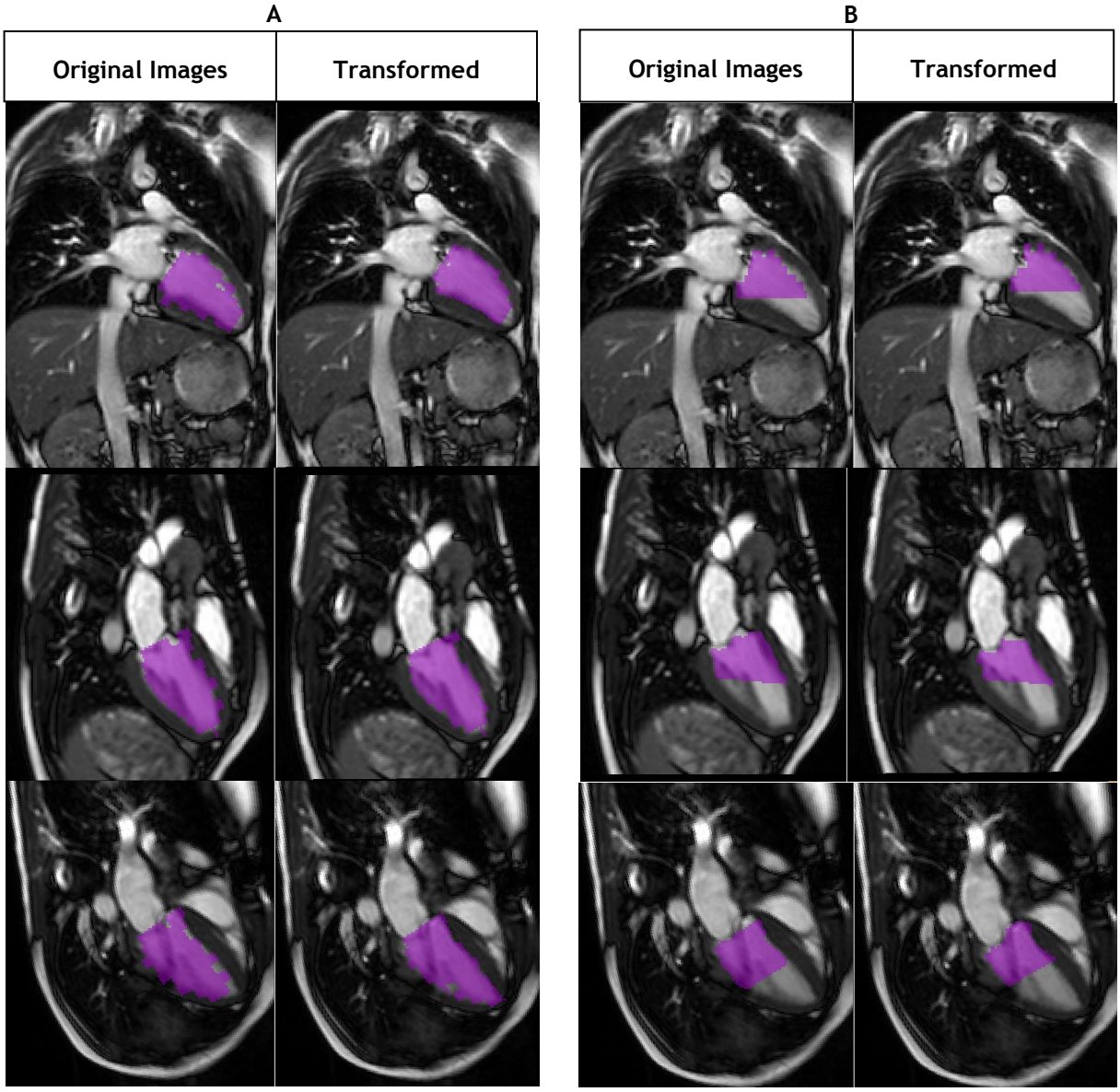

Figure 3 - Original and transformed SAX (right) and TRA (left) inner LV label (purple) overlaid on the a) 2CH, b) 3CH and c) 4CH images in the intermediary phase (TP5) of the cardiac cycle.

Appendix B - Effect of smoothing type on the inner LV surface from the ES phase

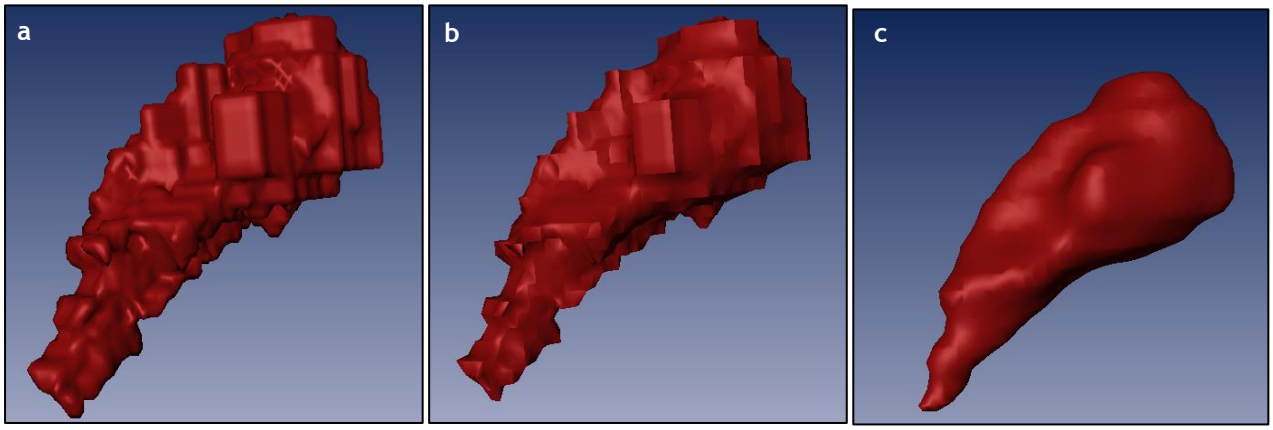

Figure 1 - Inner LV surface generated without smoothing (a), with constrained smoothing (b) and with unconstrained smoothing (c), in the ES phase.

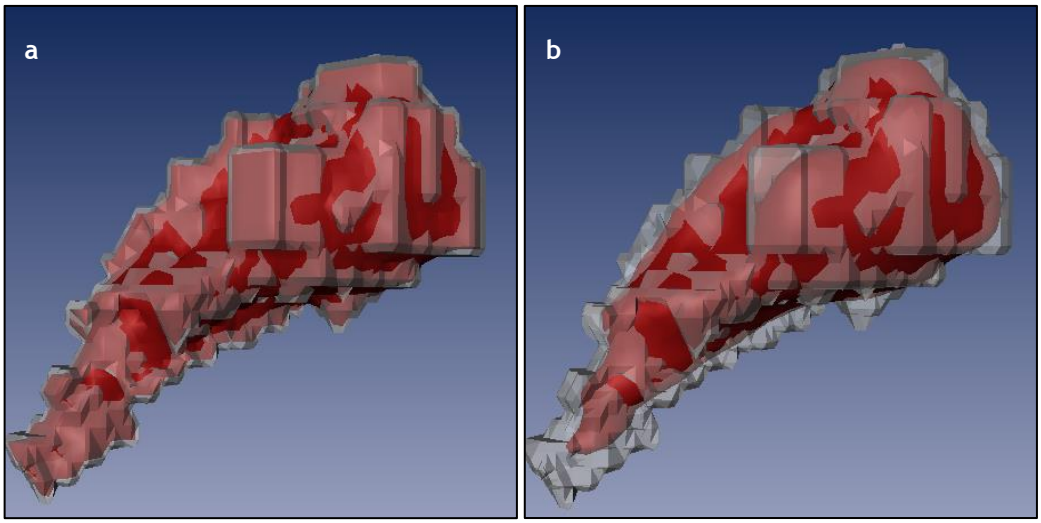

Figure 2 - ES surface generated without smoothing (transparent) superimposed on the same surface generated with constrained smoothing (a) and with unconstrained smoothing (b).